Aeroelastic Analysis and Classical Flutter of a Wind Turbine using BLADEMODE V.2.0 and PHATAS in FOCUS 6

RP Baran
1222996

TU Delft

ECN
Your energy. Our passion.

Aeroelastic Analysis and Classical Flutter of a Wind Turbine using BLADEMODE V.2.0 and PHATAS in FOCUS 6

Master of Science Thesis

For the degree of Master of Science in Sustainable Energy Technology
at Delft University of Technology

Author
RP Baran

Supervisor
Dr.ir. J.G. Holierhoek

Exam committee
Prof. Dr. G.J.W. Van Bussel
Dr. Ir. W.A.A.M. Bierbooms
Dr.ir. J.G. Holierhoek
Dr.ir. R. de Breuker

24th of June 2013

Faculty of Applied Sciences, Delft University of Technology

ABSTRACT

In a world where renewable energy sources are becoming more relevant, wind energy takes an important position in the current and future energy market. In order to become a bigger player in this market it is first important to provide a solid reliable product. To this extent, it is important to consider classical flutter for a wind turbine, as here flap and torsion vibration of the blade couple with each other resulting in a potential catastrophic failure of the wind turbine. Classical flutter is considered a dynamic instability boundary problem, which means that there is a specific rotational speed boundary beyond which the fluid-structure interaction becomes unstable. For classical flutter this boundary is the flutter speed. Due to the wind turbine blades getting larger, the possibility of the blades approaching the flutter speed is increased. Therefore the purpose of this thesis is to find a clear and efficient procedure to analyze the flutter speed.

To fulfill this purpose, simulations are performed with the programs BLADEMODE V.2.0 and PHATAS, based on the ART5 reference wind turbine model. BLADEMODE V.2.0 is primarily used as a stand-alone program, while PHATAS is employed in the user friendly environment of the shell-program FOCUS 6. This is because the release version of the stand-alone version of BLADEMODE V.2.0 is more recent than the one incorporated in FOCUS 6.

There are three simulations performed with BLADEMODE V.2.0 in order to deduce if classical flutter occurs. For each simulation BLADEMODE V.2.0 generates an output file containing the necessary data to construct 2D plots of the mode shapes and a Campbell plot. Constructing the 2D plots, with the deformation data generated, makes it possible to determine the dominant mode shapes. These mode shapes are viewed in the Campbell plot from which it can be deduced if classical flutter occurs or not. This is done by noticing if a flap-wise mode approaches a torsional mode, which is expected for classical flutter, as the rotor speed increases.

With the built-in loadcase generator LCPREP in FOCUS 6, the overspeed loadcase is generated for PHATAS. This loadcase is used for the classical flutter analysis. The simulation produces the time history behavior of output parameters relevant to classical flutter. The most important output parameters chosen are the flap-wise displacement and torsional deformation. These two parameters are linked to a flap-wise and torsional mode respectively, which are essential for classical flutter. Combined with the generated rotor speed curve, a four step method is established to determine if classical flutter occurs and how the flutter speed can be determined. This is done by considering the vibrations in the flap-wise and torsional deformation curves, by appropriately zooming in on the graphs. Once the method is established, it is analyzed how the flutter limit may be increased by performing simulations for changing pitch angle values or altering the torsional stiffness values of the blade. Following this, it is desired to know how the natural frequency at which classical flutter occurs can be determined. Therefore, the built-in post-processor in FOCUS 6 is used to transforms the signals of the output parameters from the time domain to the frequency domain, via a Fast Fourier Transform (FFT). This is done for the relevant output parameters and as a result a power spectral density (PSD) plot is generated. The analysis of the natural frequency is based on the fact that this PSD describes how the power of a signal or time series is distributed over the different frequencies. The natural frequency at which classical flutter occurs can be recognized in the PSD as it is represented by a ‘spike’ or narrow peak. Here a small amount of an input force can cause a very large response. This is what would be expected for classical flutter. Furthermore the PSD for the flap-wise displacement should contain this peak at a similar frequency as the peak of the PSD for the torsional deformation. Because when classical flutter occurs these frequencies have approached each other.

The analysis with BLADEMODE V.2.0 shows that it is not possible to detect classical flutter with this program, while with PHATAS the four step method is determined to be the tool for an efficient procedure to analyze the flutter speed.

PREFACE

This work is done for the Energy research Centre of the Netherlands (ECN). The basis for this report was a literature study on classical flutter and obtaining theoretical background information on BLADEMODE V.2.0 and PHATAS. Using this knowledge the results were obtained using the shell-program FOCUS 6.

I would like to thank my supervisor dr.ir. Jessica Holierhoek (ECN) without whom it would be impossible to complete this thesis. If not for her guidance, patience, insights and taking the time to help me whenever I did not know how to move forward, this thesis could not have been completed. Also, I am grateful to ir. Koert Lindenburg (ECN) and dr.ir. Wim Bierbooms (TU Delft)for taking the time to evaluate my work and provide me with useful information and guidance. Furthermore, special thanks to Gerben de Winkel and Remco Brood from Wind turbine Materials and Constructions (WMC), who provided FOCUS 6 and were kind enough to take the time to familiarize me with the program via two workshops. Next to this, I want to thank the Wind Energy department from the faculty of Aerospace Engineering at the Delft University of Technology for providing the facilities so that I could complete my work.
Special thanks to my girlfriend (Rohini) for being with me during my study and making me a better person. You have provided me with care and motivation to complete this work. Finally, I want to thank my family, especially my parents. Their caring and hard work has enabled me to be who I am today and do what I have wanted to do in my life. My gratitude towards them cannot be emphasized enough.

Rajeev Prithviraj Baran

Delft, The Netherlands
24th of June 2013

TABLE OF CONTENTS

LIST OF SYMBOLS

Symbols	Unit	Description
a_{ind}	-	Axial induction factor
a'	-	Tangential induction factor
b	[m]	Blade span
c	[m]	Local blade chord
ca_{AC}	[m]	Distance between the aerodynamic center and elastic axis
ca_{CG}	[m]	Distance between the center of gravity and elastic axis
d	[m]	The perpendicular distance between an axis through the CG and the parallel axis
dm	[kg]	Mass element
h	[m]	Flap-wise translation
$\dot{h}$	[m/s]	Flap-wise velocity
$\ddot{h}$	[m/s^2]	Flap-wise acceleration
k	-	Reduced frequency
k_f	[N/m/m]	Flap-wise bending stiffness
k_t	[N · m/m]	Torsional stiffness
m	[kg]	Mass per unit section
q	-	Vector containing the flap-wise translation h and torsional rotation θ
r	[m]	Radial position along the blade span
r_{CG}	-	Normalized radius of gyration about the center of gravity
t	[s]	Time
x	[m]	Distance between the mass element dm and the elastic axis
x_b	-	X-axis local blade reference system
y_b	-	Y-axis local blade reference system
ż	[m/s]	Vertical speed (flap-wise velocity)
z_b	-	Z-axis local blade reference system
A	[m]	Amplitude of the oscillation
A_1	[m]	Amplitude of the oscillation for the 1st edge-wise mode shape
A_2	[m]	Amplitude of the oscillation for the 2nd edge-wise mode shape
C_L	-	Lift coefficient
C_L'	[deg^{-1}]	Lift curve gradient
F	[N]	Force
F_i	[N]	Inertia force
F_p	[N]	Progressive force
F_r	[N]	Retrograde force
F_{Y^F}	[N]	Y^F-component of reaction force at the hub
F_{Y^R}	[N]	Y^R-component of reaction force at the hub
F_{Z^F}	[N]	Z^F-component of reaction force at the hub
F_{Z^R}	[N]	Z^R-component of reaction force at the hub
I_{CG}	[kg m^2/m]	Mass moment of inertia about the axis through the center of gravity
I_θ	[kg m^2/m]	Mass moment of inertia about the elastic axis
L	[N]	Aerodynamic lift force
L_0	[N]	Steady-state lift force
M_{EA}	[Nm]	Moment about the elastic axis due to the lift force acting at the aerodynamic center
$R_{g,CG}$	[m]	Radius of gyration about the center of gravity
S_θ	[kg m/m]	Static moment related to the elastic axis
T	[J]	Total kinetic energy of the airfoil section
V	[J]	Potential energy of the airfoil section
W	[m/s]	Relative speed
W_0	[m/s]	Steady-state relative speed of the inflow
U_0	[m/s]	Free-stream wind velocity

Y^F	-	Y-axis non-rotating reference frame
Y^R	-	Y-axis rotating reference frame
Z^F	-	Z-axis non-rotating reference frame
Z^R	-	Z-axis rotating reference frame

Greek symbols	**Unit**	**Description**
α	[deg]	Angle of attack
α_0	[deg]	Zero-lift angle of attack
δ	[m]	Distance between the collocation points
θ	[deg]	Torsional rotation/deformation
θ_b	[deg]	Structural blade pitch angle
$\dot{\theta}$	[deg/s]	Torsional velocity
$\ddot{\theta}$	[deg/s^2]	Torsional acceleration
κ	[m^{-1}s^{-2}deg^{-1}]	Aerodynamic stiffness
ρ	[kg/m^3]	Air density
ω	[Hz]	Frequency (of the vibration)
ω_f	[Hz]	Natural flap-wise frequency
ω_t	[Hz]	Natural torsional frequency
ω_v	[Hz]	Vibration frequency
$\omega_{v,e}$	[Hz]	Frequency of the edge-wise vibration
Ω	[RPM]	Rotor speed

Abbreviations

AC	Aerodynamic center
BW	Backward whirling
C	Aerodynamic damping matrix
CG	Center of gravity
COP	Center of pressure
CP	Collocation point
'DRV'	Collective edge-wise
'E'	Edge-wise
EA	Elastic Axis
EOM	Equations of motion
'F'	Flap-wise
FW	Forward whirling
FFT	Fast Fourier Transform
K	Aeroelastic stiffness matrix
'LA'	Lateral
L_{LA}	Lagrangian
'LO'	Longitudinal
M	Structural mass matrix
PSD	Power spectral density
Q	Vector containing the external forces and moments about the elastic axis due to L and M_{EA}, respectively
'T'	Tower
X_b	X-axis blade root reference system
Y_b	Y-axis blade root reference system
Z_b	Z-axis blade root reference system

Chapter 1 INTRODUCTION

Appearances are deceptive. This is common knowledge, yet many perceive wind turbines as steady rotating energy converters. However, upon closer look it becomes evident not all is as calm as it seems. As wind turbines get larger, so do their blades. As a consequence aeroelastic phenomena such as classical flutter, where flap and torsion vibration of the blade couple with each other resulting in an increase in amplitude, may become relevant. These phenomena are related to the mutual interaction between the structure and the aerodynamic forces. Each is a function of the other. To be more precise, aeroelasticity focuses on the interaction between inertial, elastic and aerodynamic forces. This is depicted in the Collar Triangle, shown in Figure 1.1.

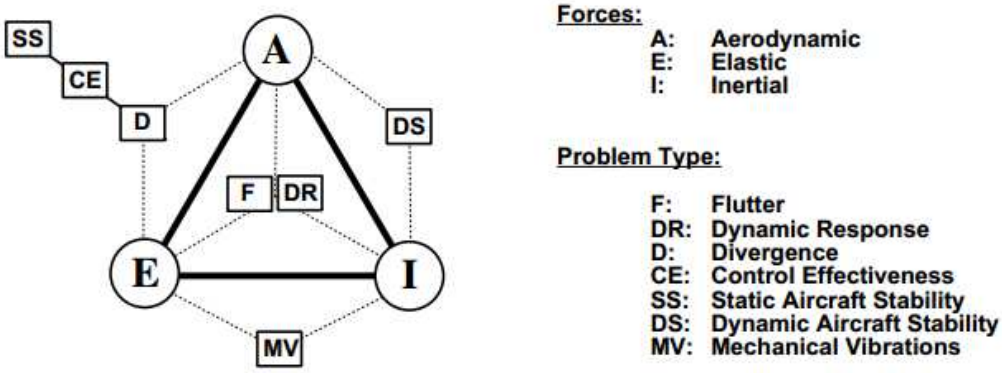

Figure 1.1: Collar's Triangle [1].

Classical flutter is considered a dynamic instability boundary problem, which means that there is a specific rotational speed boundary beyond which the fluid-structure interaction becomes unstable. For classical flutter this boundary is the flutter speed. Due to the wind turbine blades getting larger, the possibility of the blades approaching the flutter speed is increased. Upon surpassing this boundary, the consequences can be catastrophic leading to failure of the wind turbine. Therefore it is essential to find this boundary. To analyze classical flutter ECN has several aeroelastic tools at its disposal, such as BLADEMODE V.2.0 and PHATAS which are used in this project. Both tools can be used in the shell-program FOCUS 6 but BLADEMODE V.2.0 can also be used in the stand-alone version. Developed for the verification of the eigenmodes of a single rotating rotor blade, BLADEMODE V.2.0 was developed at ECN Wind Energy. Subsequently it was altered to make it possible to make a prediction of the aeroelastic stability. The rotor blade used in the analysis follows engineering bending theory of beams and the structural mechanical properties of the blade are a function of the span-wise coordinate only. The analysis of this program is frequency based and providing the required input data of a wind turbine model, this makes it possible to find the natural frequencies for increasing wind or rotor speeds and consequently produce a Campbell diagram. BLADEMODE v2.0 omits the relative phase between the deformation components, hence there is no coupling possible between the flap-wise and torsional modes and this is not visible in the diagram. However there is a possibility that the frequencies of these two modes approach one another as the rotor speed increases. Therefore it may still be possible to find a flutter limit, especially when using the results from PHATAS for the same wind turbine model to compare against. This possibility is founded on the argument that with increasing rotor speed, the flap-wise natural frequencies will increase as a result of the centrifugal stiffening. Contrary to this, the theory of BLADEMODE v2.0 predicts that the torsional natural frequencies will decrease with increasing rotor speed. Therefore, it is expected that the flap-wise and torsional natural frequencies should approach one another in a Campbell diagram.

Whether or not BLADEMODE V.2.0 can be used to predict classical flutter depends on the results from the analysis done with PHATAS, which provides comparison data for the same wind turbine model. The main difference with BLADEMODE V.2.0 is that PHATAS is a non-linear time domain simulation, while BLADEMODE V.2.0 performs a frequency based analysis. Another difference is that PHATAS analyses the dynamic behavior and the corresponding loads in the main components of a wind turbine such as the rotor blades, the rotor shaft and the tower. Based on the non-linear beam approach, most of the bending and torsion flexibilities of the blades and the tower are described in the structural model of the wind turbine in PHATAS. Both BLADEMODE V.2.0 and PHATAS are not only relevant with regard to determining if classical flutter occurs and compare their respective results, but especially regarding how this limit can be deduced in a precise manner. Considering the catastrophic effect this phenomena has on a wind turbine, it is essential to find this limit. As such, the purpose of this thesis *to find a clear and efficient procedure to analyze the flutter speed.*

The limitations of BLADEMODE V.2.0 and PHATAS and validity of the operating conditions are considered. Having obtained the results, a comparison between the results of both programs is performed and the validity of the approach and possible differences are explained.

This thesis consists of seven chapters starting with the introduction in Chapter 1. The second chapter provides a solid base for the theoretical understanding of the classical flutter phenomena. Chapter 3 provides a description of BLADEMODE V.2.0 which is used in the analysis. Also, the simulations performed are described. The structure of Chapter 4 is similar, the only difference being that now PHATAS is considered as this is also used for the analysis. Subsequently Chapter 5 and 6 provide the results following from both BLADEMODE V.2.0 and PHATAS, respectively. Finally Chapter 7 contains the conclusions and recommendations.

Chapter 2 CLASSICAL FLUTTER THEORY

In this section the theoretical background for classical flutter will be provided. It will be explained how classical flutter may be detected when considering the modes of vibration for wind turbine blades via a Campbell diagram, or when looking at the time history behavior of a specific parameter relevant for classical flutter. These tools are applied to an actual wind turbine blade to analyze the if classical flutter occurs, which is discussed in Chapter 5 and Chapter 6.

Before one can use the aforementioned tools, it is necessary to provide an explanation how these tools are obtained and used in the classical flutter analysis. To this extent, the first section discusses modes of vibration and mode shapes, while the second section gives an illustration of and elaboration on the terminology used when describing the directions in which a blade may deform. The third section deals with the definition of classical flutter. A deeper analysis of classical flutter is provided in the fourth section by elaborating on the instability mechanism behind the phenomenon. Criteria related to the occurrence of classical flutter are presented in the fifth section. The sixth section provides the tools used to analyze the occurrence of classical flutter, which are a Campbell diagram as well as the time history behavior of a specific parameter relevant for classical flutter.

2.1 MODES OF VIBRATION AND MODE SHAPES

The modes of vibration are inherent properties of a structure which only change when physical properties, such as mass or stiffness, or the boundary conditions change [2][3]. As such, the aerodynamic forces influence the mode of vibration as they can add stiffness and damping. This is elaborated on in sections 2.3 and 2.4. Furthermore centrifugal stiffening will add stiffness depending on the rotational speed of the wind turbine rotor blades. A mode of vibration consists of a mode shape with a corresponding modal frequency and damping coefficient [4]. The mode shape is defined as the pattern of motion or behavior of the structure of a mode of vibration at a specific frequency and is unique as far as the shape is concerned [5][6]. Examples of modes of vibration for a wind turbine blade are the edge-wise and flap-wise bending modes, as well as the torsional blade modes. Each mode of vibration has a first and higher order blade mode, each with its own modal frequency and damping. Considering the flap-wise bending mode, this can be illustrated with Figure 2.1. Here the first three flap-wise modes are shown. It should be noted that in reality a turbine mode is a combination of two or more modes of vibration.

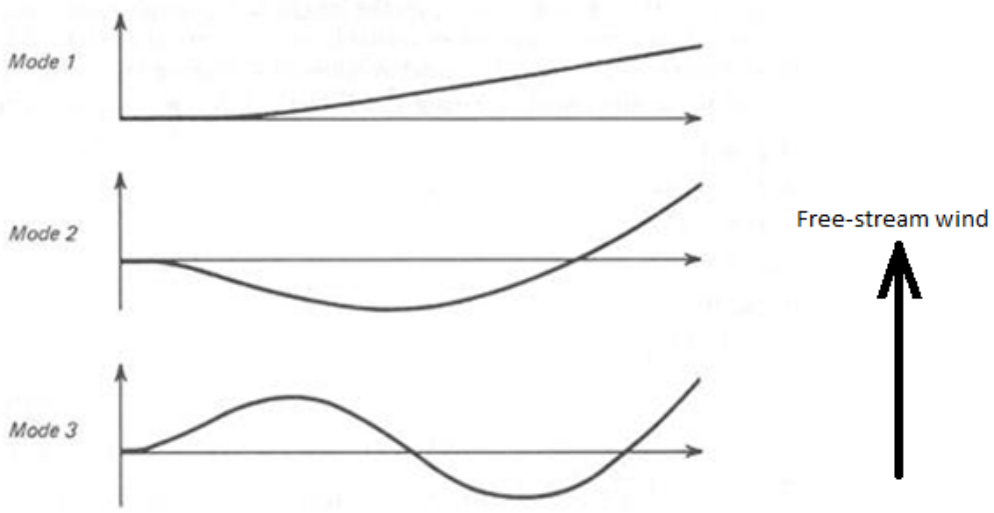

Figure 2.1: Mode shapes for 1st, 2nd, 3rd and 4th flap-wise bending modes [7]. Top view with blade clamped at hub.

The same can be done again for the mode shapes, but this time visualized for a wind turbine blade, as shown in Figure 2.2 and Figure 2.3. It must be noted that this only provides a graphic illustration of the mode shapes and the blade is not drawn to scale nor does it represent an actual wind turbine blade. Furthermore for clarity reasons the structural blade twist is omitted.

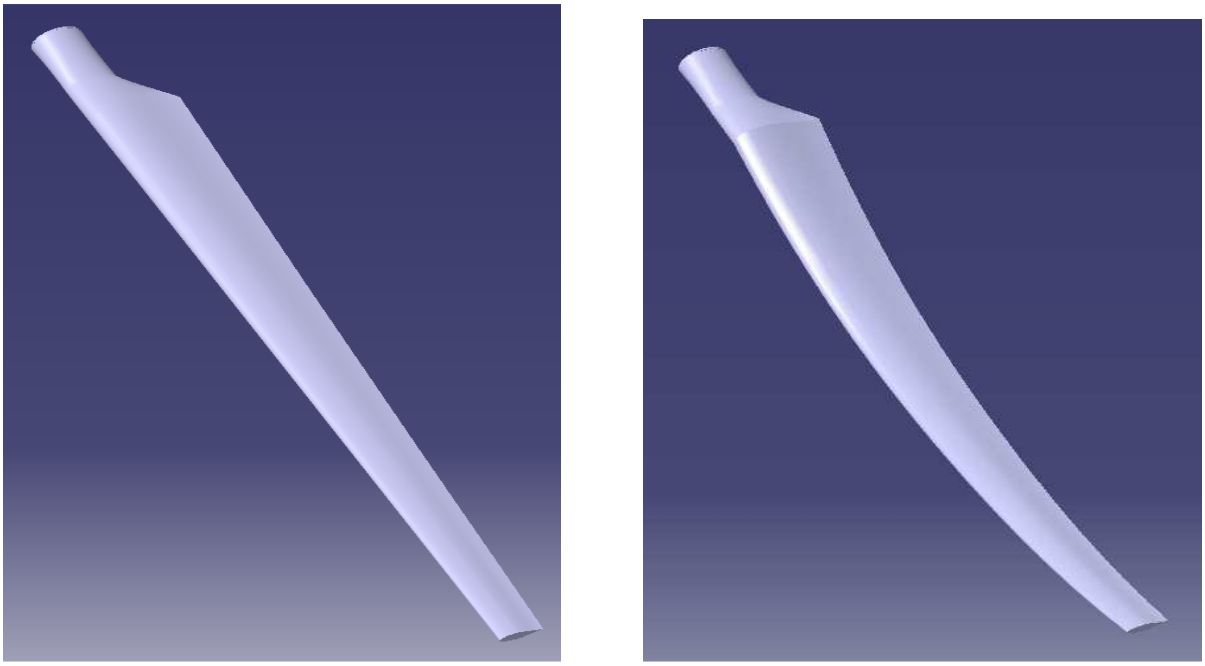

Figure 2.2: Isometric views of the undeformed wind turbine blade (left) and same wind turbine blade with the 2nd flap-wise bending moment (right).

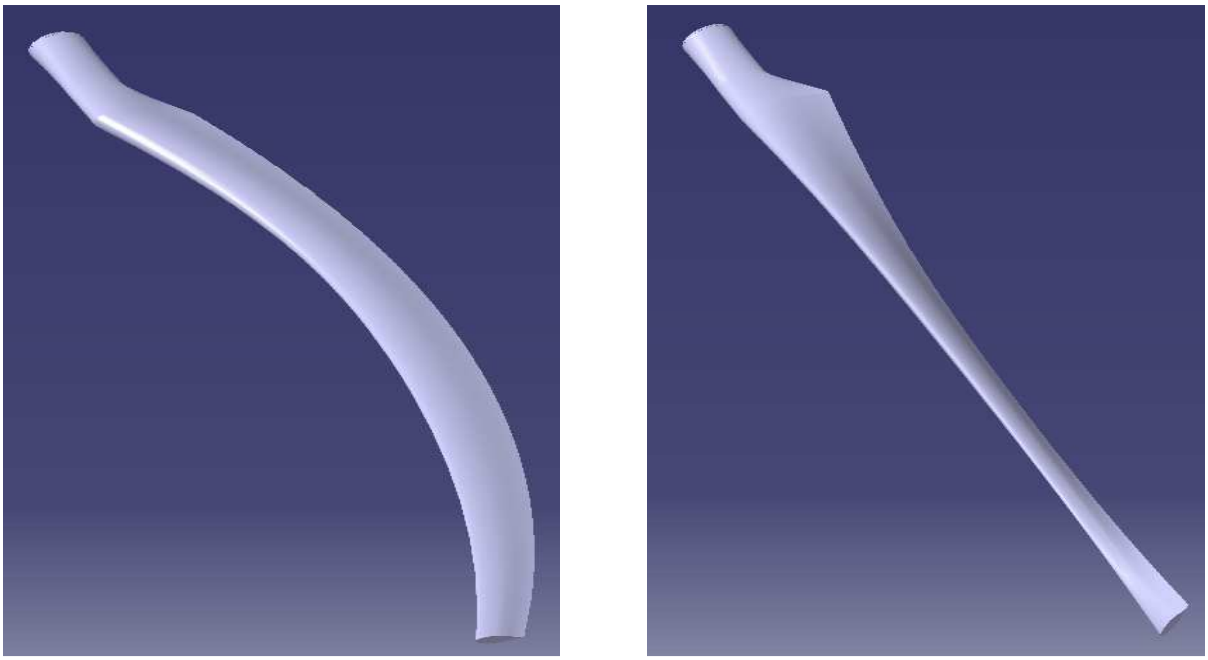

Figure 2.3: Isometric views of the wind turbine blade with the 2nd edge-wise bending moment (left) and with the 2nd torsional blade mode (right).

It is chosen to present the 2nd order modes of vibration for wind turbine blades, in order to provide the reader with an illustration of a higher order mode. Also, by choosing the 2nd order modes the clarity of the illustrations is deemed to remain sufficient, with respect to providing a better understanding of blade bending modes. To give a better perspective of the 2nd order modes of vibration for wind turbine blades, Figure 2.4 and Figure 2.5 are provided.

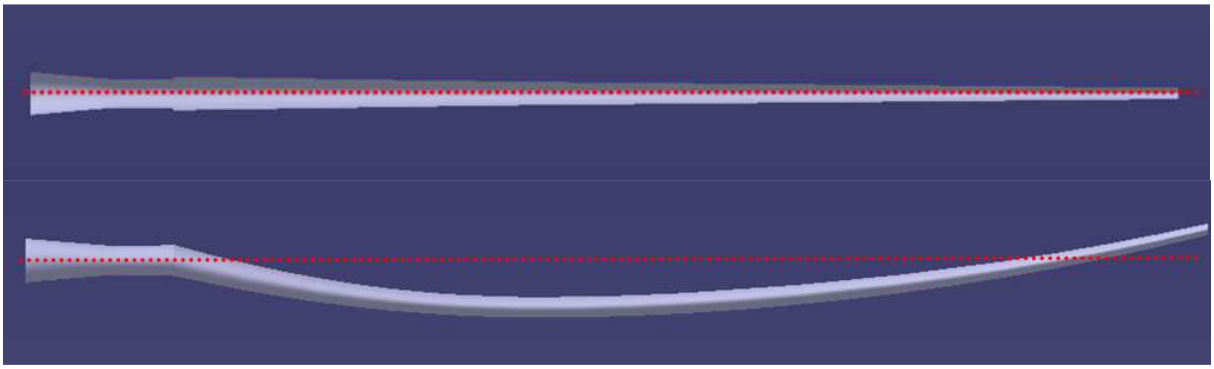

Figure 2.4: Front view of the undeformed wind turbine blade (top) and of the wind turbine blade undergoing the 2nd flap-wise bending moment (bottom).

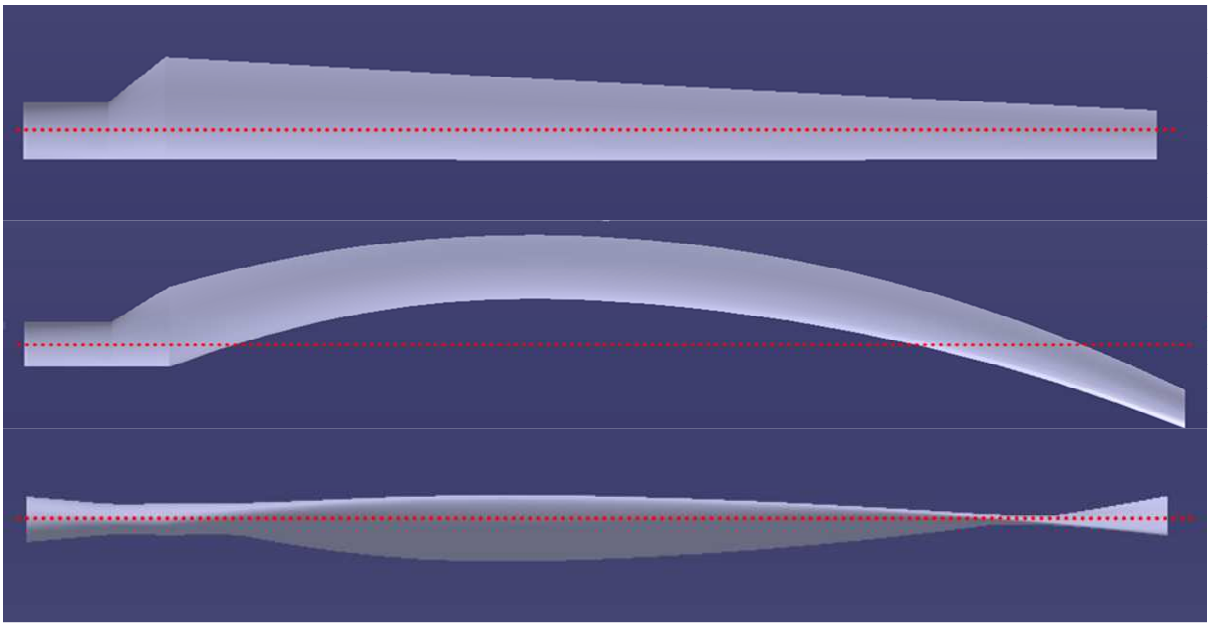

Figure 2.5: Top view of the undeformed wind turbine blade (top), the wind turbine blade undergoing the 2nd edge-wise bending moment (middle) and with the 2nd torsional blade mode (bottom).

The red dotted line present in both figures represents an orientation line such that the deformations are clear. Comparing to Figure 2.2 (left plot), one can see in the bottom plot of Figure 2.5 that the leading edge goes up first above the red line, after which it decreases below the red dotted line. Vice versa for the trailing edge. Referring to Figure 2.1, this is then recognized as the 2nd torsional mode.

2.2 TERMINOLOGY FOR BLADE DEFORMATIONS

Now that a basic explanation of the modes of vibration is given, the next step is to provide the terminology and sign convention used for blade movements or deformations [8].

The movement associated with the edge-wise bending mode concerns movement along the direction of the local chord *c* and is defined positive in the rotational direction. Movement perpendicular to the local chord is related to the flat-wise bending mode and positive in the downwind direction. Furthermore, movement parallel or perpendicular to the plane of rotation is associated to the lag- or flap-wise bending modes respectively. In this case movement downwind is determined to be positive and movement in the rotational direction is considered to be negative. It is worth noting that the deformations related to the edge- and flat-wise modes are defined in the local blade reference frame, while deformations related to the lag- and flap-

wise modes are defined in the blade root reference system [9]. The difference between both reference frames is the structural blade pitch angle θ_b, which usually is relatively small [10]. Therefore flat-wise deformations ≈ flap-wise deformations. Both reference systems are presented in Figure 2.6 for a clockwise rotating wind turbine, as seen from the front. Furthermore there is an uniform wind velocity of $U_0(1-a_{ind})$ and a velocity due to the rotation of the blade $\Omega r(1-a')$ present in the figure. Here U_0 is the free-stream wind velocity, r is the radial position along the blade span, Ω is the rotational velocity, a_{ind} is the axial induction factor and a' is the tangential induction factor.

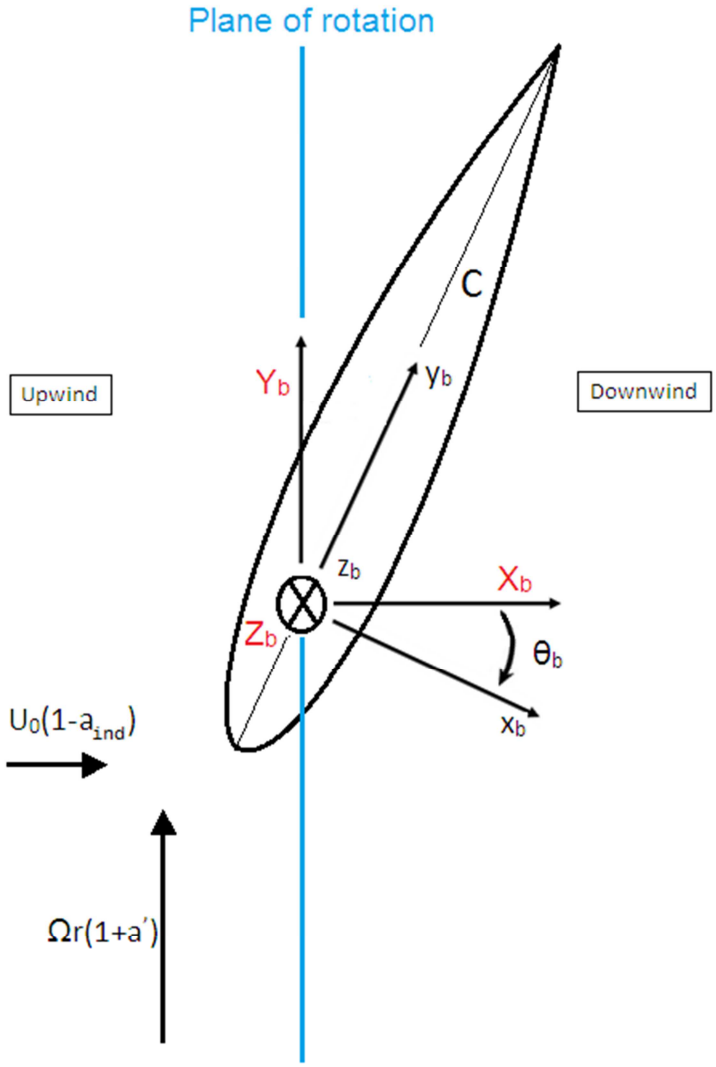

Figure 2.6: Blade root reference system (red capitals) and local blade reference system (black lowercase), with z-axis running from blade root to tip.

In Figure 2.6 the axes indicated with red capital letters are for the blade root reference system, while the axes for the local blade reference system are indicated with lowercase black letters. It is worth noting that regardless of the reference system the blade z-axis is the same in Figure 2.6. This is because here the undeformed blade is considered. The blade z-axis runs through the elastic axis, so when deformation occurs the z-axis in the blade root reference system differs from the one in the local blade reference system.

The terminology and sign convention for the relevant modes of vibration, which will appear in this report, are presented in Figure 2.7 for clarity reasons. In Figure 2.7 also the torsional deformation or rotation θ is illustrated, related to the torsional mode. This deformation is

positive according to the right-hand rule. So if the torsional mode increases θ it is considered positive.

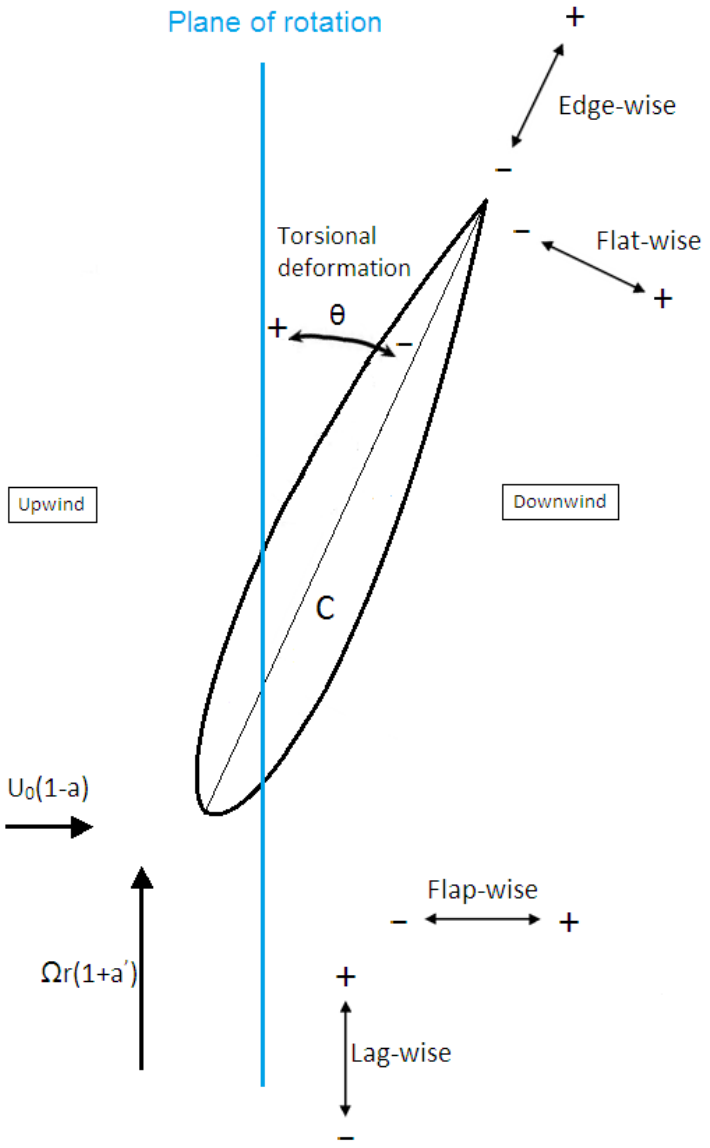

Figure 2.7: Terminology and sign convention for the displacements and rotations.

2.3 DEFINITION CLASSICAL FLUTTER

Classical flutter is defined as a violent instability where a torsional blade mode couples to a flap-wise bending mode via aerodynamic forces, resulting in a rapid growth of the amplitude of the flap-wise and torsional motions due to the flap-wise and torsional modes enhancing each other under influence of the aerodynamic coupling [11][12]. This phenomenon occurs above a critical limit defined as the flutter speed. Below this limit the oscillations will not be sustained, but be damped out. Vice versa for a velocity above this limit, where the damping becomes negative and unstable self-enhancing oscillations can occur. The enhancing takes place if there is attached flow and when the torsional deformation is present, which increases the angle of attack and thus the lift force. As a result of this, the flap-wise deformation increases acting as a stimulus for further torsional deformation. This is evident from Figure 2.8. In this figure it can be seen that increasing lift creates an additional moment about the elastic axis *EA*.

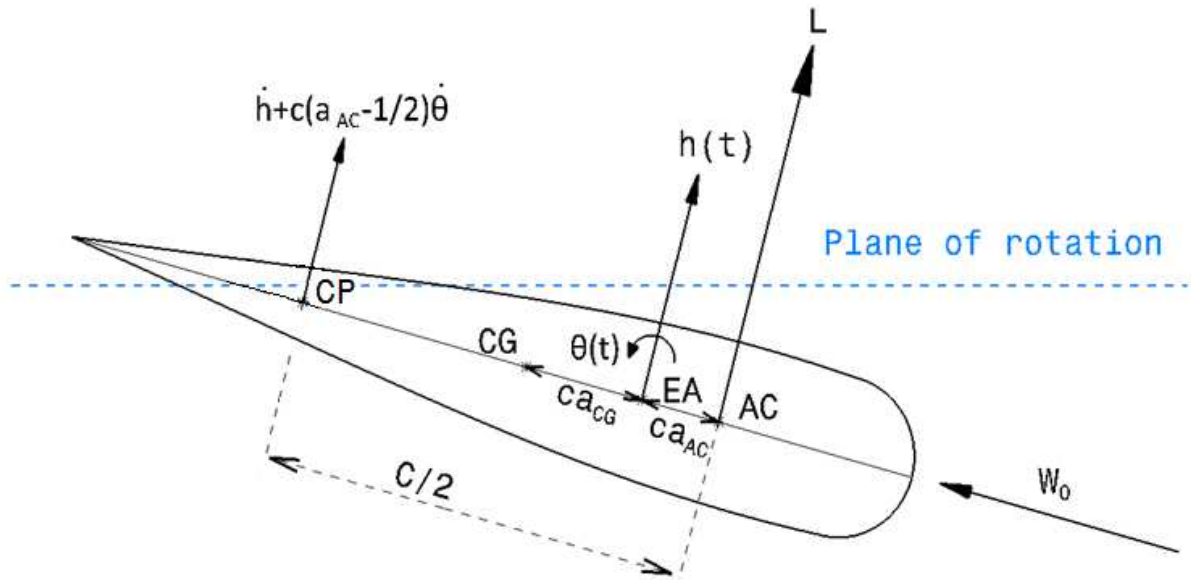

Figure 2.8: Blade section with two degrees of freedom: flap-wise or plunging translation *h(t)* perpendicular to the inflow and rotation *θ*(t) about the elastic axis. Plunging translation and torsional rotation of the airfoil are not illustrated.

In Figure 2.8 a symmetric airfoil is considered and subsequently the camber is neglected, as here only a qualitative analysis is provided. In this figure W_0 is the steady-state relative speed of the inflow. The aerodynamic lift is represented with L and acts at the aerodynamic center AC which is at a distance ca_{AC} in front of the elastic axis and at a quarter chord behind the leading edge. Since a symmetric airfoil is considered, the aerodynamic lift is only present in case of non-zero angle of attack α. Furthermore the elastic axis is at a distance ca_{CG} in front of the center of gravity on the chord CG. Also, in this figure a collocation point CP is defined at 3c/4. Considering that W_0 is parallel to the chord, the angle of attack is zero. This value does not remain zero when the plunging (or flap-wise translation) and torsional rotation of the airfoil, h and θ respectively, are included. These motions cause the collocation point to move with the velocity components indicated with the term $\dot{h} + c(a_{AC} - 1/2)\dot{\theta}$. The airfoil however will experience an air flow velocity in the opposite direction, which will change the angle of attack. To determine which location should be used to capture the effects of the torsional velocity $\dot{\theta}$ on α, it is important to consider the "1/4 – 3/4" rule [13][14][15]. Although not a theoretical law, due to proven sufficient accuracy in practice this rule is widely used. When using a horseshoe vortex to replace a lifting surface such as the airfoil in Figure 2.8, the location of both the vortex and the so-called collocation point is important. This collocation point is where the boundary condition of zero normal flow to the surface must be satisfied and it is found to be at the three-quarter chord [16]. The reason to determine the angle of attack at this collocation point is because the induced velocity has a different value at each chord-wise locations of a section. The angle at three-quarter chord can be considered a representative sectional effective angle of attack [17]. Another important aspect for this location of the collocation point is with regard to the computation of the relative inflow speed. Computing it at this location for small values of the reduced frequency $k = \frac{c\omega}{2W_0}$, makes certain that the equations of Theodorsen for unsteady aerodynamics match those of the Blade Element method [18].

For an asymmetric (cambered) airfoil the lift acts in the center of pressure COP. However, the location of the COP is not fixed but alters with changing angle of attack which makes the analysis complicated. This problem can be solved by translating the lift to the aerodynamic center together with an accompanying pitch moment, accounting for the moment the lift force creates about the aerodynamic center when applied at the center of pressure. The aerodynamic center is assumed to be at the quarter-chord location from the leading edge, which is its approximate

location for symmetric airfoils. This translation makes analysis easier, as for most low speed airfoils the magnitude of the pitching moment about the aerodynamic center remains nearly constant with changing angle of attack [19]. When computing the moment about the elastic axis one must thus also include this pitching moment, next to the moment the lift force creates about this axis. So the total moment due to the lift force about the elastic axis is a sum of both components. However, using a symmetric (non-cambered) airfoil means that the pitching moment about the aerodynamic center is equal to zero. Thus omitting this pitch moment only simplifies the understanding of classical flutter without changing the principle behind the phenomenon.

The derivation of the term $\dot{h} + c(a_{AC} - 1/2)\dot{\theta}$ is based on the location of the collocation point and applying the flap-wise translation and torsional rotation about the elastic axis, as depicted in Figure 2.9.

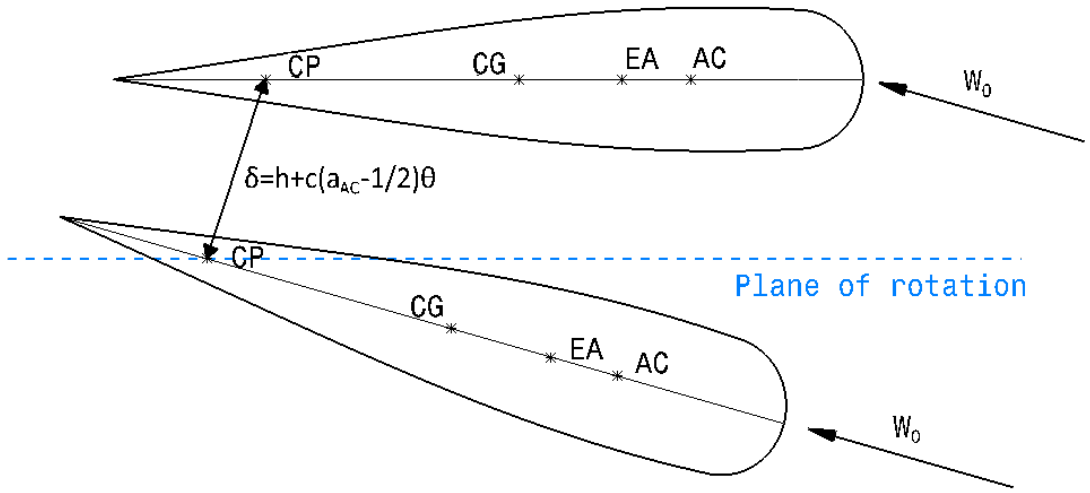

Figure 2.9: Motion of the symmetric airfoil due to the flap-wise translation and torsional rotation.

In Figure 2.9 the flap-wise translation and torsional rotation are applied compared to Figure 2.8, causing W_o to be inclined with an angle θ with respect to the chord. The bottom airfoil is the case of no translation and rotation. It must be noted that the line connecting the two collocation points, indicated with δ, is not perpendicular to the chord at both points. This is because there is also the torsional deformation. Furthermore, in Figure 2.9 the angle of this line as well as the flap-wise translation and torsional deformation is exaggerated for clarity reasons. Assuming small (initial) torsional deformations, the distance δ between the two collocation points can be deduced. First the distance between the collocation point and the elastic axis is determined. This distance is equal to $c(1/2 - a_{AC})$, and it rotates with an angle θ. Now multiplying this distance with the torsional rotation θ yields $c(1/2 - a_{AC})\theta$, which is the translation of the collocation point in the direction of h. However, this translation is in the negative h-direction. Combined with the positive flap-wise translation h, the total translation in the flap-wise direction becomes $\delta = h + c(a_{AC} - 1/2)\theta$. Taking the time derivative of δ, yields the velocity of the collocation point in the flap-wise direction as indicated in Figure 2.8.

Considering that the angle of attack is calculated at the collocation point, the velocity components due to the flap-wise translation and torsional rotation can be determined. Due to positive the flap-wise translation, the airfoil experiences a velocity component in the opposite direction of h. Thus the velocity component of the airflow due to the flap-wise motion at the collocation point remains $\dot{h}$, but now in the negative h-direction. For the torsional rotation the collocation point had a flap-wise velocity component equal to $c(a_{AC} - 1/2)\dot{\theta}$ in the negative h-direction. The airfoil experiences this same velocity component, but only in the positive h-direction.

Based on this definition and description it is indeed evident for the case of classical flutter, how a torsional rotation can increase the angle of attack, subsequently the lift force and as a result of this the flap-wise deformation which then acts as a stimulus for further torsional rotation.

Another way of looking at this enhancement is by considering that work is done on the structure when the lift and vertical speed (or speed in the flap-wise direction) of the blade section have the same sign. The vertical speed for a typical airfoil section is graphically depicted in Figure 2.10, as well as the torsional velocity $\dot{\theta}$ of the airfoil. It must be noted that in Figure 2.10 the vertical speed is represented by $\dot{z}$ instead of $\dot{h}$, because this figure is based on aircraft analysis and not on wind turbines. Nevertheless, the same principle holds for wind turbines and therefore the conclusions that can be drawn based on Figure 2.10 are equally valid for the wind turbine case.

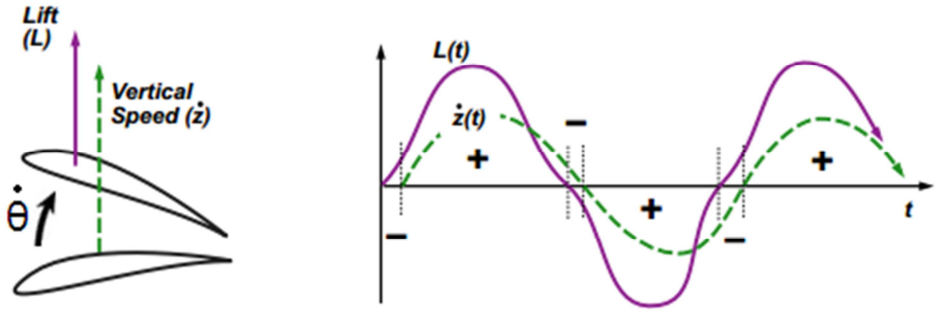

Figure 2.10: Timing of the vertical motion and aerodynamic lift force [1].

Figure 2.10 shows that the regions where energy is added to the structure are considered positive and are indicated with a '+' sign. Vice versa for damping of the structure. For classical flutter the key lies in the fact that the timing of the motion in θ and h over one cycle results in $\int L(t)\,\dot{z}(t)dt > 0$ [1]. Simply put, there are more positive regions than negative regions. When this is the case, the level of vibration increases resulting in a self-exciting oscillation [20]. With regard to this, the location of the center of gravity from the blade elastic shear center is an essential coupling factor [11].

Focusing on the timing of the torsion and flap-wise motion, it can be stated that there must be a substantial phase difference between the two motions. This is because this phase difference makes it possible for the structure to extract energy from the passing airflow at the flutter speed in such a manner that flutter occurs [21][22]. To quantify this phase difference, consider Figure 2.11.

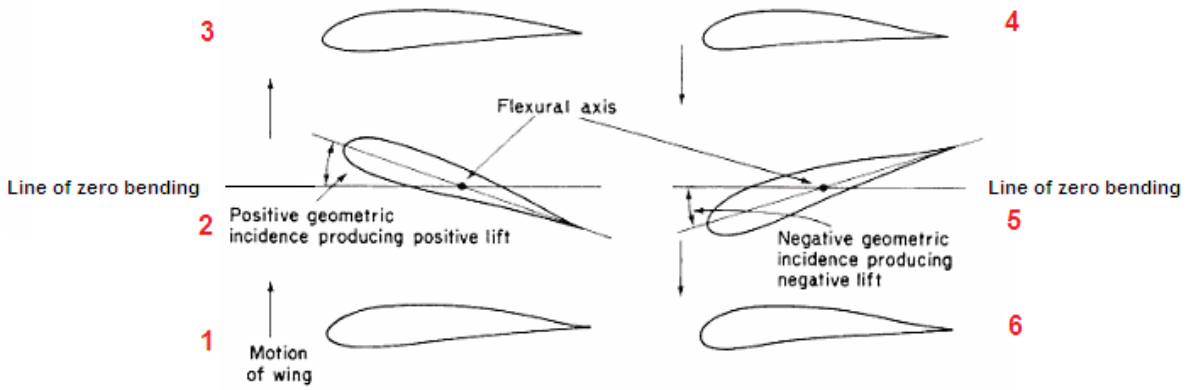

Figure 2.11: Coupling of bending and torsional oscillations and its destabilizing effect [23]. Blade positions 1-3 show the first half of the cycle.

From Figure 2.11 it can be deduced that in case of flap-torsion coupling, there is a 90° phase difference because the maximum torsional deformation occurs at the line of zero bending. The opposite is also true. This phase difference has also been found to be different from 90° in some practical cases [23]. Again it must be stated that Figure 2.11 is based on aircraft analysis but the principle behind and conclusions from the figure are equally valid for the wind turbine case. Next to this, when torsion lags the flap-wise plunging or displacement, it signals flutter [24]. This phase difference will be considered in Chapter 5 and Chapter 6, using BLADEMODE V.2.0 and PHATAS respectively, to check if classic flutter occurs in the analysis.

2.4 Instability Mechanism Classical Flutter

Now that the definition of classical flutter has been provided and elaborated on, a deeper analysis of the instability mechanism behind classical flutter is provided in this section based on Hansen [13] and Hulshoff [1]. Based on the linear equations of motion for the airfoil section, the flutter limit is derived. The analysis provided in this section serves to provide a qualitative analysis based on quasi-steady aerodynamics and without apparent mass terms, which is sufficient to understand the instability mechanism [1]. When considering unsteady aerodynamics, oscillations of the airfoil cause vortices to be shed at the trailing edge of the airfoil. The time history of this vortex sheet influences the angle of attack and thus the aerodynamic forces. In quasi-steady aerodynamics this effect is neglected, which is allowed in this qualitative analysis. For a deeper understanding on vortices the reader is referred to Anderson [25].

In order to deduce the linear equations of motion for the plunging and pitching motion of the airfoil section, the Lagrange's equation should be solved. In order to set up the Lagrangian L_{LA}, a structural model for the airfoil presented in Figure 2.8 and Figure 2.9 is constructed.

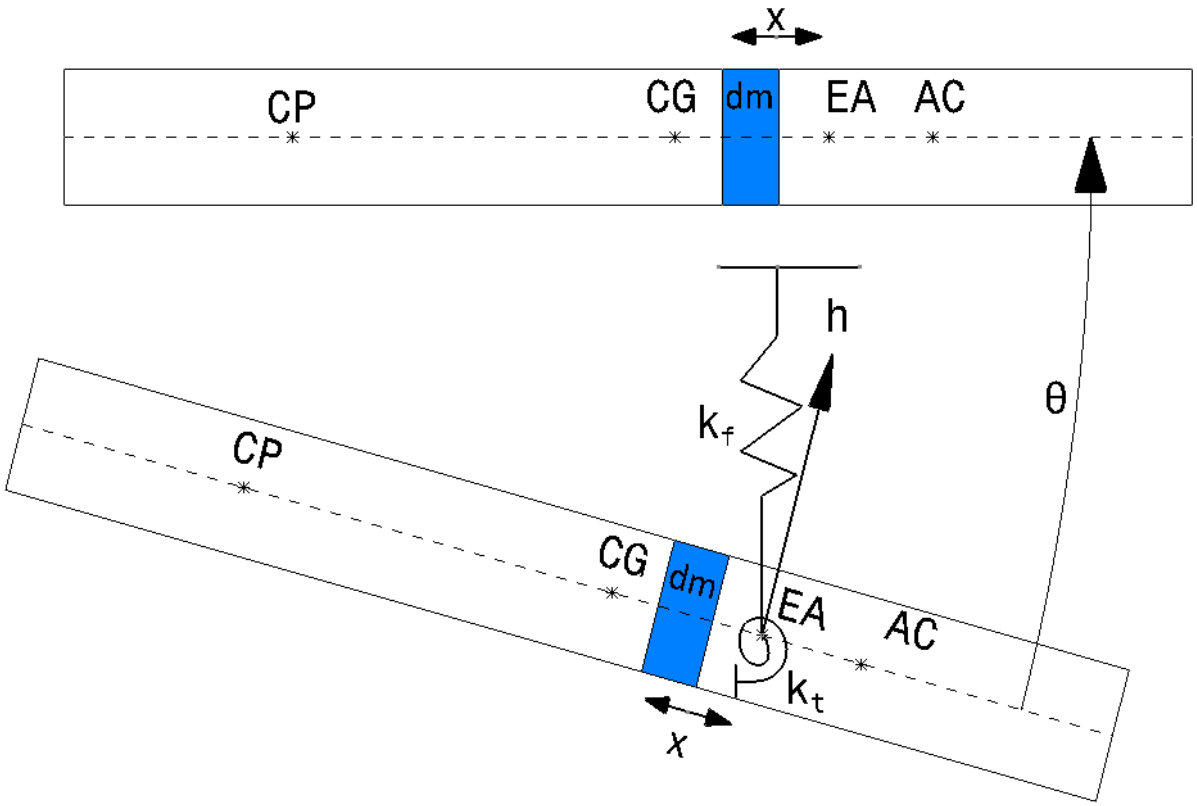

Figure 2.12: Structural model for flap-wise translation *h* and torsional rotation *θ* used to set up the Lagrangian.

In Figure 2.12 x represents the distance between the mass element dm and the elastic axis. Furthermore the two springs are indicated with k_f and k_t, which stand for the flap-wise and torsional stiffness. Based on this structural model with 2 degrees of freedom the Lagrangian can be set up.

$$L_{LA} = T - V \tag{2.1}$$

In this equation V is the potential energy of the airfoil section. Next to this, T is the total kinetic energy of the airfoil section and it can be deduced based on the kinetic energy of the mass element, as a result of the flap-wise $\dot{h}$ and torsional velocity $\dot{\theta}$ [26].

$$dT = \frac{1}{2} dm\left(\dot{h} + x\dot{\theta}\right)^2 \tag{2.2}$$

Now the total kinetic energy for the airfoil section can be determined.

$$T = \frac{1}{2} m\left(\dot{h}^2 + 2x\dot{h}\dot{\theta} + x^2\dot{\theta}^2\right) = \frac{1}{2} m\dot{h}^2 + mx\dot{h}\dot{\theta} + \frac{1}{2} mx^2\dot{\theta}^2 \tag{2.3}$$

In equation (2.3) the static and mass moment of inertia about the elastic axis, S_θ and I_θ respectively, can be recognized [27].

$$T = \frac{1}{2} m\dot{h}^2 + S_\theta \dot{h}\dot{\theta} + \frac{1}{2} I_\theta \dot{\theta}^2 \tag{2.4}$$

Now that the total kinetic energy for the airfoil section is determined, the potential energy will be analyzed. This consists of the energy stored in the springs. It is the flap-wise and torsional stiffness, k_f and k_t respectively. It must be noted that the gravity can be neglected with respect to these two stiffness components, as there are only small changes in the position of the airfoil based on small angle approximations. The position of the CG does not alter enough for it to create the necessity to be included in the potential energy term.

$$V = \frac{1}{2} k_f h^2 + \frac{1}{2} k_\theta \theta^2 \tag{2.5}$$

Having determined the potential energy, the Lagrangian can be constructed.

$$L_{LA} = T - V = \frac{1}{2} m\dot{h}^2 + S_\theta \dot{h}\dot{\theta} + \frac{1}{2} I_\theta \dot{\theta}^2 - \frac{1}{2} k_f h^2 - \frac{1}{2} k_\theta \theta^2 \tag{2.6}$$

Using equation (2.6) one can solve Lagrange's equation.

$$\frac{d}{dt}\left(\frac{\delta L_{LA}}{\delta \dot{\boldsymbol{q}}}\right) - \frac{\delta L_{LA}}{\delta \boldsymbol{q}} = \boldsymbol{Q} \tag{2.7}$$

In this equation $\boldsymbol{q}$ is the vector containing the flap-wise translation h and torsional rotation θ, $\boldsymbol{q} = [h\ \theta]^T$. Also, $\boldsymbol{Q}$ is the vector containing the external forces and moments about the elastic axis, L and M_{EA} respectively. Substituting the derived quantities, equation (2.7) can be solved.

$$\frac{d}{dt}\left(m\dot{h} + S_\theta\dot{\theta} + S_\theta\dot{h} + I_\theta\dot{\theta}\right) - \left(-k_f h - k_\theta\theta\right) = \boldsymbol{Q} \tag{2.8}$$

$$m\ddot{h} + S_\theta\ddot{\theta} + S_\theta\ddot{h} + I_\theta\ddot{\theta} + k_f h + k_\theta\theta = \boldsymbol{Q} \tag{2.9}$$

Now x is placed at the CG, where a point mass can be located, such that S_θ becomes the static moment of inertia of the CG about the elastic axis. Referring to Figure 2.8, $S_\theta = mca_{CG}$. The definition of the mass moment of interia about the elastic axis, using the parallel axis theorem, is provided in equation (2.10) [28][29].

$$I_\theta = I_{CG} + md^2 \tag{2.10}$$

In equation (2.10) I_{CG} is the mass moment of inertia about the axis through the CG and d represents the perpendicular distance between an axis through the CG and the parallel axis. Now applying this equation to case illustrated in Figure 2.8:

$$I_{CG} = mR_{g,CG}^2 \tag{2.11}$$
$$md^2 = m(ca_{CG})^2 = mc^2a_{CG}^2 \tag{2.12}$$

In equation (2.11) $R_{g,CG}$ is the radius of gyration about the CG. Normalizing $R_{g,CG}$ with the chord c yields $R_{g,CG}=cr_{CG}$, resulting in equation (2.13).

$$I_{CG} = mR_{g,CG}^2 = mc^2r_{CG}^2 \tag{2.13}$$

Combining equations (2.10)-(2.13) yields:

$$I_\theta = I_{CG} + md^2 = mc^2(r_{CG}^2 + a_{CG}^2) \tag{2.14}$$

Having determined the expressions for S_θ and I_θ, the sign convention needs to be considered. Forces in the positive h-direction, as indicated in Figure 2.8, are considered positive. Similar for moments about the elastic axis, which are considered positive when creating a pitch-up motion. Having found the necessary expressions and determined the sign convention, equation (2.9) can be solved further.

$$m\ddot{h} - mca_{CG}\ddot{\theta} - mca_{CG}\ddot{h} + mc^2(r_{CG}^2 + a_{CG}^2)\,\ddot{\theta} + k_f h + k_\theta \theta = \boldsymbol{Q} \tag{2.15}$$

Rewriting this solution to obtain linear equations of motion for both the forces in the flap-wise direction and moments about the elastic axis, results in equations (2.16) and (2.17).

$$Forces: \quad m\ddot{h} - mca_{CG}\ddot{\theta} + k_f h = L \tag{2.16}$$
$$Moments: \quad -mca_{CG}\ddot{h} + mc^2(r_{CG}^2 + a_{CG}^2)\ddot{\theta} + k_t\theta = ca_{AC}L \tag{2.17}$$

In both equations the external force vector $\boldsymbol{Q}$ has been substituted with L and $M_{EA}=ca_{AC}L$, where the latter expression is the moment about the elastic axis due to the lift force which acts at the aerodynamic center.

Continuing with finding the flutter limit, an expression for the quasi-steady aerodynamic lift force per unit length on the airfoil is desired, in order to solve the equations of motion. This definition is provided in equation (2.18).

$$L = \frac{1}{2}\rho W^2 c C_L(\alpha) \tag{2.18}$$

In this expression ρ is the air density and C_L is the lift coefficient, which is a function of the angle of attack. Also, W is the relative speed and it is defined below together with the angle of attack.

$$W = \sqrt{W_0^2 + \dot{h}^2} \tag{2.19}$$

Here W_0 is practically parallel to the chord, at small angle of attack values. This small angle of attack is due to the small value of θ. The last term in equation (2.18) is the angle of attack, which is provided in equation (2.20).

$$\alpha = arctan\left(\frac{W_0 sin\theta - \dot{h} - c\left(\frac{1}{2} - a_{AC}\right)\dot{\theta}}{W_0 cos\theta}\right) \tag{2.20}$$

In this equation the term between brackets is deduced based on Figure 2.13, which is a result of what has been depicted and analyzed in Figure 2.8 and Figure 2.9.

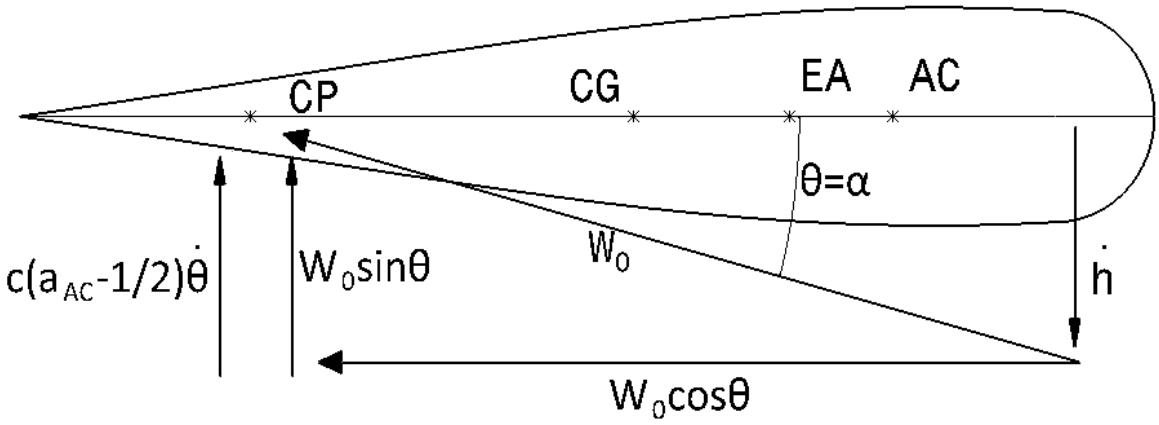

Figure 2.13: Velocity vectors at the collocation point including the flap-wise and torsional velocity used to determine the angle of attack.

It should be noted that in Figure 2.13 the velocity vectors are not drawn to scale but serve to clarify the derivation of the angle of attack. Adding the velocity vectors in the flap-wise direction yields $W_0 sin\theta - \dot{h} - c\left(\frac{1}{2} - a_{AC}\right)\dot{\theta}$, while the velocity vectors added in the direction parallel to the chord add up to $W_0 cos\theta$. Dividing the two terms does indeed yield the same result as in equation (2.20).

Now assuming small values for θ, $\dot{h}$ and $\dot{\theta}$ leads to the expression for the linear lift.

$$L \approx L_0 + \frac{1}{2} c\rho W_0^2 C_L' \left(\theta - \frac{\dot{h}}{W_0} - \left(\frac{1}{2} - a_{AC}\right)\frac{c\dot{\theta}}{W_0}\right) \tag{2.21}$$

Recognizing the fact that camber was neglected, the value for steady-state lift L_0 equals zero. Next to this, C_L' is the gradient of the lift curve evaluated at α_0=0, which implies that equation (2.21) is only valid for moderate angles of attack. For high values of α, approaching the stall region, this linear relationship between C_L' and α is lost.

Now that the formulation of the linear lift force is determined, the focus is put again on the linear equations of motion presented in equations (2.16) and (2.17). These equations can be rewritten into a matrix format, using the vector $\boldsymbol{x} = \left[{}^{h}/_{c}, \theta\right]^T$. To obtain the matrices, the following derivation is performed. First equation (2.16) is divided by *mc*.

$$\frac{\ddot{h}}{c} - a_{CG}\ddot{\theta} + \frac{k_f}{m}\frac{h}{c} = \frac{\rho W_0^2 C_L' \theta}{2m} - \frac{\rho W_0 C_L' \dot{h}}{2m} - \frac{c\rho W_0 C_L' \dot{\theta}}{4m} + \frac{a_{AC} c\rho W_0 C_L' \dot{\theta}}{2m} \tag{2.22}$$

Useful relations in the further derivation of the EOM are provided right below:

$$\omega_f = \sqrt{k_f/m} \tag{2.23}$$

$$\kappa = \frac{\rho}{2m} W_0^2 C_L' \tag{2.24}$$

Here ω_f stands for the natural frequency of the flap-wise mode. Furthermore k_f stands for the flap-wise bending stiffness. Equation (2.24) provides an expression for the aerodynamic stiffness κ, which amongst others is dependent on the air-section mass ratio ρ/m.

Applying equations (2.23) and (2.24) to equation (2.22):

$$\frac{\ddot{h}}{c} - a_{CG}\ddot{\theta} + \omega_f^2 \frac{h}{c} + \frac{c\rho W_0 C_L' \dot{\theta}}{4m} - \frac{a_{AC} c\rho W_0 C_L' \dot{\theta}}{2m} - \frac{\rho W_0^2 C_L' \theta}{2m} + \frac{\rho W_0 C_L' \dot{h}}{2m} = 0 \tag{2.25}$$

$$\frac{\ddot{h}}{c} - a_{CG}\ddot{\theta} + \omega_f^2 \frac{h}{c} + \frac{c\kappa}{2W_0}\dot{\theta} - \frac{c\kappa a_{AC}}{W_0}\dot{\theta} - \kappa\theta + \frac{c\kappa}{W_0}\frac{\dot{h}}{c} = 0 \tag{2.26}$$

$$\frac{\ddot{h}}{c} - a_{CG}\ddot{\theta} + \frac{c\kappa}{W_0}\left(\frac{1}{2} - a_{AC}\right)\dot{\theta} - \kappa\theta + \frac{c\kappa}{W_0}\frac{\dot{h}}{c} + \omega_f^2 \frac{h}{c} = 0 \tag{2.27}$$

Now focusing on equation (2.17), the following derivation is performed. A useful relation with respect to this EOM is the expression for the natural frequency of the torsional mode ω_t, which is provided in equation (2.28).) Here there is no inertia coupling, which means that a_{CG}=0.

$$\omega_t = \sqrt{k_t/(mc^2 r_{CG}^2)} \tag{2.28}$$

In equation (2.28) k_t stands for the torsional stiffness.

Using equations (2.24), (2.28) and dividing the EOM in equation (2.17) with mc^2:

$$-a_{CG}\frac{\ddot{h}}{c} + (r_{CG}^2 + a_{CG}^2)\ddot{\theta} + \frac{k_t}{mc^2}\theta = \frac{\rho a_{AC} W_0^2 C_L' \theta}{2m} - \frac{\rho a_{AC} W_0 C_L' \dot{h}}{2m} - \frac{\rho c a_{AC} W_0 C_L' \dot{\theta}}{4m} + \frac{\rho a_{AC}^2 c W_0 C_L' \dot{\theta}}{2m} \tag{2.29}$$

$$-a_{CG}\frac{\ddot{h}}{c} + (r_{CG}^2 + a_{CG}^2)\ddot{\theta} + r_{CG}^2\omega_t^2\theta = -\frac{c\kappa}{2W_0}a_{AC}\dot{\theta} + \frac{a_{AC}^2 c\kappa}{W_0}\dot{\theta} + a_{AC}\kappa\theta - \frac{a_{AC}c\kappa}{W_0}\frac{\dot{h}}{c} \tag{2.30}$$

$$-a_{CG}\frac{\ddot{h}}{c} + (r_{CG}^2 + a_{CG}^2)\ddot{\theta} + \frac{c\kappa}{W_0}\left(\frac{a_{AC}}{2} - a_{AC}^2\right)\dot{\theta} - a_{AC}\kappa\theta + \frac{a_{AC}c\kappa}{W_0}\frac{\dot{h}}{c} + r_{CG}^2\omega_t^2\theta = 0 \tag{2.31}$$

Finally considering the derivatives of $\boldsymbol{x}$:

$$\dot{\boldsymbol{x}} = \begin{bmatrix} \dot{h}/_c, \dot{\theta} \end{bmatrix}^T \tag{2.32}$$

$$\ddot{\boldsymbol{x}} = \begin{bmatrix} \ddot{h}/_c, \ddot{\theta} \end{bmatrix}^T \tag{2.33}$$

Having performed the derivation, the matrices can be constructed as shown in equation (2.34).

$$\begin{bmatrix} 1 & -a_{CG} \\ -a_{CG} & r_{CG}^2 + a_{CG}^2 \end{bmatrix}\begin{bmatrix} \ddot{h} \\ \ddot{\theta} \end{bmatrix} + \frac{c\kappa}{W_0}\begin{bmatrix} 1 & \frac{1}{2} - a_{AC} \\ a_{AC} & a_{AC}\left(\frac{1}{2} - a_{AC}\right) \end{bmatrix}\begin{bmatrix} \dot{h} \\ \dot{\theta} \end{bmatrix} + \begin{bmatrix} \omega_f^2 & -\kappa \\ 0 & r_{CG}^2\omega_t^2 - \kappa a_{AC} \end{bmatrix}\begin{bmatrix} h \\ \theta \end{bmatrix} = \mathbf{0} \tag{2.34}$$

Starting with the matrix on the most left-hand side and continuing to the right, equation (2.34) contains the structural mass, aerodynamic damping and aeroelastic stiffness matrices respectively. The shorter matrix notation of equation (2.34) is presented in equation (2.35).

$$\boldsymbol{M}\ddot{\boldsymbol{x}} + \boldsymbol{C}\dot{\boldsymbol{x}} + \boldsymbol{K}\boldsymbol{x} = 0 \tag{2.35}$$

The aerodynamic damping matrix may be neglected due to the elements of $\boldsymbol{C}$ being an order of magnitude smaller than the elements of $\boldsymbol{K}$, which describe the change in lift as a result of a torsional rotation θ. The cause for the neglecting of $\boldsymbol{C}$ is based on the fact that for wind turbines the value for W_0 is relatively large, while the section vibrations have moderate frequencies ω. Considering the definition of the reduced frequency, $\boldsymbol{C}$ can be expressed in terms of this factor, it is evident that neglecting the elements of $\boldsymbol{C}$ is allowed for the mentioned conditions [30]. Another reason is, that this section provides a qualitative analysis of the classical flutter mechanism and the small dissipative forces of $\boldsymbol{C}$ are relevant in a quantitative analysis.

Now inserting the solution $\boldsymbol{x} = \boldsymbol{v}e^{\lambda t}$ into equation (2.35) yields the eigenvalue problem given in equation (2.36).

$$(\lambda^2 \boldsymbol{M} + \boldsymbol{K})\boldsymbol{v} = 0 \tag{2.36}$$

In order to find the non-trivial solutions the determinant of $\lambda^2 \boldsymbol{M} + \boldsymbol{K}$ must be zero. The derivation from this determinant to the characteristic equation is presented in equations (2.37)-(2.39)

$$det\begin{bmatrix} \lambda^2 + \omega_f^2 & -\lambda^2 a_{CG} - \kappa \\ -\lambda^2 a_{CG} & \lambda^2 r_{CG}^2 + \lambda^2 a_{CG}^2 + r_{CG}^2 \omega_t^2 - \kappa a_{AC} \end{bmatrix} = 0 \tag{2.37}$$

$$\begin{aligned}&\left(\lambda^4 r_{CG}^2 + \lambda^4 a_{CG}^2 + \lambda^2 r_{CG}^2 \omega_t^2 - \lambda^2 \kappa a_{AC} + \lambda^2 \omega_f^2 r_{CG}^2 + \lambda^2 a_{CG}^2 \omega_f^2 + r_{CG}^2 \omega_f^2 \omega_t^2 - \kappa \omega_f^2 a_{AC}\right) - \\ &(\lambda^4 a_{CG}^2 - \lambda^2 \kappa a_{CG}) = 0\end{aligned} \tag{2.38}$$

$$\lambda^4 r_{CG}^2 + \lambda^2 \left[(r_{CG}^2 + a_{CG}^2)\omega_f^2 + r_{CG}^2 \omega_t^2 - \kappa(a_{AC} + a_{CG})\right] + \omega_f^2 (r_{CG}^2 \omega_t^2 - \kappa a_{AC}) = 0 \tag{2.39}$$

To have a stable solution, the real part of the solution of the characteristic equation must be negative. Based on the Routh-Hurwitz criteria, which states that the real part of the solutions are negative when the coefficients of the polynomial are positive, the following can be deduced from (2.39) [31][32]:

$$(r_{CG}^2 + a_{CG}^2)\omega_f^2 + r_{CG}^2 \omega_t^2 - \kappa(a_{AC} + a_{CG}) > 0 \quad and \quad r_{CG}^2 \omega_t^2 - \kappa a_{AC} > 0 \tag{2.40}$$

The coefficient of λ^4 is always positive and does not need to be considered in equation (2.40). Considering the limit for the first criterion in this equation, while satisfying the second criterion, equation (2.39) can be solved:

$$\lambda^4 r_{CG}^2 + \omega_f^2 (r_{CG}^2 \omega_t^2 - \kappa a_{AC}) = 0 \tag{2.41}$$

$$\lambda^4 = -\frac{\omega_f^2 (r_{CG}^2 \omega_t^2 - \kappa a_{AC})}{r_{CG}^2} = -\gamma^2 \tag{2.42}$$

$$\lambda^2 = i\gamma \tag{2.43}$$

$$\lambda_{1,2} = \pm\sqrt{i\gamma} = \pm\sqrt{i}\sqrt{\gamma} = \pm\frac{\sqrt{2}}{2}(1 + i)\sqrt{\gamma} \tag{2.44}$$

Equation (2.44) proves that there is one complex eigenvalue with a positive real part. Next to this, the presence of its non-zero imaginary part means that the instability is oscillatory. Therefore the first criterion in equation (2.40) provides the flutter limit of the section:

$$\frac{\rho}{2m} W_0^2 C_L' < \omega_f^2 \frac{r_{CG}^2 + a_{CG}^2}{a_{AC} + a_{CG}} + \omega_t^2 \frac{r_{CG}^2}{a_{AC} + a_{CG}} \quad for \quad a_{AC} + a_{CG} \geq 0 \tag{2.45}$$

Here the aerodynamic stiffness has been inserted. If the left-hand side (LHS) of equation (2.45) is larger than the right-hand side (RHS), the risk of flutter is substantial. It is also worth noting that this equation is for quasi-steady aerodynamics.

2.5 Flutter Criteria

After determining the flutter limit of the section, it is important to consider the main criteria related to classical flutter. Then it is possible to compare them with equation (2.45) and see if they indeed lead to an increased risk of flutter. Based on the extensive studies of aircraft wing flutter, it is assumed that a wind turbine runs the risk of experiencing flutter if the following main criteria are met [33][34]:

1. There must be attached flow. If this is not the case, positive blade torsion will not lead to increased lift.

2. There must be high tip speeds. This means that the value for W_0 must be sufficiently high, resulting in higher energy in the aerodynamic forces which 'feed' the flutter mode.

3. There must be low flap and torsion stiffness. Consequently the values of ω_f and ω_t are sufficiently low, such that they can couple in a flutter mode.

4. The location of the CG on the outboard part of the blade must be aft of the aerodynamic center, which will ensure the correct phasing between the flap-wise and torsional components of the flutter.

Considering the first criterion and comparing with equation (2.45), it is clear that the LHS can only be larger than the RHS if there is attached flow. This means that $C_L' > 0$. For the second criterion a similar statement can be made. Only in this case it is the steady-state relative speed of the inflow which must be sufficiently high. Turning the attention to the third criterion, the flutter limit can only be exceeded when ω_f and ω_t are adequately low such that LHS>RHS. Finally the location of the CG must always be aft of the location of the aerodynamic center. If this is not the case, $a_{AC} + a_{CG} < 0$ and the flutter limit inequality in equation (2.45) must be turned, resulting in the fact that new inequality can never be exceeded for attached flow. This new inequality will always be true, and thus the new flutter limit can never be reached.

Next to the 4 main criteria, there are less essential parameters. The first is the air-blade mass ration ρ/m where a low as possible value is desired to reduce the risk of flutter. This is clear based on consulting equation (2.45). Next to this are the blade aspect ratio b/c (where b is the span), material damping and positions of the elastic and shear center which influence structural bending-torsion couplings.

Having determined how to find the flutter limit and the main flutter criteria, it is possible to construct a stability plot where the relation between these criteria and the flutter limit can be illustrated. In order to provide a better understanding of the flutter limit and how it is influenced by the main flutter criteria, a simplified numerical example is provided in Appendix A. Here it should be noted that the values used to create the stability plot do not belong to an actual wind turbine blade. The result of this example can be compared with the analysis done using BLADEMODE V.2.0 and PHATAS for the effect of varying torsional stiffness values on the occurrence of classical flutter. These results are presented in Chapter 5 and Chapter 6, provided that classical flutter indeed occurs in the analysis and thus can be detected.

Similar to this, Chapter 5 and Chapter 6 will also elaborate on the effect of a changing pitch angle on the occurrence of classical flutter.

2.6 Analysis Tools for Classical Flutter

Having discussed the modes of vibration, mode shapes, the definition of classical flutter including its instability mechanism and criteria, this section discusses the tools used to analyze the occurrence of classical flutter. These tools are a Campbell diagram and the time history behavior of a specific parameter relevant for classical flutter. However, before it is possible to construct and understand a Campbell diagram, it is first necessary to further examine blade vibrations and their transformation from the local blade frame to the ground-fixed frame.

When a blade vibrates with a modal frequency ω_v in the local blade frame, the motion of the mass can be described using d'Alembert's Principle as a force. Here a trick is used to reduce the dynamic system to a static equilibrium problem. In effect d'Alembert's Principle states that if the blade is moving or harmonically vibrating in a specific direction, it gives rise to a harmonic inertia force F_i acting with the same magnitude in the opposite direction [35].

$$\sum F - ma = 0 \tag{2.46}$$

Equation (2.46) is the mathematical description of the static equilibrium problem for a vibrating blade. The inertia force has magnitude ma. It must be noted that this does not mean that a dynamic problem can be solved via statics. What has been done is that the resulting differential equations can now be deduced using statics.

Now that the definition of the inertia force has been provided, the transformation to the non-rotating (ground-fixed) reference frame can be performed by for example considering (pure) edge wise bending modes. There are two fundamental edge-wise bending modes, because of the different tilt and yaw stiffness, but once rotating the difference between the two frequencies found for these bending modes is no longer noticeable [36]. The frequency related to these bending modes is indicated by $\omega_{v,e}$. The two fundamental edge-wise mode shapes are depicted in Figure 2.14.

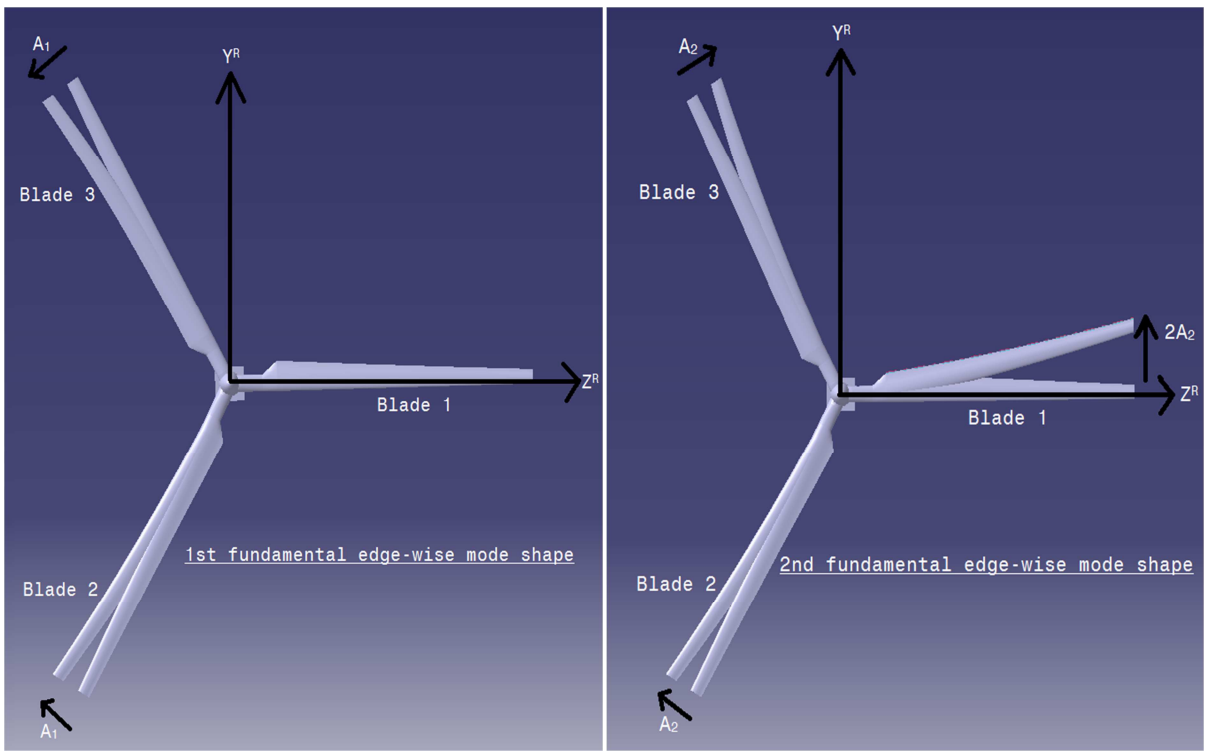

Figure 2.14: First and second fundamental edge-wise mode shapes depicted on the LHS and RHS respectively. The rotating rotor reference frame is indicated by Y^R-Z^R, while the amplitudes for the first and second fundamental edge-wise mode shapes are indicated by A_1 and A_2 respectively. The black arrows show the direction of vibration.

In this figure the rotor reference frame, indicated by Y^R and Z^R, is fixed at the hub and rotates with Ω along with the blades. The first fundamental edge-wise mode shape has blade 2 and 3 vibrating in counter-phase and with equal amplitude A_1. As a result it can be deduced that there is only an in-plane force component of the inertia force in the Z^R-direction. Contrary to this, the second fundamental edge-wise mode shape has blade 2 and 3 vibrating in-phase with each other and with identical amplitude A_2. Blade 1 is vibrating in counter-phase with blades 2 and 3. Also, the amplitude of blade 1 is $2A_2$. It can now be deduced that there is only an in-plane force component of the inertia force in the Y^R-direction. Combining the in-plane force components for both mode shapes, yields a force in both the Y^R- and Z^R-direction. Both these components can be expressed as a sine function, since the inertia force is harmonic. Plotting the two sine functions against each other yields an ellipsoid shape, as depicted in Figure 2.15, since both fundamental edge-wise mode shapes have a different phase.

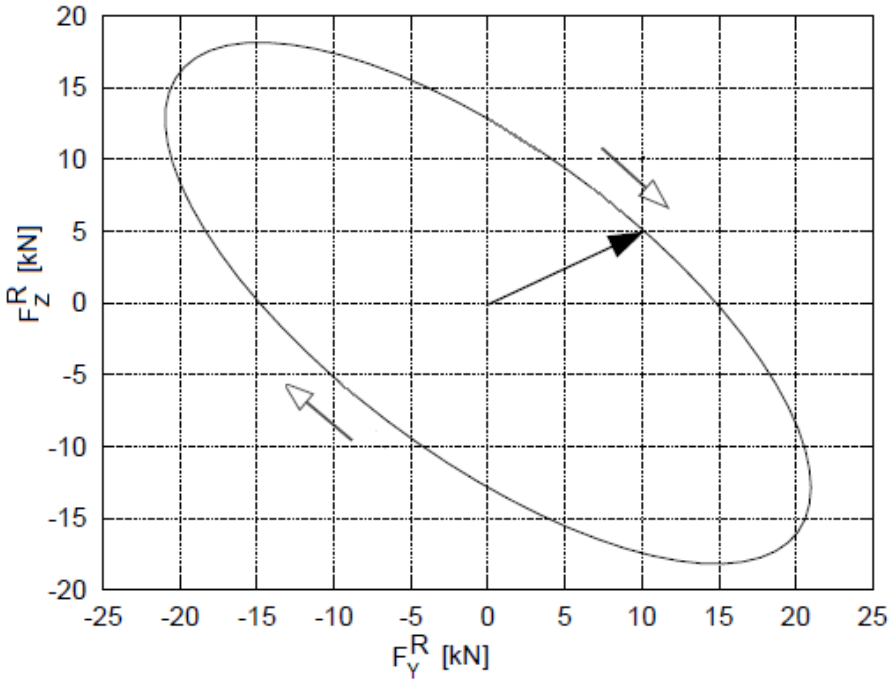

Figure 2.15: In-plane inertia force for the two fundamental pure edge-wise bending modes (with different phase) in rotor coordinates for a three-bladed wind turbine [36].

For a more thorough elaboration, including the mathematical derivation of the inertia force in the rotating rotor coordinate frame, the reader is referred to Petersen, Thomsen & Madsen [36]. In Figure 2.15 the non-filled arrows indicate the direction of rotation of the inertia force, which is indicated with the black arrow and rotates with frequency $\omega_{v,e}$. Furthermore this plot is constructed for the two fundamental pure edgewise vibrations and the superscript of the forces indicates that the inertia force is depicted in the rotating rotor reference frame.

Having transformed the inertia force from the local blade frame to the rotating rotor reference frame, it can now be transformed to the non-rotating reference frame. Since many reference frames have been mentioned in this chapter, for clarity reasons the reference frames mentioned up to this point have been illustrated in Appendix B. It should be noted that the inertia force shown in Figure 2.15 can be decomposed in two counter-rotating circular components. The force component rotating along with Ω is the progressive or forward whirling (FW) force F_p and the other force component is the retrograde or backward whirling (BW) force F_r. These forces are constant in size and depending on the relative size of these two inertia force components, the rotation is deemed FW or BW. Transforming from the rotor coordinate reference frame to the ground-fixed reference frame, results in a frequency splitting of $\pm\Omega$ around the center frequency $\omega_{v,e}$. The frequency of the FW inertia force is increased with Ω, while the frequency of the BW

inertia force is decreased with Ω. These frequencies are associated with the FW and BW modal components of a blade vibration mode. These FW and BW components can be deduced based on Figure 2.16.

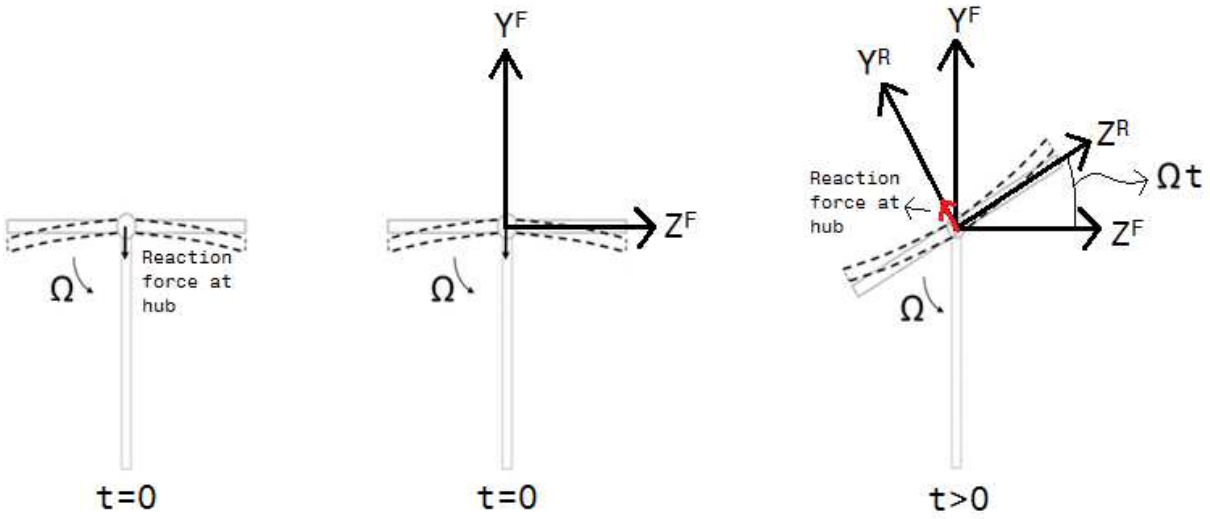

Figure 2.16: Reaction force at the hub for a two-bladed wind turbine due to the inertia force created by the blade vibrations in the edge-wise direction. This force can be considered in the fixed (non-rotating) or rotor (rotating) reference frame, indicated by Y^F-Z^F and Y^R-Z^R respectively. On the right-hand side the reaction force at the hub has been indicated in red for clarity reasons.

In this figure a two-bladed wind turbine is depicted with the reaction force at the hub, as a result of the inertia force created by the blade vibrations. Furthermore, the rotating and non-rotating reference frames are depicted, where the latter is indicated by Y^F-Z^F. The reason for using a two-bladed wind turbine, instead of the three-bladed wind turbine used so far, is based on the fact that in the rotating rotor reference frame no elliptical shape for the inertia force can be constructed, contrary to what was illustrated in Figure 2.15 for the three-bladed wind turbine. Therefore it is less evident how the FW and BW modal components are present, since it is not possible to deduce two counter-rotating circular components of the inertia force in the rotating reference frame. The reason for there not being an elliptical shape of the inertia force can be understood when deducing the components of the reaction force at the hub, or in the non-rotating reference frame.

Based on the assumption of a harmonic blade vibration, the reaction force at the hub can be deduced in its y- and z-components [37]. It should be noted that in Figure 2.16 at t=0 the rotating and non-rotating reference frames coincide. First the reaction force at t=0 is provided in the rotating reference frame in its Y^R- and Z^R-components.

$$F_Y^R = A\,sin(\omega_{v,e}t) \tag{2.47}$$

$$F_z^R = 0 \tag{2.48}$$

In equation (2.47) A stands for the amplitude of the vibration. The reason that $F_Z{}^R$ equals zero in equation (2.48) is due to the fact that a two-bladed wind turbine is considered and a vibration in the edge-wise direction is perpendicular to the Z^R-axis, hence there is no force component in the Z^R-direction. This in contrast to Figure 2.14 and Figure 2.15, where a three-bladed wind turbine was considered. Considering equations (2.47) and (2.48) there are not two sine equations which can be plotted against each other to form an ellipsoid, as was the case for the three-bladed wind turbine depicted in Figure 2.14. Hence, for the two-bladed wind turbine case Figure 2.15 would reduce to a straight line as only $F_Y{}^R$ is present.

Now considering that for t>0 the rotating rotor reference frame will have rotated over an angle Ωt, with respect to the non-rotating reference frame, the reaction force can be decomposed in its Y^F- and Z^F-components.

$$F_Y^F = F_Y^R cos(\Omega t) = A\ sin\left(\omega_{v,e} t\right) cos(\Omega t) \quad (2.49)$$
$$F_Z^F = F_Y^R sin(\Omega t) = A\ sin\left(\omega_{v,e} t\right) sin(\Omega t) \quad (2.50)$$

These equations can be rewritten, which is done in equations (2.51) and (2.52).

$$F_Y^F = A\ sin\left(\omega_{v,e} t\right) cos(\Omega t) = \frac{1}{2} A \sin\left(\left(\omega_{v,e} - \Omega\right)t\right) + \frac{1}{2} A\ sin\left(\left(\omega_{v,e} + \Omega\right)t\right) \quad (2.51)$$
$$F_Z^F = A\ sin\left(\omega_{v,e} t\right) sin(\Omega t) = \frac{1}{2} A \cos\left(\left(\omega_{v,e} - \Omega\right)t\right) - \frac{1}{2} A\ cos\left(\left(\omega_{v,e} + \Omega\right)t\right) \quad (2.52)$$

Equations (2.51) and (2.52) show the FW and BW components of the reaction force at the hub, including the frequency splitting of $\pm\Omega$, when translating the inertia force to the non-rotating reference frame. Using these equations the components of the reaction force at the hub can be determined, which allows the determination of how the rotor c.g. will move during a rotor revolution with respect to Ω. An example of rotor c.g. movement during a rotor revolution is provided in Figure 2.17 for a four-bladed wind turbine.

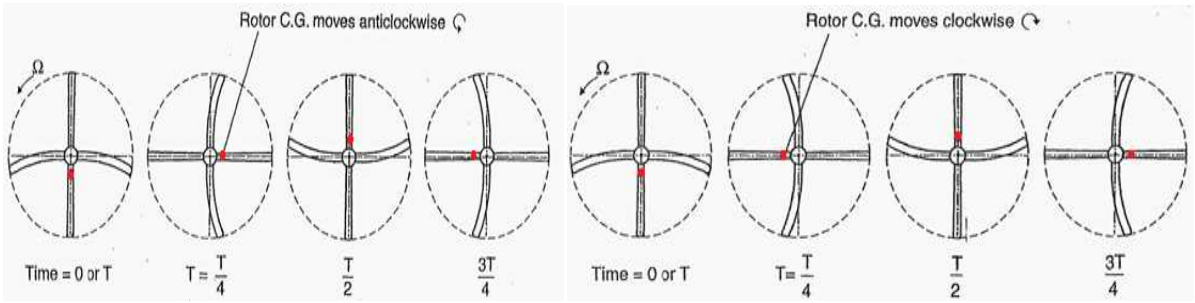

Figure 2.17: Progressive (left) and retrograde (right) 1st edge-wise mode for a four-bladed wind turbine, during a three-quarter period of the oscillation. Red dot represents rotor CG location [38].

Considering the progressive edge-wise mode in this picture, it can be seen that one pair of the blades leads the other pair by a phase of 90 degrees. As a result of this, the CG location of the rotor is not located at the center of the hub. It has an offset which is indicated in Figure 2.17 with a red dot. Furthermore, the rotor CG generally follows an elliptical anti-clockwise rotation and it rotates about the hub center [38]. For the retrograde mode it can be deduced that the pair of blades deformed at time=0 lag the other pair of blades. Hence the rotor CG follows an elliptical clockwise rotation about the hub center.

Now that the transformation of the inertia force to the ground-fixed frame and associated frequency shifts, as well as the rotor c.g. movement have been explained, the emphasis is put on the natural frequencies of the modal components of a (blade) vibration mode in a Campbell diagram. Up to this point an edge-wise bending mode was considered. However, regardless of the (blade) vibration mode, there are almost always three modal components present. The first is the symmetric modal component, where the blades deflect simultaneously in the considered deflection shape with no phase difference and the same amplitude [13]. The frequency of this component is equal to the natural frequency of the mode considered ω_v. The other two modal components are the FW and BW mode, which are asymmetrical meaning that per blade both the phase and amplitude are different at a given moment in time.

Although the FW and BW modes split around ω_v, the symmetric and asymmetric modes do not have the same standstill natural frequency. The standstill frequency of the asymmetric modes is lower due to the different flexibilities of the remaining support structure [36]. Furthermore, the

same is valid when comparing the standstill frequencies of both asymmetric modes. Again, each asymmetric mode is related to a different flexibility, resulting in (slight) differences in the standstill frequencies. These aspects can be illustrated in a Campbell diagram such as in Figure 2.18, where the natural frequencies of the modal components of a (blade) vibration mode are plotted against the rotor speed.

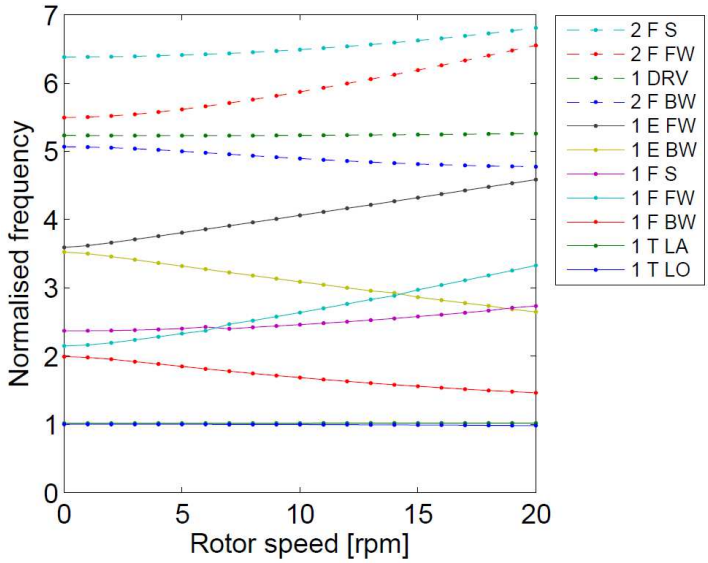

Figure 2.18: Campbell diagram illustrating the modal frequencies of a vibration mode versus the rotor speed [39].

In Figure 2.18, abbreviations *'E'*, *'F'*, *'T'* and *'DRV'* stand for the edge-wise, flap-wise, tower and drive train or collective edge mode of vibration. Furthermore *'LO'*, *'LA'* and *'S'* stand for longitudinal, lateral and symmetric respectively. Also, the frequencies have been normalized with the lowest frequency. From this figure it is evident that for a specific vibration mode there is a difference between the standstill frequencies symmetric and asymmetric modes. Furthermore the splitting of the asymmetric modes is also clear. For increasing Ω, the frequency of the FW modes increases, while the frequency of the BW modes decreases corresponding to the definition of their frequencies. An interesting phenomenon occurs when, for a specific vibration mode, the frequencies of the symmetric and asymmetric modes approach each other. The closer the two gets, the more they attain a modal component of the other. For example, the first FW and symmetric flap-wise mode approach each other at approximately 6,5 RPM. They now both attain a component of the other mode. This can be seen in Figure 2.18 as both lines slightly deflect. What happens is that the lines do not cross, but deflect from each other. Therefore, the line labeled with *'1 F S'* in Figure 2.18, is actually the line of the first FW flap-wise mode beyond 6,5 RPM [39]. It is however assigned with the mentioned label, because considering all rotor speeds for this line, the symmetric component is dominant in the mode. The same is true for the line labeled *'1 F FW'*. As far as two different mode shapes are concerned, such as an asymmetric flap- and edge-wise mode, these do not switch at the crossing point. The reason for this is simply that these mode shapes are too different from each other.

To improve the understanding of symmetric and asymmetric modal components, graphical illustrations are provided in Figure 2.19-Figure 2.24 which are relevant for classical flutter. These figures make it easier to understand and visualize the difference between symmetric and asymmetric modal components for a full wind turbine. It should be noted that the tower movements and hub displacements are neglected as it does not serve the purpose. The black lines in the figures serve to create a better perspective of the blade deformations. An elaboration is proved after the last figure.

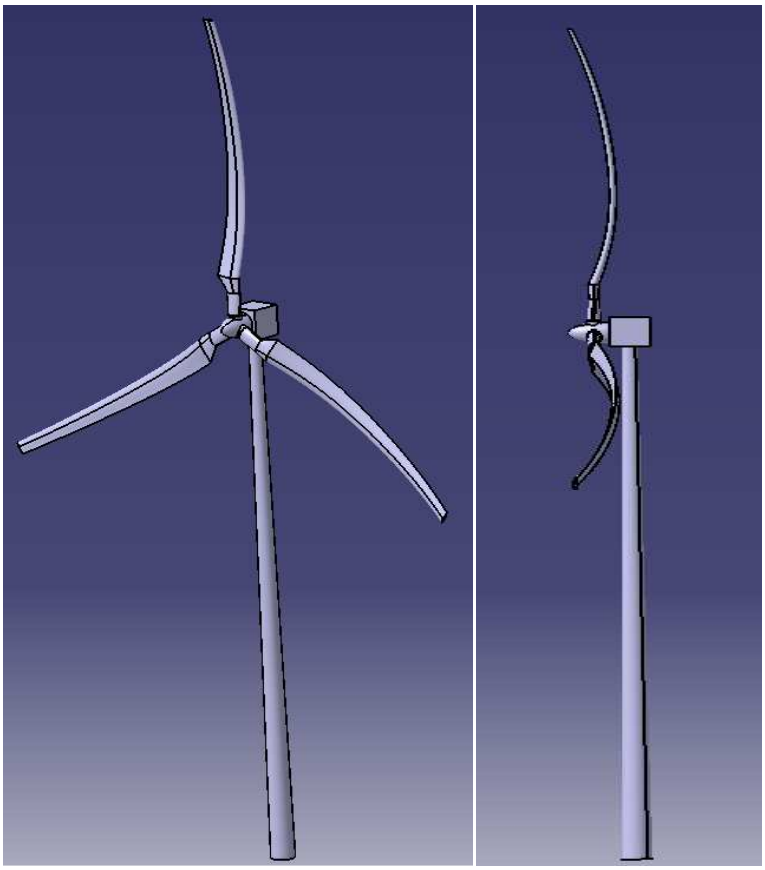

Figure 2.19: isometric (left plot) and side view of the 2nd symmetric flap-wise mode.

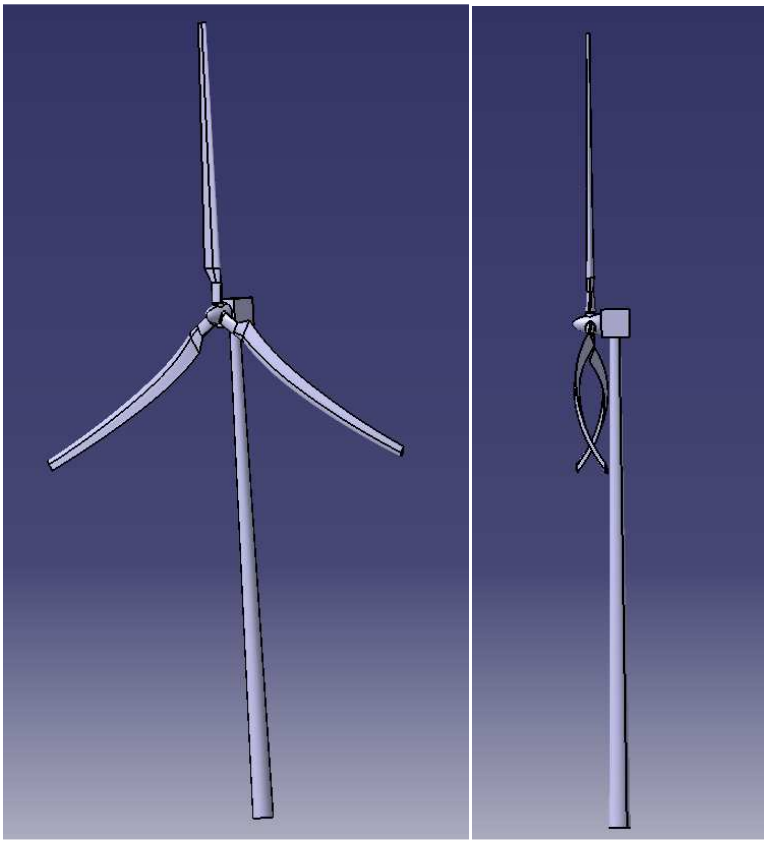

Figure 2.20: Isometric (left plot) and side view of the 2nd flap-wise BW mode.

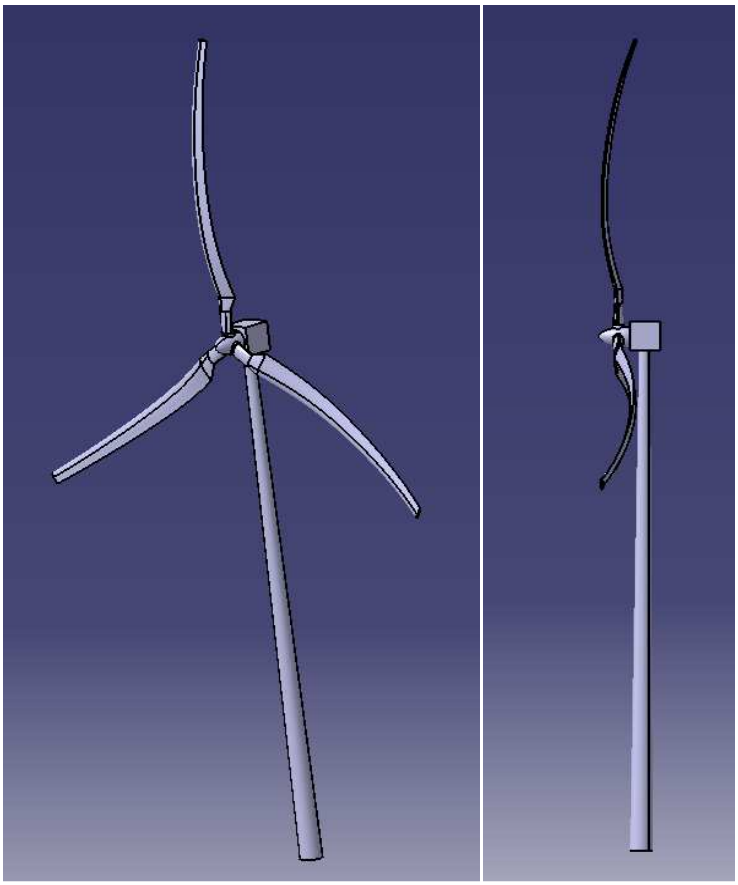

Figure 2.21: isometric (left plot) and side view of the 2nd flap-wise FW mode.

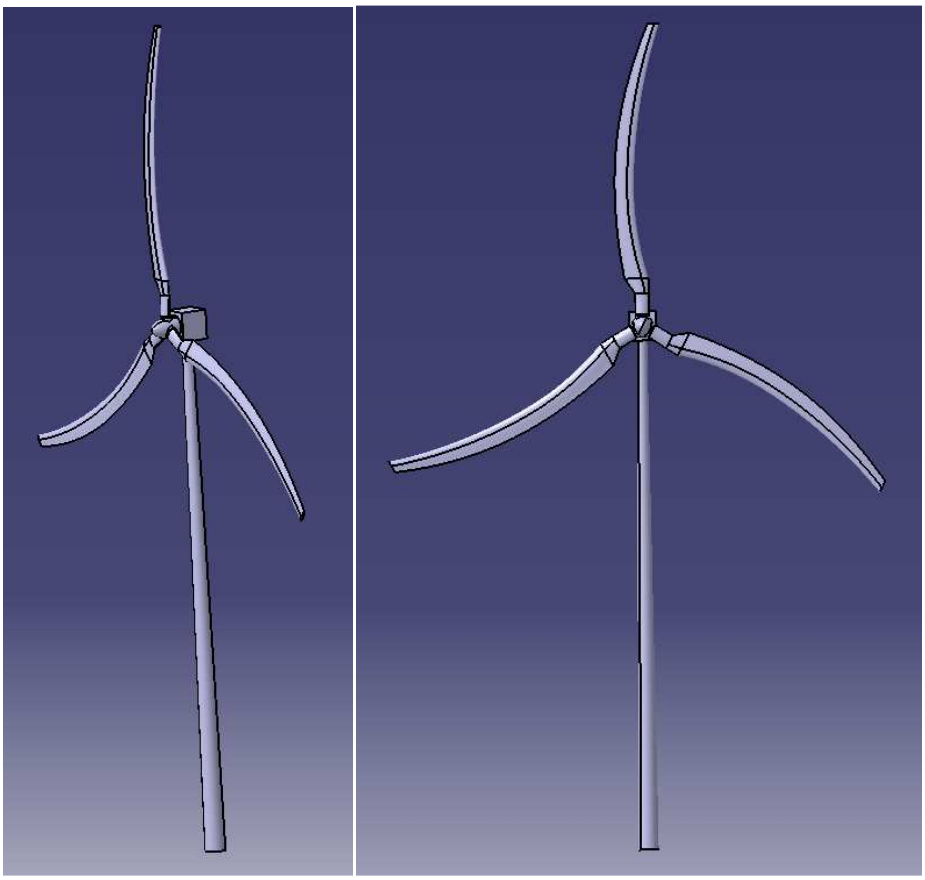

Figure 2.22: isometric (left plot) and front view of the 2nd collective edge-wise mode.

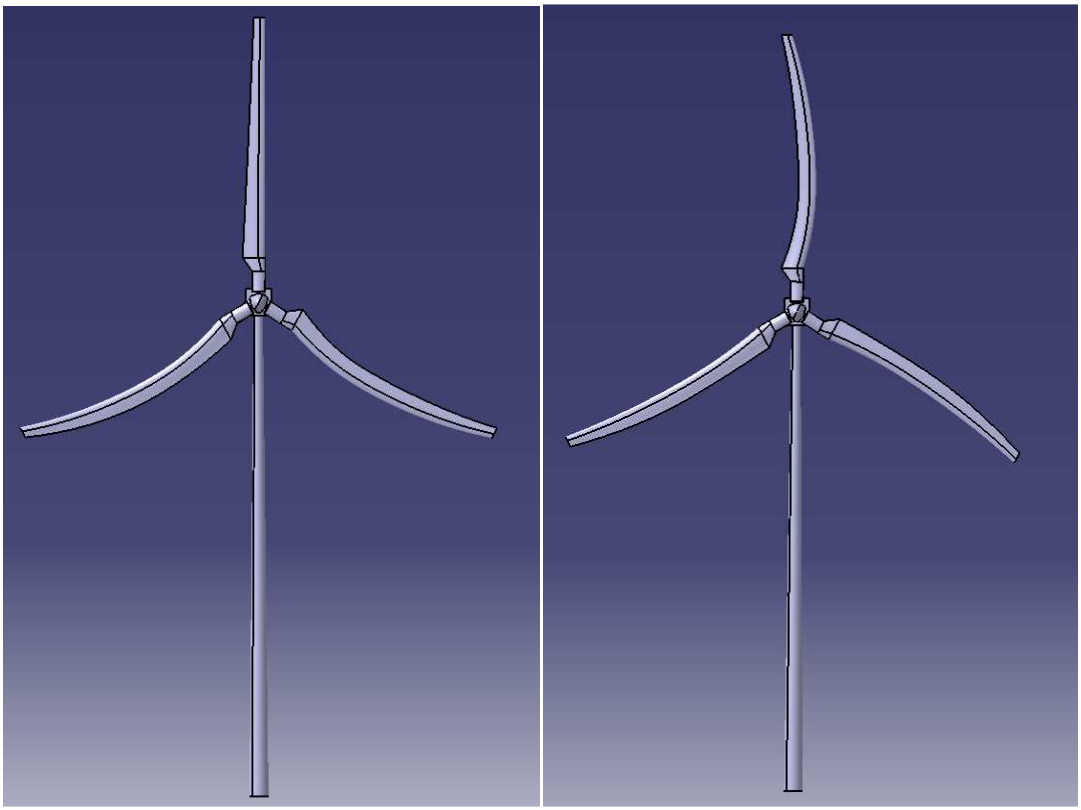

Figure 2.23: Left plot shows the 2nd edge-wise BW mode and the right plot shows the 2nd edge-wise FW mode.

Figure 2.24: Isometric (left plot) and side view of the 2nd symmetric torsion mode.

Considering Figure 2.19, 2.22 and 2.24 it is shown that the blades deform in the same deflection shape, as is expected for the symmetric and collective mode shapes. Figure 2.20 shows the wind turbine with the top blade practically at rest, while the other two blades vibrate in counter-phase with each other. This is especially clear when considering the side view. Now shifting the focus to Figure 2.21, it is clear that the top blade now vibrates in counter-phase with the remaining two blades. These two blades vibrate in the same deflection shape and in-phase. Finally there is Figure 2.23, where the left plot shows the 2nd edge-wise BW mode. Here the top blade is again practically at rest, while the other two blades vibrate in counter-phase with the same amplitude. Contrary to this, Figure 2.24 shows that for the 2nd edge-wise FW mode the top blade vibrates with twice the amplitude of the other two blades. Furthermore the vibration of the top blade in is counter-phase with the in-phase vibration of the other two blades.

Having transformed the inertia force from to the ground-fixed reference frame, considered rotor c.g. movement and explained the modal components of a (blade) vibration mode, the focus can be put on how the coupling of the flap-wise and torsional modes looks like and can be recognized in a Campbell diagram. To this extent, a Campbell diagram based on both a single blade analysis and full turbine analysis is presented in Figure 2.25.

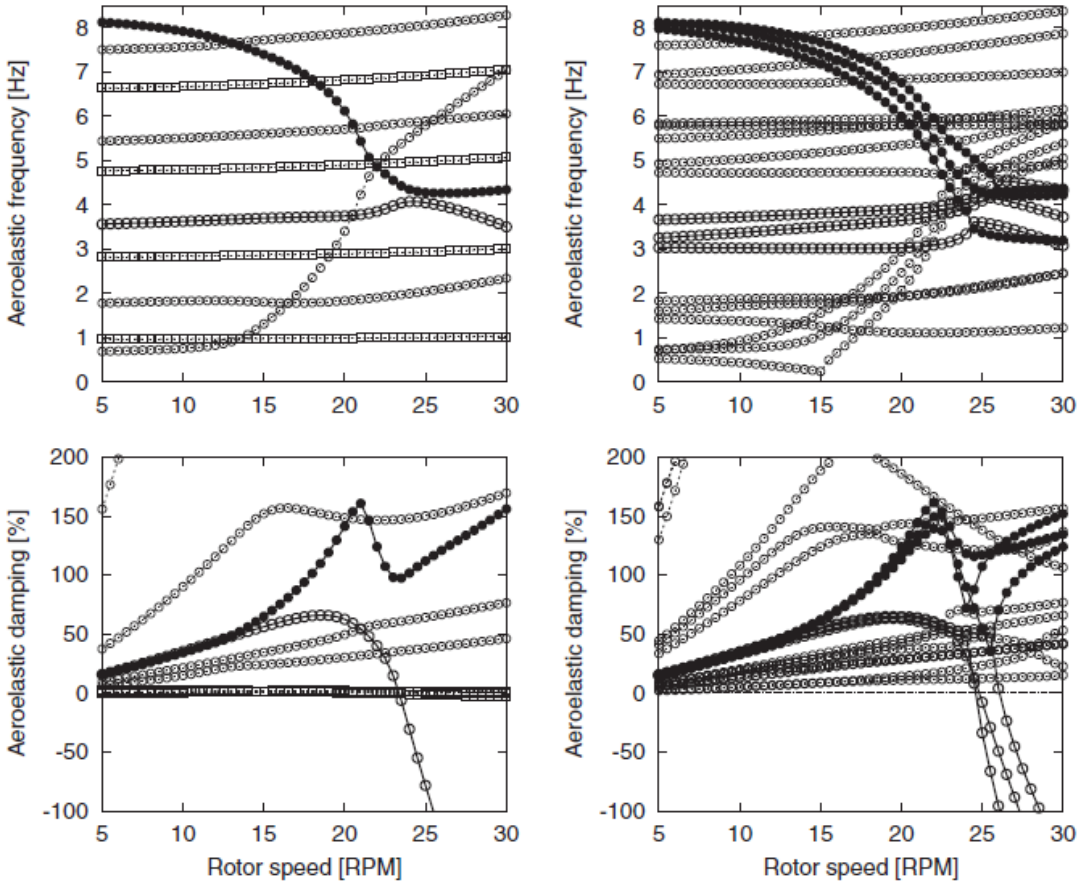

Figure 2.25: The top plots show the natural frequencies, while the bottom plots contain the damping. The flap-wise modes are represented by 'o', while the torsional modes are denoted by '•'. Left plots are for single blade analysis, right plots are full turbine analysis. The conditions of operation are no wind, zero blade pitch and undeformed steady state [40].

The top left plot in Figure 2.25, contains the analysis for one blade. Care should be taken not to confuse the first flap-wise mode as the mode which couples with the first torsional mode, when consulting the top left plot. Although, the first flap-wise mode crosses the line of the torsional mode first, it does not couple into a flutter mode. This is also evident when consulting the bottom left plot, which contains the damping percentage of the blade modes. Here it is clear that

the damping of a flap-wise mode becomes increasingly negative beyond approximately 25 RPM. This indicates a flutter mode. Consulting the top left plot at this rotor speed, it is evident that a coupling occurs between a flap-wise and torsional mode as two lines have approached each other and seem to deflect. This is similar to what happened in Figure 2.18. Counting the number of lines which are indicated with and 'o' and •, it is clear that the third flap-wise mode couples with the first torsional mode.

Similarly, for the full turbine analysis, top right plot, the same coupling occurs at the stated RPM value. Therefore the single blade analysis complies with the full turbine analysis. It should be noted that for the full turbine analysis there are three flutter mode pairs, contrary to the single flutter mode pair of the single blade analysis. Here the third FW flap-wise mode couples with the first FW torsional mode in the full turbine analysis. The same is true for the BW and symmetric modes. This is because the two FW modes are more similar to each other in motion. This can also be stated for the both BW modes and the symmetric modes.

Having analyzed how a Campbell diagram is created, it should be noted that this tool is used in Chapter 5 to see if classical flutter occurs for the ART5 reference turbine which is considered in this report. The output of the BLADEMODE V.2.0 program is organized such that the Campbell diagram can be made for a set of specific conditions. The program PHATAS however, does not use the Campbell diagram to perform a similar analysis. The output of this program provides the time history behavior of user-determined parameters. An example of such an output is provided in Figure 2.26. Here it is clear that at a time instance slightly above 100s, the torsional blade moment increases substantially within a short time span. Further analysis of the time history behavior of parameters beside the torsional blade moment is needed to determine if classical flutter is indeed occurring. Also, using output plots such as in Figure 2.26 and zooming in on the flutter region, it can be deduced if there is indeed a phase difference present between the flap-wise and torsional deformation as theoretically indicated in section 2.3. This analysis is done in Chapter 6.

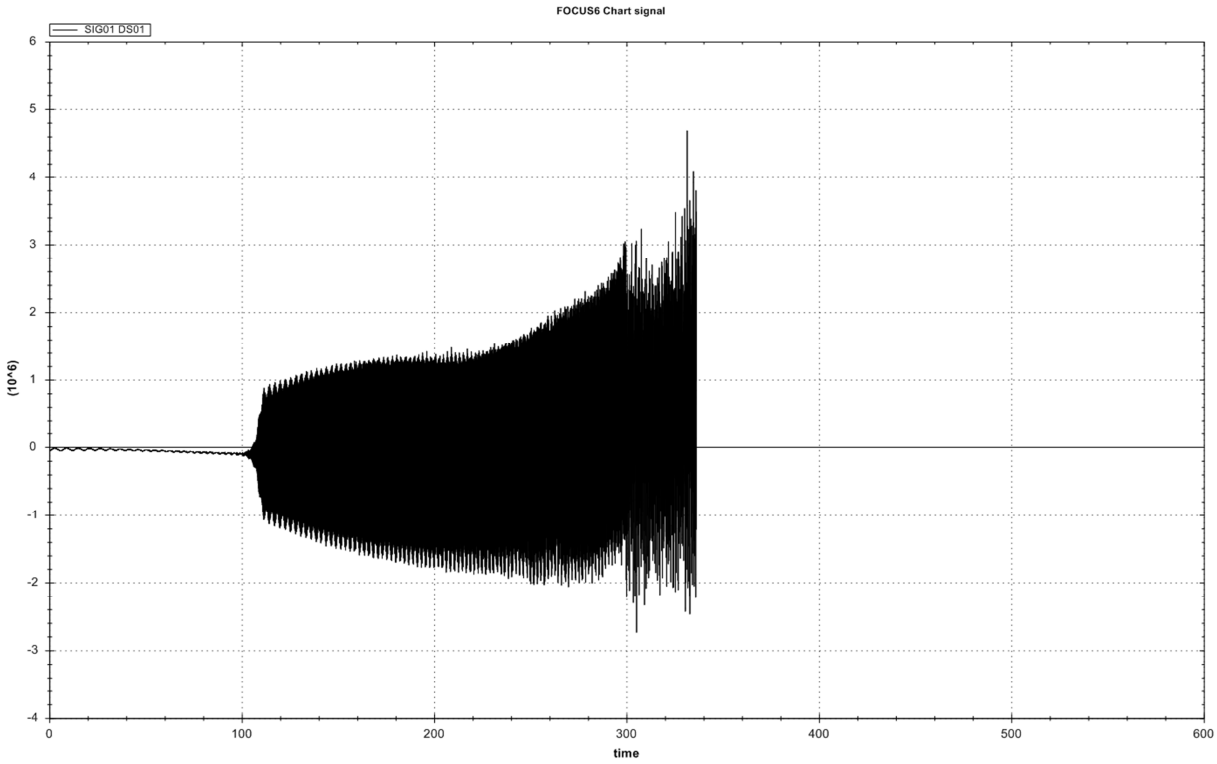

Figure 2.26: Torsional blade moment [Nm] versus time [s]. Expansion starting from 100 seconds onwards hints at an instability such as classical flutter. The plot can be used to determine if flutter occurs and what the flutter limit is.

Chapter 3 BLADEMODE V.2.0 THEORY

In this chapter the program BLADEMODE V.2.0 will be discussed [8]. The first section will give a general description of the program and how it is used in this thesis, as well as a short elaboration on the wind turbine used. The second section specifies the simulation input parameters used to yield the results necessary to perform the classical flutter analysis. The results for the simulations are presented in Chapter 5.

3.1 GENERAL DESCRIPTION BLADEMODE V.2.0

BLADEMODE V.2.0 was developed at ECN Wind Energy for the verification of eigenmodes of a single rotating rotor blade and later for the prediction of the aeroelastic stability. It is a program which performs a frequency based analysis. This makes it possible to find the natural frequencies for increasing wind or rotor speeds and consequently produce a Campbell diagram. The rotor blade used in the analysis follows engineering bending theory of beams and the structural mechanical properties of the blade are a function of the span-wise coordinate only. Furthermore, as far as bending and torsion dynamics of the blade is concerned, BLADEMODE V.2.0 includes the torsional deformation and transverse shear flexibility next to several aerodynamic and structural dynamic coupling terms. Some blade properties modeled in BLADEMODE V.2.0 are:

- Centrifugal effects (in lead-lag different than in flap direction).
- Transverse shear deformation of a cross section.
- Cross-sectional moments of inertia.
- 'Slender-beam' properties such as the distribution of sectional mass and bending stiffnesses (flat, edge and coupling).

There are also several edge constraints at the root and tip of the blade. As such the equations of motion for bending and torsion of the rotor blade are solved as a two-point boundary value problem. Examples of these constraints are the flexibility of the pitch mechanism about the blade axis and the flapping flexibility of a hinge. Since BLADEMODE V.2.0 considers small vibrations around an equilibrium state, the equations of motion are linearized and the eigenmodes and frequencies are found by solving these equations. Having discussed how the blade is modeled in BLADEMODE V.2.0 and how the program deduces the eigenmodes and associated natural frequencies, it is necessary to consider which tasks the program performs. BLADEMODE V.2.0 has three tasks which can be performed independent of each other.

1. **Quasi-steady deformed and aerodynamic state.** Both states are solved iteratively since they influence each other. A choice can be made between a BEM-based model and a vortex wake model for the rotor aerodynamics.

2. **Eigenmode solution**. It should be noted that in this algorithm there is a changing coordinate system at each section, due to the curved blade axis, which is approximated with a single 'kink'.

3. **Aerodynamic damping.** The aerodynamic damping is calculated for each of the eigenmodes. It is possible to choose between the damping from the linearized aerodynamics and the damping from integration of energy dissipation for finite-amplitude vibrations.

Now that the functional structure of BLADEMODE V.2.0 has been provided, it will be discussed how the program is used in this thesis. BLADEMODE V.2.0 is used in the shell-program FOCUS 6, but primarily as a stand-alone version. The reason for this is that the stand-alone BLADEMODE

V.2.0 program is a newer version of the program, to be precise it is the June 2012 release. The version of BLADEMODE V.2.0 incorporated in FOCUS 6 is the August 2010 version. As the newer version is not yet incorporated in FOCUS 6, it was used as a stand-alone version. Using BLADEMODE V.2.0 frequencies for each mode shape can be generated. With these frequencies a Campbell plot can be made using the rotor speed values which can be generated by BLADEMODE V.2.0 itself or provided as a user input, depending on the type of simulation performed. Which mode shapes are actually generated are determined using an output file, produced by BLADEMODE V.2.0. This file shows the overall geometry of the vibrating rotor and this can be used to draw perspective views of the mode shapes. These views are static 2D plots, while with FOCUS 6 a vibrating 3D plot can be made where it is possible to rotate around the rotor in the picture. This gives better perspective of which mode shapes are actually found. After determining the mode shapes, which are designated with the numbers 0,1,…,9, it can be seen in the Campbell plot how these modes behave as the rotor speed increases. As such it is analyzed whether it is possible to use BLADEMODE V.2.0 to determine if classical flutter occurs and thus if a flutter speed or limit can be determined. Also, if this happens to be the case, it will be considered whether a method can be established concerning how this flutter limit can be determined.

The wind turbine used for the analysis, both with BLADEMODE V.2.0 and PHATAS, is the ART5 reference wind turbine. The parameters belonging to this wind turbine are presented in Appendices C and E for BLADEMODE V.2.0 and PHATAS respectively. The ART5 reference wind turbine is based on the DOWEC 6MW wind turbine model and the 5MW RWT model of the UpWind project, with the aim to provide an aerodynamic rotor design that is more representative for well-designed modern wind turbine rotors [41]. Depending on which program is used in the analysis, the specification of the parameters required vary.

3.2 Input Files for Simulations

Three simulations are performed using BLADEMODE V.2.0, simulation 1, simulation 2 and simulation 3 respectively. All simulations are performed using a BEM-based model for the rotor aerodynamics. This is provided in the ART5 input file in Appendix C. Furthermore, the BEM-based model is remarkably faster than using the vortex wake mode, which is the other option. Each of the three simulations are discussed in this section. In the subsequent sections BLADEMODE V.2.0 and PHATAS parameters will be given in italic.

The reason for having three simulations can be explained by first considering the *generator curve table*, see Table C.1. This table contains the *slow shaft generator torque*, *the loss of torque* and the *pitch angle* for a range of *rotor speeds*. For non-zero values of the *slow shaft generator torque*, there is generator damping. This can be depicted in a figure.

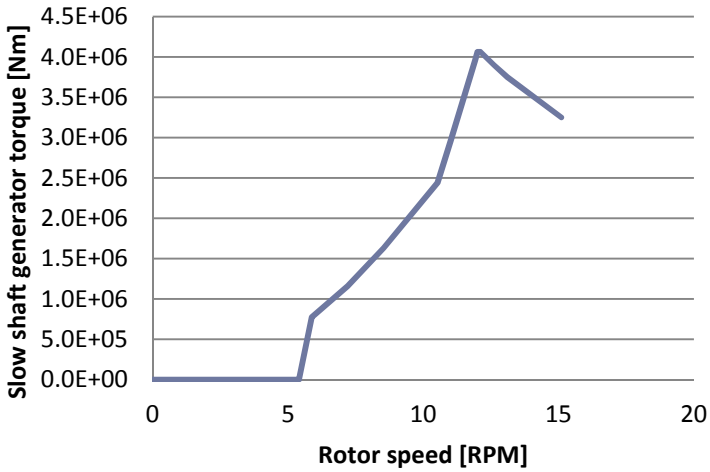

Figure 3.1: Generator curve for the original *generator curve table*.

The slope of the *generator curve table* in Figure 3.1 adds damping when the slope is positive and a decreasing slope has an opposite effect [42]. Based on this knowledge, a distinction is made to perform two simulations. The first simulation will include this generator damping effect on the modal frequencies in the classical flutter analysis, while the second simulation will not. Therefore, the second simulation will have zero entries in Table C.1 for all *slow shaft generator torque* and the *loss of torque* entries. The first simulation has the parameter *solve speed* set ON. The relevance of this statement is made clear in the next section.

For the second simulation a division is made when considering the BLADEMODE V.2.0 parameter *solve speed*. When this parameter is set ON, combined with the *aerodynamics* being set ON, the *rotational speed* is solved from the aerodynamic torque, the generator torque-speed relation and the corresponding *pitch angle* specified in the *generator curve table*. When *aerodynamics* is set ON, the quasi-steady aerodynamic loads are solved, the aerodynamic stiffness is included in the eigenmode solution, and the aerodynamic damping is calculated. For *solve speed* ON the value of *rotational speed* is the initial speed in searching the steady-state solution for each wind speed specified in *wind* series, which contains a range of non-zero increasing wind speeds. By setting *solve speed* OFF, but keeping *aerodynamics* ON, the *generator curve table* is no longer considered. The rotor speed is not calculated with these settings and it needs to be indicated manually. The range of *rotor speeds* is provided in the *wind series*, which has three columns when *solve speed* is set OFF. The first column contains the *wind speed* values, the second column contains the *rotor speed* value, while the last column specifies the *pitch angle*. When *solve speed* is OFF, the value for the *wind speed* is constant for each entry in the *wind series* parameter. As such, for a specific constant wind speed the *rotor speed* varies and the frequencies are calculated for each of these rotor speeds. By performing a simulation with *solve speed* OFF, the effect on the calculated frequencies and thus potential classical flutter is captured, due to not letting BLADEMODE V.2.0 converge around a steady-state solution for the rotor speed and not interpolating the *generator curve table* for this rotor speed. This in contrast to when *solve speed* is ON.

Performing a simulation with inclusion of the *slow shaft generator torque* and *the loss of torque*, as well as setting *solve speed* OFF is unnecessary. This is due to the fact that for *solve speed* OFF the *generator curve table* is not consulted. Hence this simulation would be similar to the case of no *shaft generator torque* and *the loss of torque*, with *solve speed* OFF.

Having provided the reasoning behind performing these three simulations, the main differences between the three simulations are presented in Table 3.1 for clarity.

Table 3.1: Main differences between the three simulation.

Simulation 1	***Simulation 2***	***Simulation 3***
Solve speed ON, include *slow shaft generator torque*, *the loss of torque.*	*Solve speed* ON, no *slow shaft generator torque*, *the loss of torque.*	*Solve speed* OFF, no *slow shaft generator torque*, *the loss of torque.*

Another important aspect of the three simulations is the setting for the static blade *pitch angle*, which is set equal to $\theta_s = 8^o$ for all the simulations. This value is entered in either the *generator curve table* or *wind series*, depending on the simulation performed, for each entry where the *pitch angle* needs to be specified. The value of eight degrees is similar to the value of the *pitch angle* used in the overspeed loadcase for the PHATAS analysis. This is elaborated on in Chapter 4. As such, not only a comparison between the BLADEMODE V.2.0 simulations is possible, but also a comparison between the results for the classical flutter analysis of BLADEMODE V.2.0 and PHATAS.

3.2.1 PARAMETERS FOR SIMULATION 1

The main settings defining the first simulation have been specified. But apart from the main simulation settings, there are other parameters which need to be specified correctly in order to be able to perform the simulation. Taking as a starting point the ART5 input file specified in Appendix C, the input data is altered accordingly. The parameters which are altered are shown in Table 3.2.

Table 3.2: Changed parameters with respect to ART5 input file.

Changed parameter	***Value***	***Unit***
Aerodynamics	ON	-
Blade torsion	ON	-
Deformed state	ON	-
Nr. of modes	9	-
Solve speed	ON	-
Wind series	1-60	[m/s]

As far as the apparent mass is concerned, its inclusion in the eigenmode solution is independent of whether *aerodynamics* is set ON or OFF. Setting *blade torsion* ON results in the torsional deformation being included for the deformed equilibrium state and the eigenmodes. The *deformed equilibrium state* is solved iteratively together with the 'frozen wake state' when the value is set ON. The *number of eigenmodes* setting indicates the number of eigenmodes that are to be solved. Higher order modes, of which the shape has several nodes, may be solved with some numerical error. This is elaborated on in Chapter 5. Also, the value for the maximum wind speed is chosen arbitrarily but such that it should capture the classical flutter phenomenon were it to occur. Therefore a large value is chosen, which might not be realistic for operating conditions.

The order in which these parameters are altered is irrelevant. One can change the parameters in the sequence preferred, as long as the simulation is not yet run before all the required parameters are changed. The full BLADEMODE V.2.0 input file used for simulation 1 is provided in Appendix D.

3.2.2 PARAMETERS FOR SIMULATION 2

Following a similar logic as explained in section 3.2.1, the ART5 input file from Appendix C is altered with the same parameters stated in Table 3.2. The only difference with simulation 1 is the zero values for the *slow shaft generator torque* and *the loss of torque* in the *generator curve table*, as explained earlier.

3.2.3 PARAMETERS FOR SIMULATION 3

For the third simulation, four parameters differ from the first simulation settings. These parameters are presented in Table 3.3.

Table 3.3: Changed parameters with respect to ART5 input-file and first simulation.

Changed parameter	***Value***	***Unit***
Wind series (wind speed)	3; 8; 15; 60	[m/s]
Wind series (rotor speed)	0-48 (48 steps)	-
Wind series (pitch angle)	8	[deg]
Solve speed	OFF	-

The *wind speed* in the *wind series* parameter contains four different values. The simulation is performed for each one of these *wind speeds*. The values are chosen such that an analysis can be made for realistic operating conditions and for an extreme case. Although four simulations are performed, there is only the single difference of the wind speed value. Hence all four simulations are mentioned in this section as 'the third simulation'. In the remainder of the report it will always be indicated which wind speed was used if the third simulation is mentioned.

The maximum value for the *rotor speed* is based on the results obtained for the first simulation, which will be presented in Chapter 5. The maximum *rotor speed* value calculated for the first simulation will prove to be around 48 RPM.

Chapter 4 PHATAS THEORY

In this chapter the program PHATAS will be discussed [43]. The first section will give a general description of the program and how it is used in this thesis, as well as a short elaboration on the wind turbine used. The second section specifies the simulation input parameters used to yield the results necessary to perform the classical flutter analysis. The results for the simulations are presented in Chapter 6.

4.1 GENERAL DESCRIPTION PHATAS

The abbreviation PHATAS stands for Program for Horizontal Axis wind Turbine Analysis and Simulation. This program is used to analyze the dynamics and loads of a horizontal axis wind turbine. To this extent, PHATAS is incorporated in the user-friendly shell program FOCUS 6, which is a rotor blade design tool. Using PHATAS the time history behavior of the wind turbine dynamics can be analyzed, which can be post-processed to obtain the results in the frequency domain. The main difference with BLADEMODE V.2.0 is that PHATAS is a non-linear time domain simulation, while BLADEMODE V.2.0 performs a frequency based analysis. Another difference is that BLADEMODE V.2.0 is based on a single blade analysis, while PHATAS analyses the dynamic behavior and the corresponding loads in the main components of a wind turbine such as the rotor blades, the rotor shaft and the tower. Based on the non-linear beam approach, most of the bending and torsion flexibilities of the blades and the tower are described in the structural model of the wind turbine in PHATAS [44]. Furthermore, variables for the generator torque-speed characteristics, for the torsional deformation of the rotor shaft and gearbox support, for teetering and for passive blade pitch motion are included in the model of the drive train and rotor hub. As far as the aerodynamics is concerned, PHATAS has a BEM based aerodynamic model. This model contains the terms for instationary response of the rotor wake. Furthermore, there are two ways to calculate the blade loads. One is with the heuristic dynamic stall model of Snel (which will be used), while the other is based on stationary airfoil coefficients [45]. As far as control is concerned in PHATAS, a P-D algorithm for control of the generator power or of the rotor speed by means of pitch actions is included. Also, if desired by the user it is possible to use a user-reserved routine to link dedicated control algorithms to the code. Some other models used in PHATAS are listed below [46].

- Linearized support structure model, using the Craig-Bampton model reduction.
- Drive train model consisting of gear ratio, shaft torsion and flexible mounting.
- Full 3D turbulent wind field model.

Having described the basic principles of simulations performed with PHATAS, as well as highlighting the structure of the PHATAS code, it is worth noting that the source code of PHATAS can be considered to have three origins.

- The tool GENMENU is used to generate the main program and input structure. The latter not only contains the name of the default input file, but also the files with the input properties and the routines for reading the input files.
- The part for the calculations on the wind turbine dynamics.
- A part which can be replaced on a modular basis as it is developed separate from the PHATAS code. This part solves the mode shapes and natural frequencies of the tower, as well as calculating the dynamic response.

Now that the general description of PHATAS is provided, the emphasis is put on how it is used in this thesis. The program PHATAS is used in this thesis inside the shell program FOCUS 6. Similar to what has been done with BLADEMODE V.2.0, simulations are performed to see if classical flutter occurs and thus a flutter speed or limit can be determined. Based on whether this is the

case or not, a method will be established on how to determine this flutter speed. With PHATAS the time history behavior of parameters deemed relevant for classical flutter are calculated. Considering the behavior of these parameters in time, it can be deduced if classical flutter occurs and a flutter speed can be established. An example of such a time history behavior was provided in Figure 2.26. The potential classical flutter phenomena may be detected in the time history behavior of the relevant parameters, if the correct settings are applied in PHATAS. To aid the user in this analysis, the shell program FOCUS 6 has a built-in pre-processor LCPREP. With this pre-processor an overspeed loadcase is generated. Using this loadcase, the desired output parameters are determined based on an increasing wind and rotor speed. This loadcase is adjusted only in one way, by setting the *pitch angle* equal to eight degrees for all three blades as was the case for the BLADEMODE V.2.0 analysis. The analysis is performed using the ART5 reference turbine, similar to the analysis with BLADEMODE V.2.0. However, as PHATAS is a full turbine analysis program, the input parameters differ from those required for BLADEMODE V.2.0. Consequently, the ART5 reference wind turbine input parameters are provided in Appendix E.

4.2 Input Files for Simulation

Taking the ART5 input file as a starting point, generating the overspeed loadcase and incorporating the changes to this loadcase, only the parameter *output table* needs to be altered. The required *output table* is provided in Table 4.1.

Table 4.1: Adjusted output table used for the overspeed analysis in PHATAS.

Output parameter	***Description***	***Units***
2	Wind speed at the hub	[m/s]
12	Rotor speed	[RPM]
21	Bending moment in the tower about X_F	[Nm]
22	Bending moment in the tower about Y_F	[Nm]
112	Aerodynamic angle of attack between the relative wind and blade chord	[°]
116	Value of the lift coefficient c_l	[-]
147	Flap displacement of the blade 1	[m]
148	Torsional blade deformation 1	[°]
247	Flap displacement of the blade 2	[m]
248	Torsional blade deformation 2	[°]
347	Flap displacement of the blade 3	[m]
348	Torsional blade deformation 3	[°]

In this table output parameters 21 and 22 are related to the reference frame for tower loads indicated in Figure 4.1. In this same figure, also the deformed rotor plane reference system for blade loads is depicted. The description of the symbols is provided in the illustration.

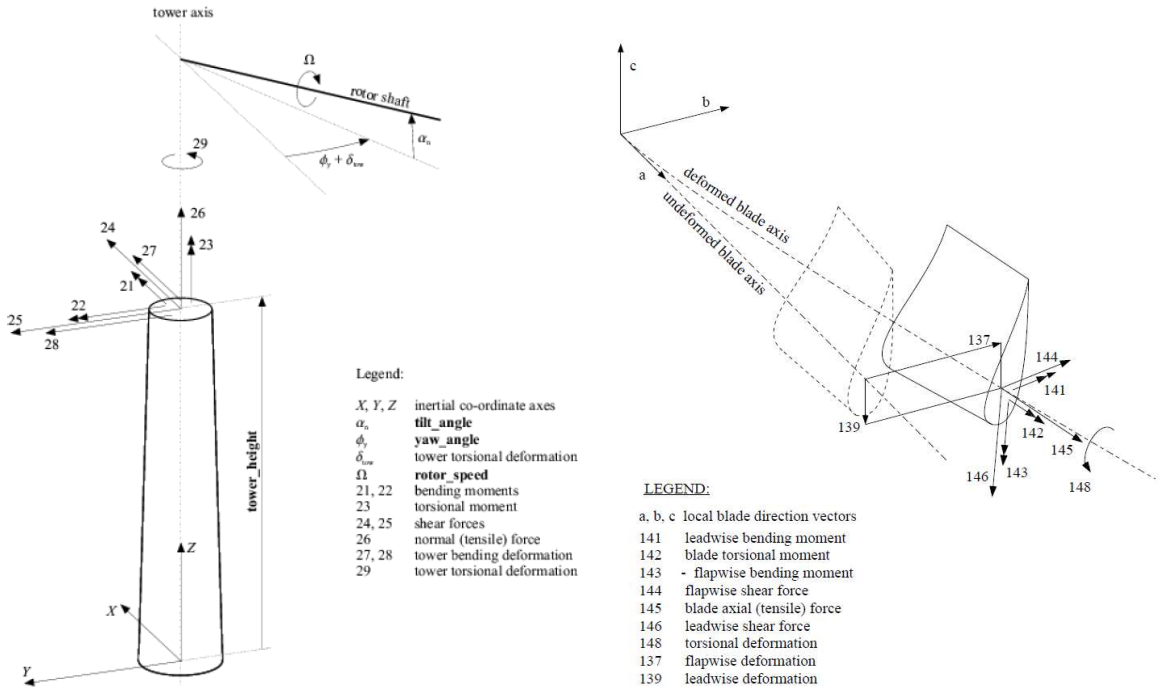

Figure 4.1: Left picture shows the reference frame for the tower, while the right picture shows the deformed rotor plane reference system [43].

Consulting Figure 4.1, it should be noted that output parameter number 147 is not present in the illustration. The reason for this is simply because it is the same as indicated for number 137, only now with respect to the deformed blade axis.

Output parameters 21 and 22 are considered as they are related to the tower side-to-side and fore-aft modes, respectively. The tower bending moments are determined at the bottom of the tower, where they are largest. Next to this, the time history behavior of the parameters related to the flap-wise and torsional modes will indicate whether classical flutter occurs or not. Also, these parameters are determined at the tip location, where their deformations are largest. Consequently output parameters 112 and 116 are also determined at the tip. These two parameters are used in the analysis to check whether the classical flutter phenomena has occurred.

The output parameters mentioned in Table 4.1 are produced for both *pitch angles* of eight and ten degrees. Simulating for both cases makes a comparison possible to see the effect of the pitch angle on the possible occurrence of flutter. This simulation is done to substantiate what it implied in the second main flutter criterion in section 2.5. Based on this criterion it is expected that increasing the *pitch angle* will reduce W_0 and hence delay the occurrence of classical flutter. Furthermore, the effect on classical flutter due to changing the *torsion stiffness* values in the torsion data table, see Table C.5, is considered. By doing this, the effect of the third main flutter criterion stated in section 2.5 is substantiated. After simulating both effects on the flutter limit, it is considered which parameter could best be changed to alter the flutter limit.

Chapter 5 BLADEMODE V.2.0 ANALYSIS

In this section the results obtained with BLADEMODE V.2.0 are presented. The aim of this chapter is to provide an answer to whether it is possible to use BLADEMODE V.2.0 to determine an efficient method for finding the flutter speed at which classical flutter occurs. The manner in which the analysis is conducted is outlined in Chapter 3, as well as the input data for the simulations. To this extent the sections one, two and three deal with the results of the first, second and third simulation respectively. The fourth section provides the general conclusions with regard to determining the classical flutter limit using BLADEMODE V.2.0, based on the simulations outlined in Chapter 3. Finally the fifth section discusses some of the limitations of the program.

5.1 SIMULATION 1 RESULTS

This section deals with results of the first simulation. First the mode shapes found will be provided. After this the Campbell plot will be presented and analyzed. The mode shapes found for the first simulation are described in Table 5.1. These mode numbers will be used in all the Campbell plots.

Table 5.1: Mode shapes for the first simulation. *Solve speed* ON, *wind series*: 1-60 [m/s], including *slow shaft generator torque* and *loss of torque.*

Mode number	***Mode shape***
Mode 0 (M0)	Unknown (should be 1P gravity load)
Mode 1 (M1)	Tower fore-aft
Mode 2 (M2)	1st flap-wise
Mode 3 (M3)	1st collective edge-wise
Mode 4 (M4)	2nd flap-wise
Mode 5 (M5)	2nd collective edge-wise
Mode 6 (M6)	3rd flap-wise
Mode 7 (M7)	3rd collective edge-wise
Mode 8 (M8)	4th flap-wise
Mode 9 (M9)	1st torsion

These mode shapes are determined by considering the static 2D plots presented in Appendix F, to be precise Figures F.1 and F.2. Using FOCUS 6 and viewing the mode shape plots with this shell-program, a better perspective is obtained which allows for easier recognition of the mode shapes. These mode shapes and their associated plots are determined by considering what the dominant mode shape is for the entire *wind speed* or *rotor speed* range. In case of simulation 1 the rotor speeds are solved by BLADEMODE V.2.0 for a *wind speed* range of 1-60 m/s. By dividing this range of *wind speeds* into smaller sections of 5 m/s and each time considering the mode shape plots for this section, the dominant mode shapes for the full *wind speed* range can be determined. In case of simulation 3, the *solve speed* is OFF. Hence, as explained in Chapter 3, the *wind speed* is kept constant while the *rotor speed* is given a range of values. For each of these *rotor speed* values the mode shapes can be depicted in a mode shape plot. Therefore the dominant mode shapes can be found by considering the mode shape plots for all the *rotor speeds*. Nevertheless, for simulation 1 the first mode shape could not be determined as it remained unclear in the plots. It is known however, that it should represent the 1P gravity load [8].

Furthermore, in Table 5.1 a reference is made to the collective edge-wise mode shape. This is because the *variable speed* is set on in the ART5 input file, there are only collective edge-wise modes determined. The Campbell plot determined for the first simulation is presented in Figure 5.1.

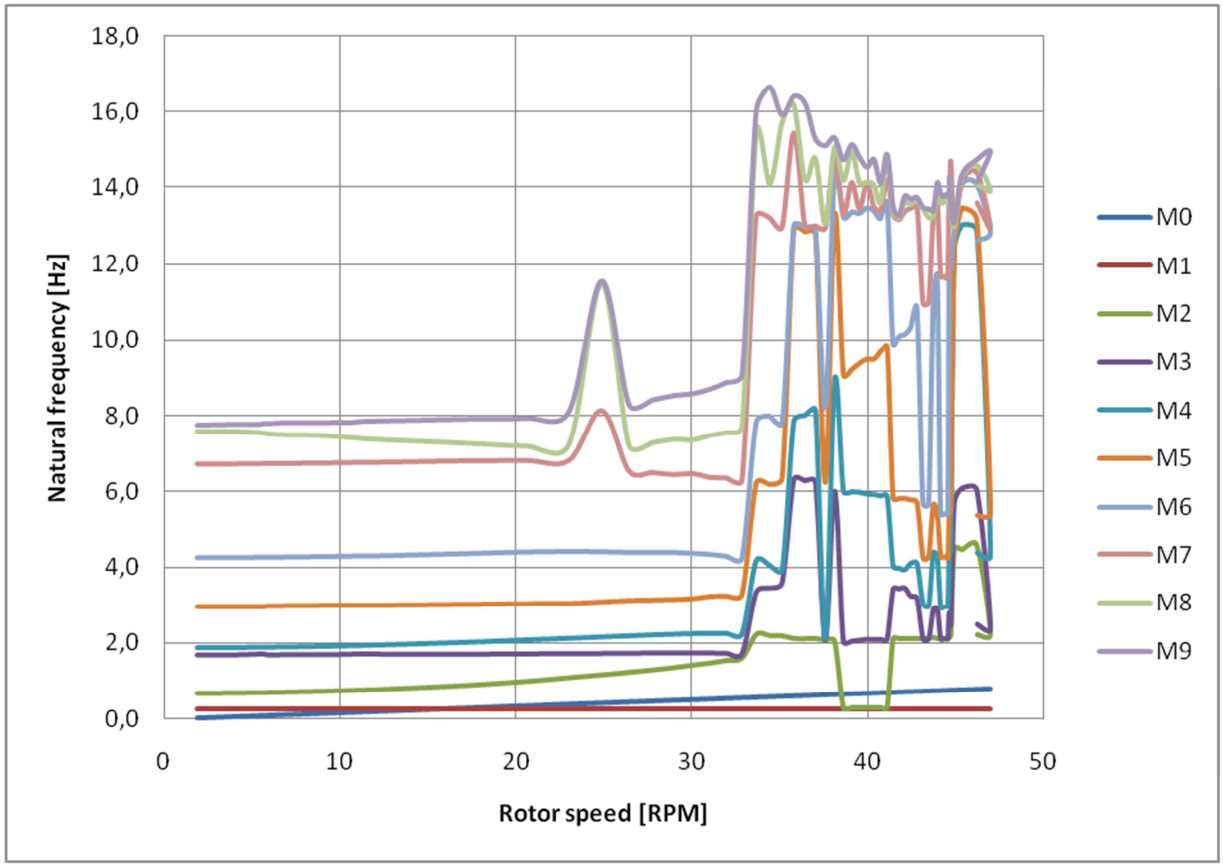

Figure 5.1: Unadjusted Campbell plot for simulation 1. *Solve speed* ON, *wind series*: 1-60 [m/s], including *slow shaft generator torque* and *loss of torque.*

When simulating for a range of wind velocities from 1-60 m/s, there will be gaps in the frequency tables of the modes. This is because frequencies need to be sorted out for all the modes. When searching for the natural frequencies, the program sometimes mistakenly assigns the solution for mode 5 to mode 4 for example. The reason for this is that a solution is sought for the case where the characteristic equation equals zero. Sometimes a solution is missed or not found and the next solution is assigned to the location where the absent solutions should have been. This causes a shift in the assigning of the frequencies to a specific mode. It must be noted that the values of the frequencies themselves do not alter, there is only a mismatch occurring between the mode and its natural frequency. Furthermore sometimes when this phenomenon occurs, not only is a natural frequency assigned to the incorrect mode (the shift) but also this same frequency is still assigned to its associated mode. This causes the same frequency to appear twice and thus overlapping of frequencies in the Campbell plot is present. This can be seen in Figure 5.1. Careful sorting out of the frequencies improves clarity of the graph, which results in Figure 5.2.

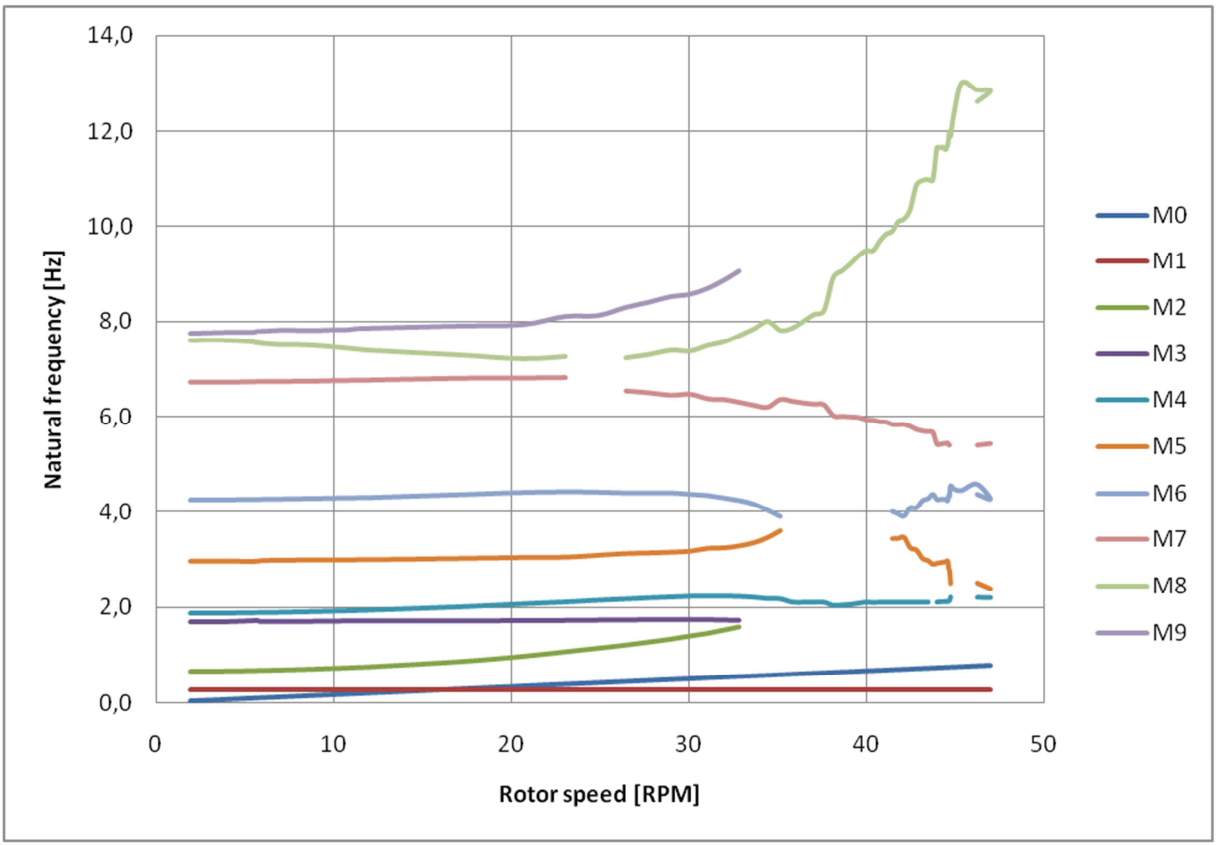

Figure 5.2: Adjusted Campbell plot for simulation 1. *Solve speed* ON, *wind series*: 1-60 [m/s], including *slow shaft generator torque* and *loss of torque.*

Consulting Figure 5.2, no clear relation seems to exist between any flap-wise and torsional mode, contrary to what would be expected if classical flutter were to occur. There is no approaching of any flap-wise and torsional mode visible in the figure. Furthermore the torsional mode has increasing frequencies for increasing rotor speed values. This is the opposite of what would be expected based on Chapter 2.

5.2 SIMULATION 2 RESULTS

This section deals with results of the second simulation. First the mode shapes found will be provided. After this the Campbell plot will be presented and analyzed. It will be determined what the effect is on occurrence of classical flutter, by setting the *slow shaft generator torque* and *the loss of torque* equal to zero in the *generator curve table.* This can be done by comparing the results of simulation 2 with those from simulation 1.

The mode shapes found for the second simulation are the same as found for simulation 1, which are shown in Table 5.1. Therefore it is deemed unnecessary to provide the 2D mode shape plots for simulation 2. The manner in which the mode shapes are determined was explained in the previous section. The Campbell plot determined for simulation 2 is provided in Figure 5.3.

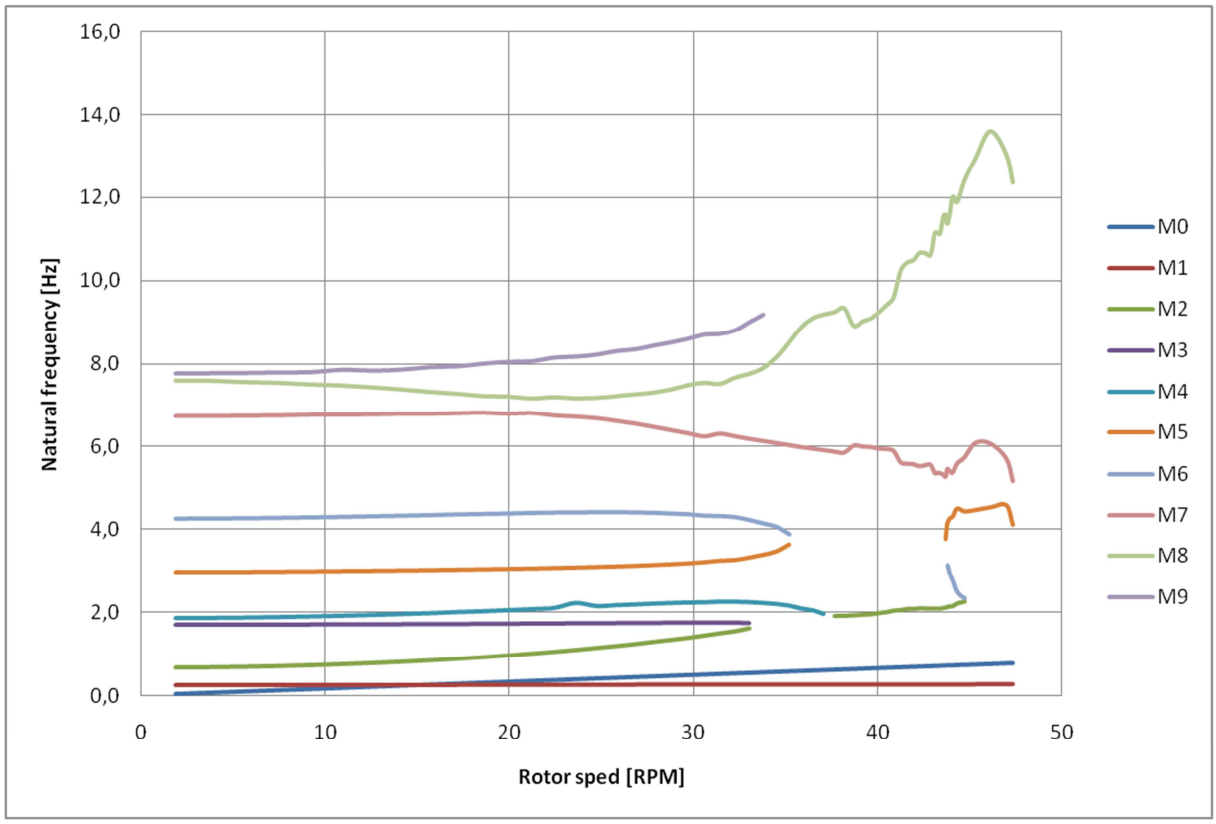

Figure 5.3: Adjusted Campbell plot for simulation 2. *Solve speed* ON, *wind series*: 1-60 [m/s], excluding *slow shaft generator torque* and *loss of torque.*

From this figure a similar conclusion to the one for the first simulation can be drawn. The flap-wise modes and torsional mode do not approach each other. This is again in contrast to what would be expected. Furthermore, as classical flutter is not deemed to occur, the effect of the *slow shaft generator torque* and *the loss of torque* on classical flutter cannot be determined. However it is possible to consider the effect on the frequencies. This done by considering the torsional mode (M9) and plotting the frequencies in one figure, which is shown in Figure 5.4

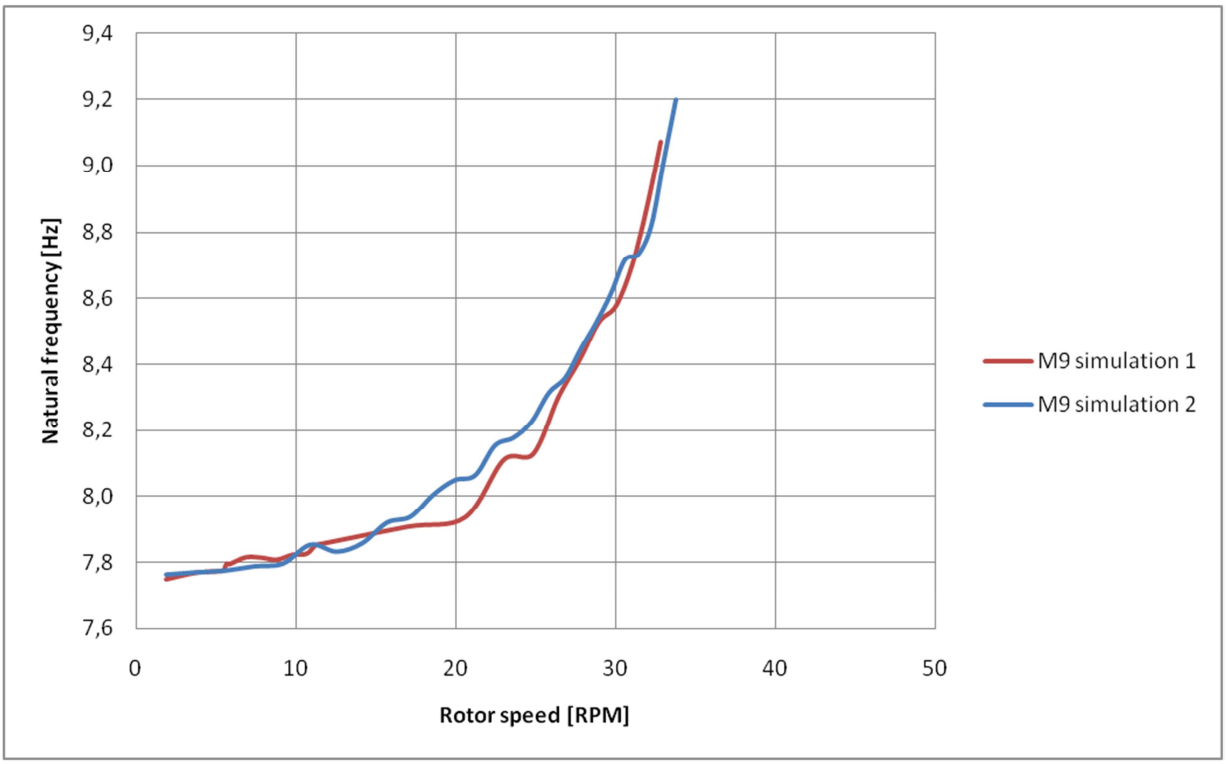

Figure 5.4: Comparison between frequencies from simulation 1 (red) and simulation 2 (blue) for the torsional mode.

From this figure it can be deduced that the frequencies for the torsional mode of simulation 2 correspond good with those of simulation 1. It is however visible that setting the *slow shaft generator torque* and *the loss of torque* equal to zero in the *generator curve table*, does create a difference between the results of the two simulations. To be more precise, in simulation 1 the generator damping is included which results in slightly lower frequencies for the torsional mode compared to the second simulation. As a result of this it is visible in Figure 5.4 that the red line clearly lies below the blue line for some distinct part of the plot. From this result it can be deduced that if classical flutter could be detected with either simulation 1 or 2, the effect of setting the *slow shaft generator torque* and *the loss of torque* equal to zero should be considered.

5.3 SIMULATION 3 RESULTS

This section provides the results for all the four wind speed values of the third simulation. The reasoning for choosing these values was given in Chapter 3. Similar to the structure used in the previous two sections, the results for the third simulation are presented in this section. It will be considered what the effect is on the calculated frequencies and potential classical flutter, due to not letting BLADEMODE V.2.0 converge around a steady-state solution for the rotor speed and not interpolating the *generator curve table* for this rotor speed. This in contrast to the first two simulations.

The mode shapes found for each of the *wind speed* values of simulation 3 are found to be the same as those for the previous two simulations, with the exception that M0 can now be determined in this simulation based on the 2D plot. Therefore the mode shapes for the third simulation are provided in Appendix F, to be precise Figures F.3 and F.4. The first mode shape (M0) is determined to be indeed the 1P gravity load, which one would expect as stated earlier. Also, the mode shape plots are provided for the *wind speed* value of 3 m/s as the other *wind speeds* yield the same result.

The Campbell plots for each of the four simulations is provided in Figure 5.5-Figure 5.8

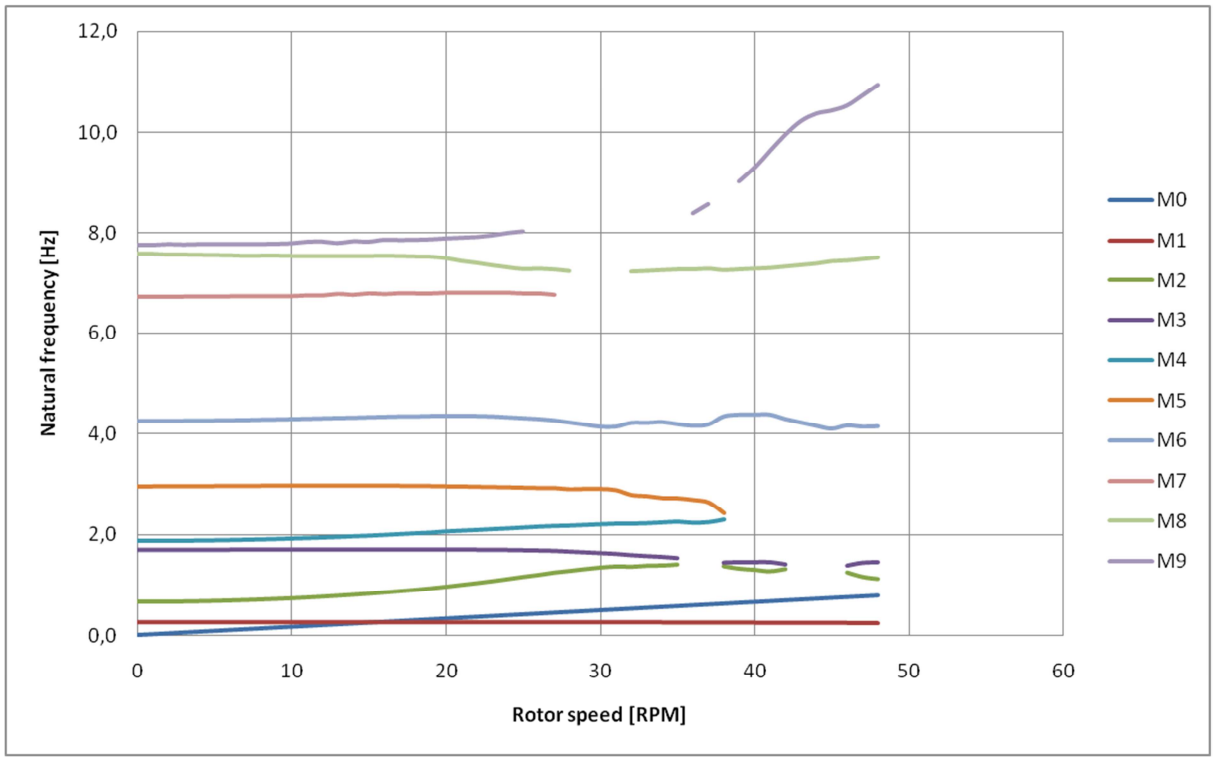

Figure 5.5: Adjusted Campbell plot for simulation 3 with wind speed 3 m/s. *Solve speed* OFF, excluding *slow shaft generator torque* and *loss of torque.*

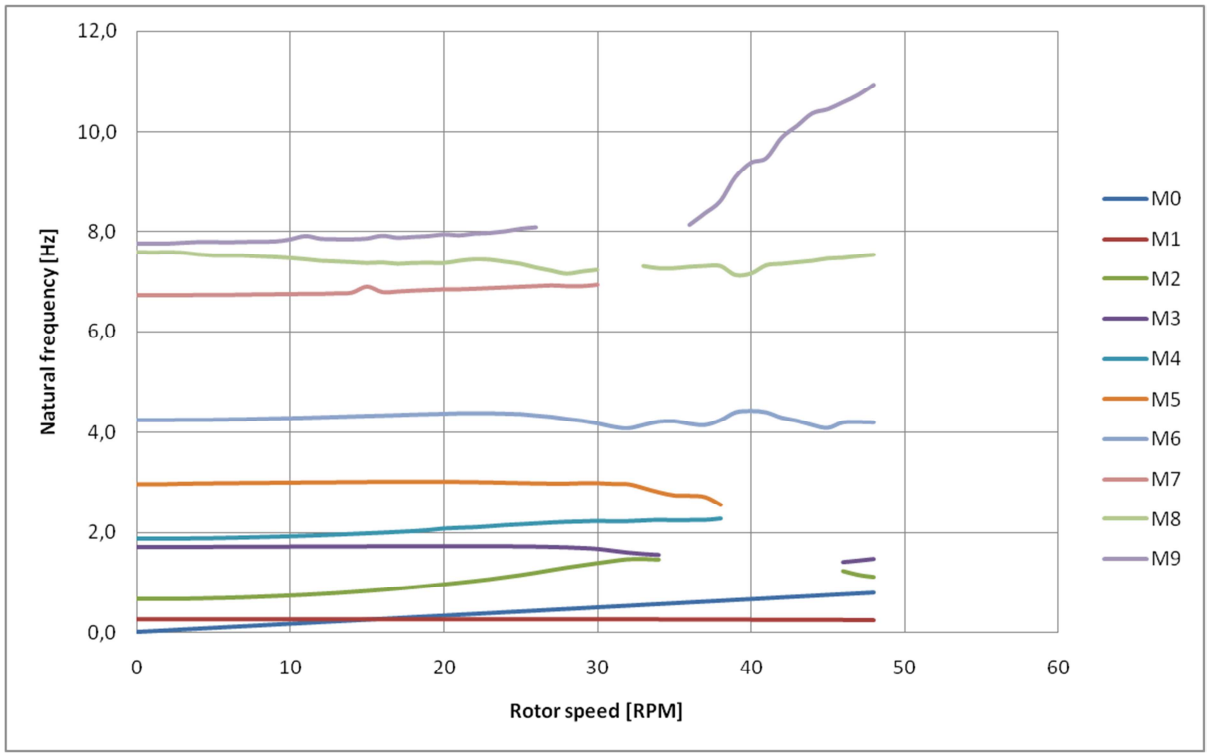

Figure 5.6: Adjusted Campbell plot for simulation 3 with wind speed 8 m/s. *Solve speed* OFF, excluding *slow shaft generator torque* and *loss of torque.*

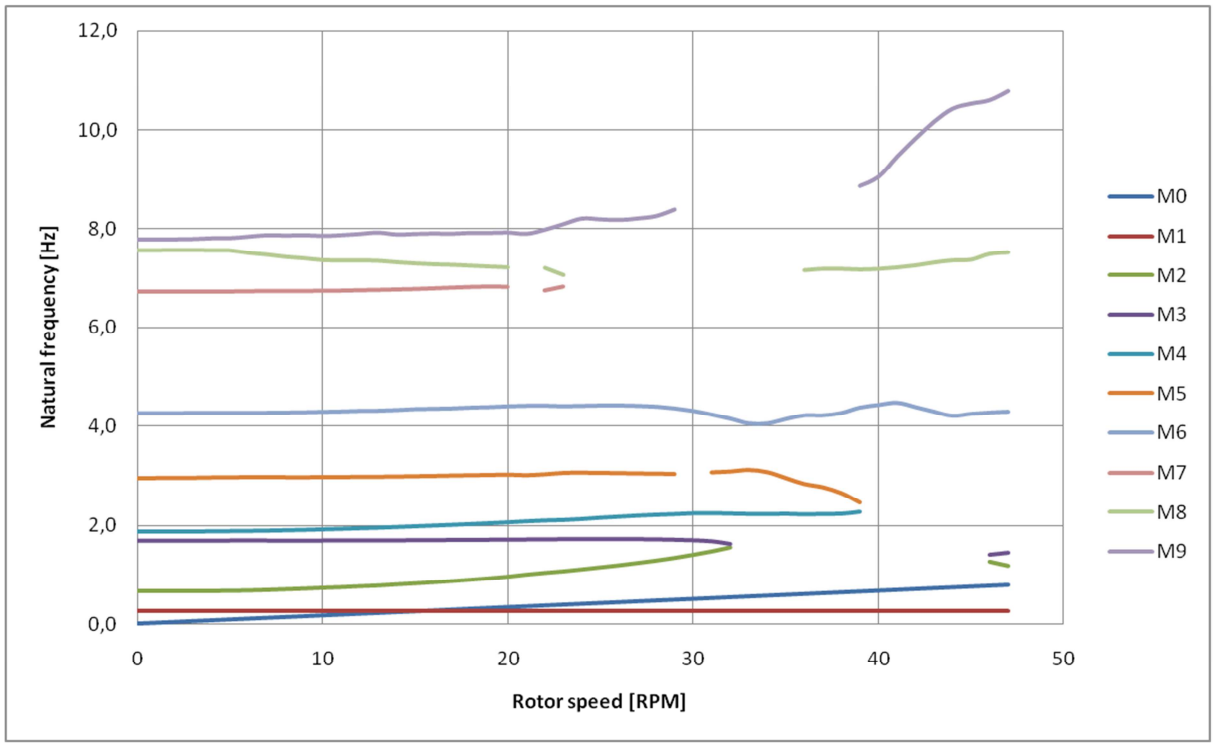

Figure 5.7: Adjusted Campbell plot for simulation 3 with wind speed 15 m/s. *Solve speed* OFF, excluding *slow shaft generator torque* and *loss of torque.*

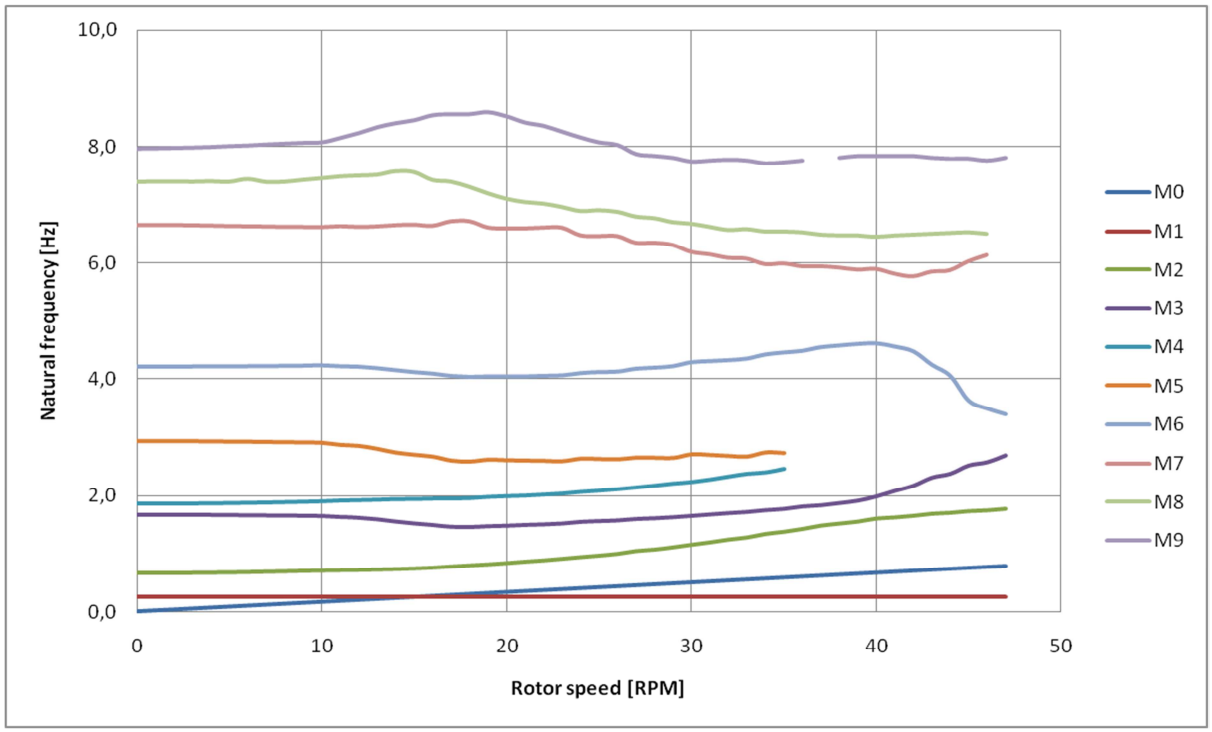

Figure 5.8: Adjusted Campbell plot for simulation 3 with wind speed 60 m/s. *Solve speed* OFF, excluding *slow shaft generator torque* and *loss of torque.*

From these figures it is evident that there is again no approaching or intersection visible of any of the flap-wise modes and torsional mode. Therefore it is deemed that classical flutter cannot be predicted for this simulation. It should be noted however that for an increasing value of the *wind speed* in this simulation, the torsional mode does appear to no longer keep increasing with the rotor speed. Even more, in Figure 5.8 it can be seen that it even decreases from around 20 RPM onwards. Nevertheless, there is no approaching of a flap-wise or torsional mode visible.

Comparing the four figures of simulation 3 with each other, the behavior of the mode shapes with increasing rotor speeds is similar. The only exception to this is Figure 5.8, where the best results for high rotor speed values are obtained. The number of gaps is relatively low for this simulation. Furthermore, comparing the Campbell plots from the three simulations with those from the first two simulations is irrelevant as classical flutter is not detected.

5.4 General Conclusions

From the figures of all three simulations it is evident that there is no approaching or intersection visible of any of the flap-wise modes and the torsional mode. Therefore there is no indication for the occurrence of classical flutter, regardless of the simulation considered. As such it not possible to determine the flutter speed and derive a method to find this limit using BLADEMODE V.2.0. A possible explanation could be that classical flutter cannot be predicted with BLADEMODE V.2.0, since it is an instability where the flap-wise and torsional vibration would not be in phase. Considering that the solutions provided with BLADEMODE V.2.0 are only for vibrations which are in phase [C.Lindenburg, ECN], classical flutter cannot be detected then. However, it would still be expected that the frequencies of the flap-wise and torsional mode would approach each other as the rotor speed increases. This is however not the case.

Also as classical flutter cannot be detected, the influence of a changing *pitch angle* and/or changing *torsional stiffness* on the flutter speed, is not determined.

5.5 Limitations of the Program

One of the main limitations of the program is that the incorrectly assigned frequencies to the mode shapes need manual adjusting, such that the frequencies are assigned to the correct mode shapes. This is not only time-consuming but also error prone and may thus lead to incorrect conclusions being drawn based on the Campbell plot.

Another limitation of the program is that no single output file is generated with the data necessary to create a Campbell plot. As such, the required data needs to be transferred manually into one file before the Campbell plot can be made with an external program. This seems inefficient and error prone.

Also, when the analysis is performed using BLADEMODE V.2.0, a 2D plot can be made of the mode shapes. These are sometimes difficult to interpret as the perspective is not quite clear.

Finally, to determine the dominant mode shapes, numerous extra simulations must be performed in order to find the dominant modes. Even though the simulations for the full range of either the *wind speeds* or *rotor speeds* are already performed, this is insufficient to determine the dominant mode shapes. This is again deemed inefficient.

Chapter 6 PHATAS ANALYSIS

In this section the results obtained with PHATAS are presented. The aim of this chapter is to provide an answer to whether it is possible to use PHATAS to determine an efficient method for finding the flutter speed at which classical flutter occurs. The manner in which the analysis is conducted is outlined in Chapter 4. Also, as BLADEMODE V.2.0 is unable to detect classical flutter, the comparison with the results from PHATAS is omitted as this is not possible.

The first section of this chapter provides the results for the simulation done for a *pitch angle* of eight degrees. Following this, the second section presents the method of how to determine the classical flutter limit based on the results presented in section 6.1. The third section contains the results for the influence of a changing *pitch angle* or *torsional stiffness* on the classical flutter limit. Consequently, section four contains the results of the analysis on how to generate the natural frequency at which classical flutter occurs. Section five contains the general conclusions with regard to determining the classical flutter limit using PHATAS. Finally the sixth section discusses some of the limitations of the program.

6.1 SIMULATION RESULTS PITCH ANGLE 8 DEGREES

This section presents the results obtained with the PHATAS program using the shell-program FOCUS 6, which are relevant in the classical flutter analysis and/or indicate the presence of an instability at a given moment in time during the simulation. Figure 6.1 shows the increasing wind speed used in the LCPREP analysis, followed by the rotor speed in Figure 6.2. The bending moment in the tower about the X^F- and Y^F-axis is provided in Figure 6.3 and Figure 6.4 respectively, while the flap-wise displacements of each individual blade are shown in Figure 6.5-Figure 6.7. The torsional blade deformations of each individual blade are shown in Figure 6.8-Figure 6.10.

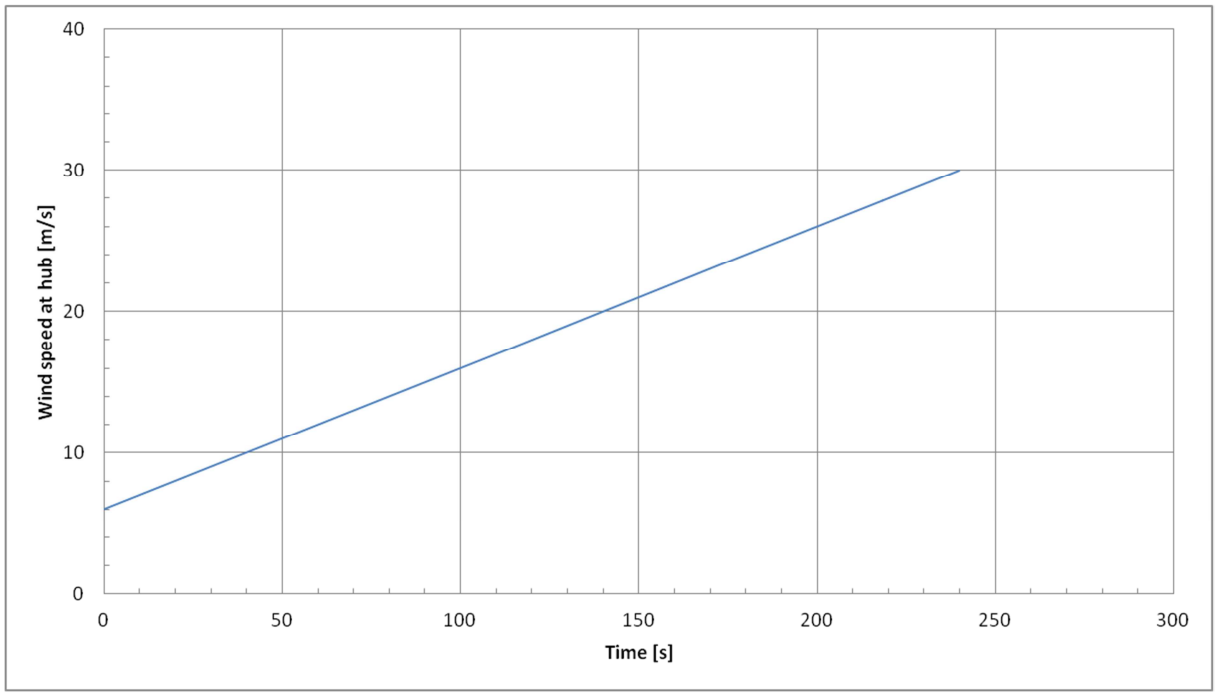

Figure 6.1: Increasing wind speed used in the LCPREP overspeed loadcase to analyze classical flutter.

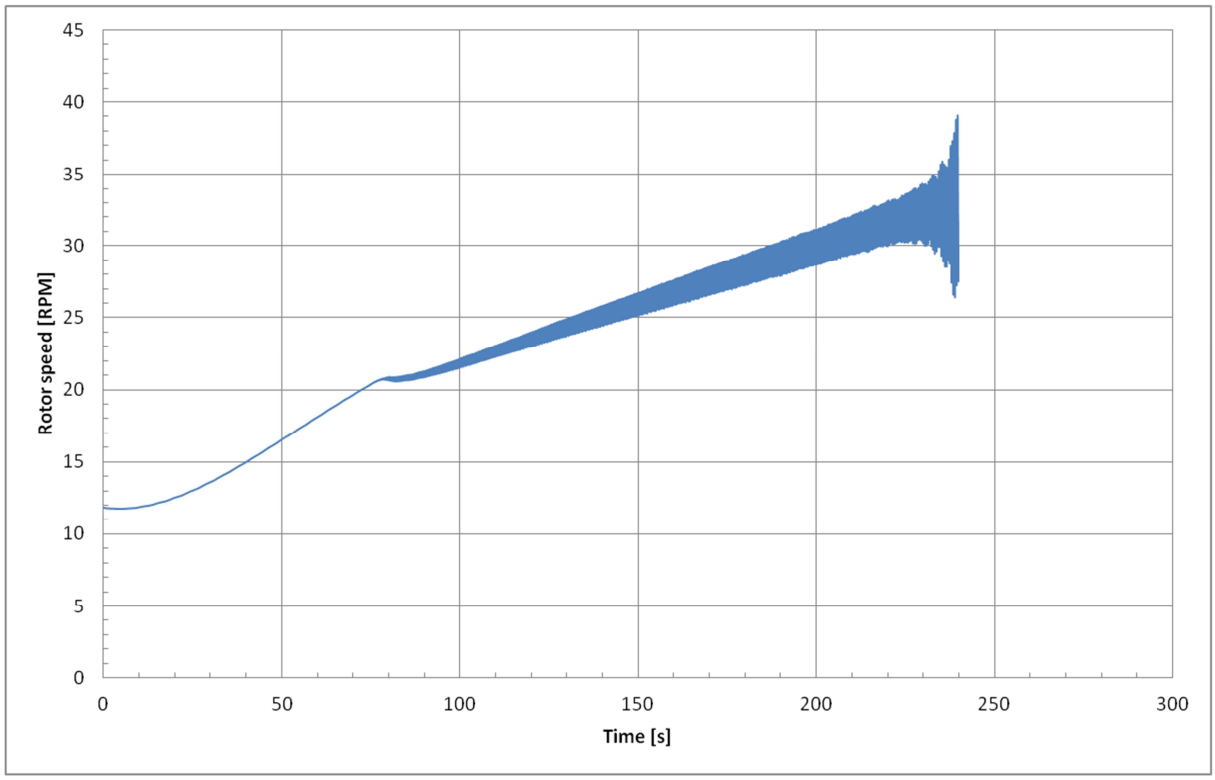

Figure 6.2: Rotor speed as a result of the increasing wind speed in the LCPREP overspeed loadcase.

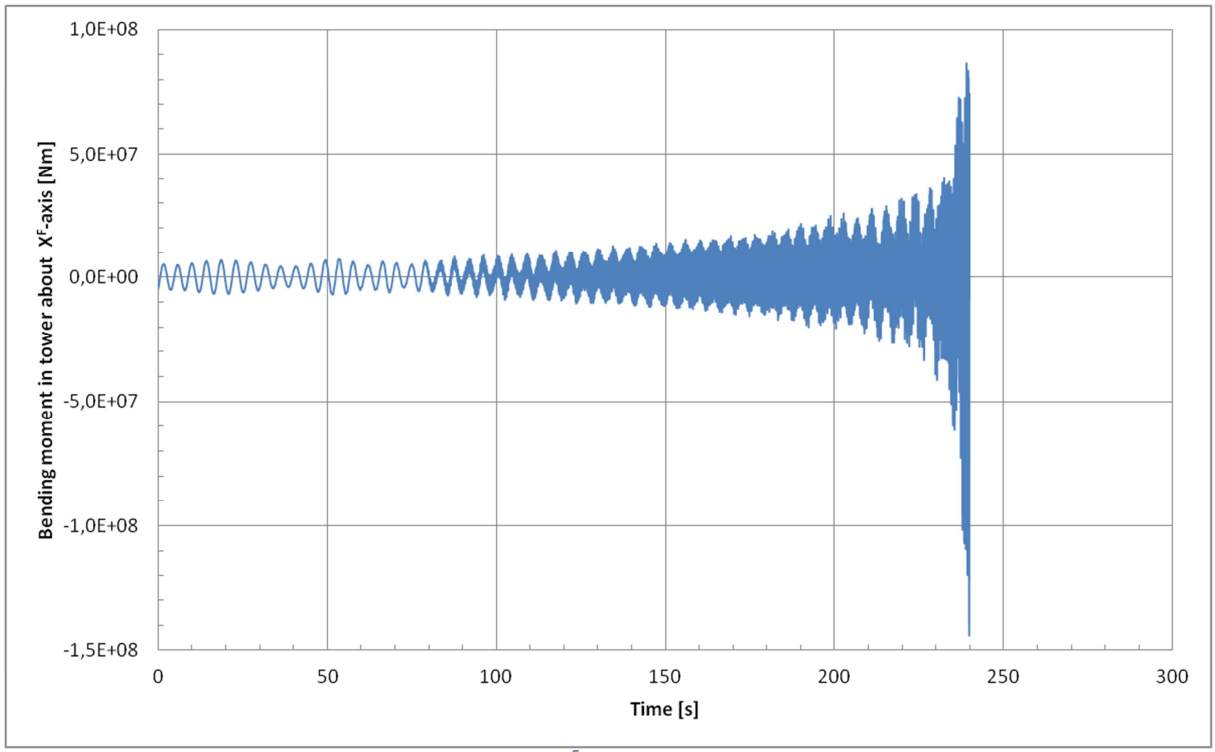

Figure 6.3: Bending moment in the tower about the X^F-axis as a result of the increasing wind speed in the LCPREP overspeed loadcase.

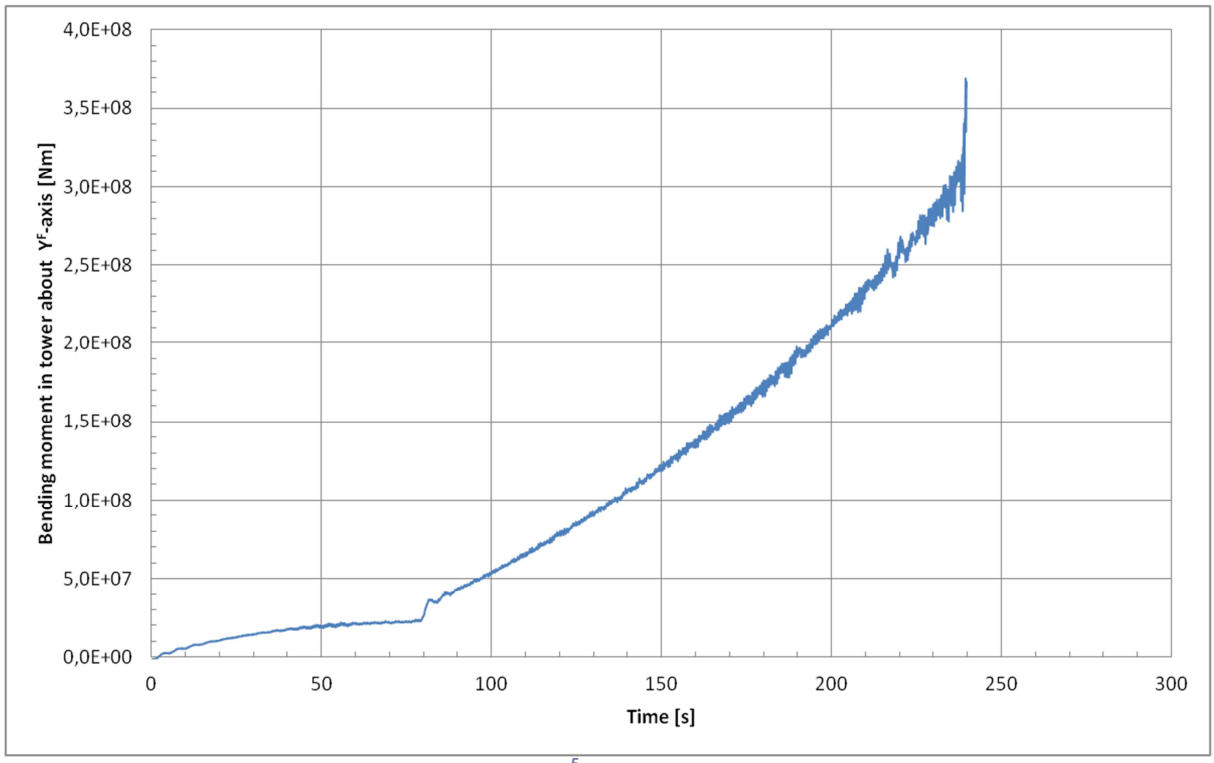

Figure 6.4: Bending moment in the tower about the Y^F-axis as a result of the increasing wind speed in the LCPREP overspeed loadcase.

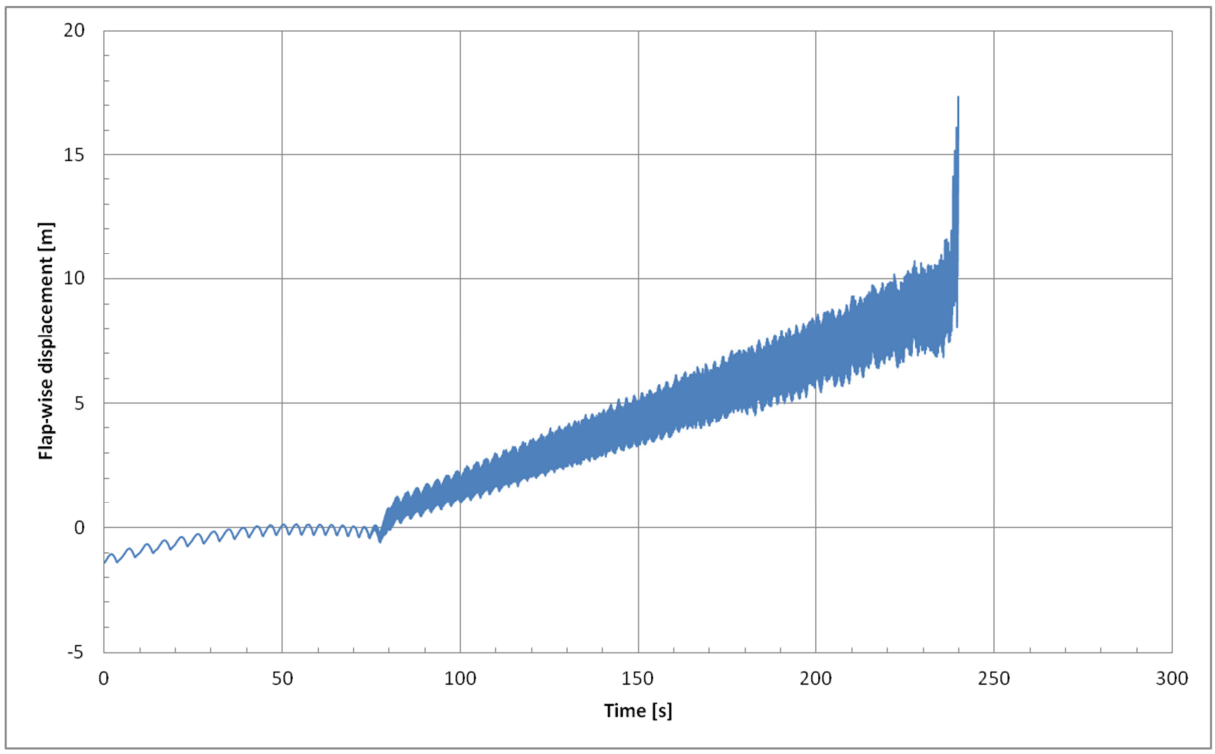

Figure 6.5: Flap-wise displacement blade 1 as a result of the increasing wind speed in the LCPREP overspeed loadcase.

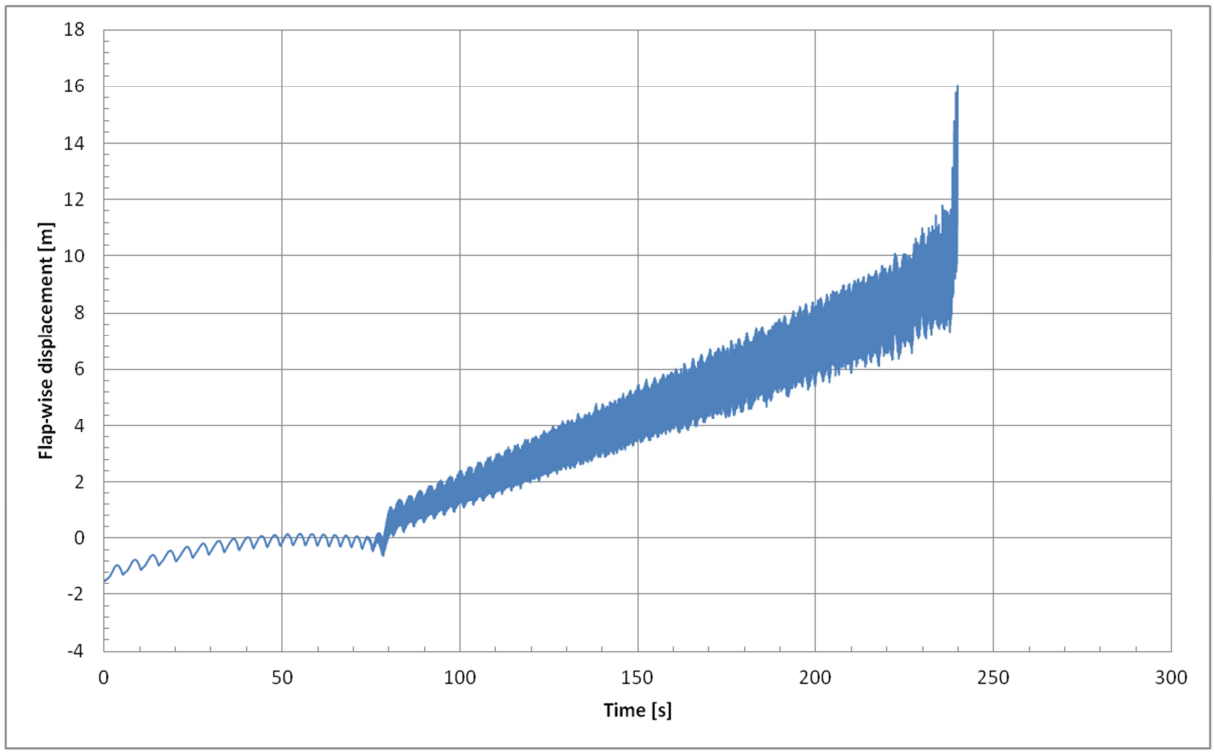

Figure 6.6: Flap-wise displacement blade 2 as a result of the increasing wind speed in the LCPREP overspeed loadcase.

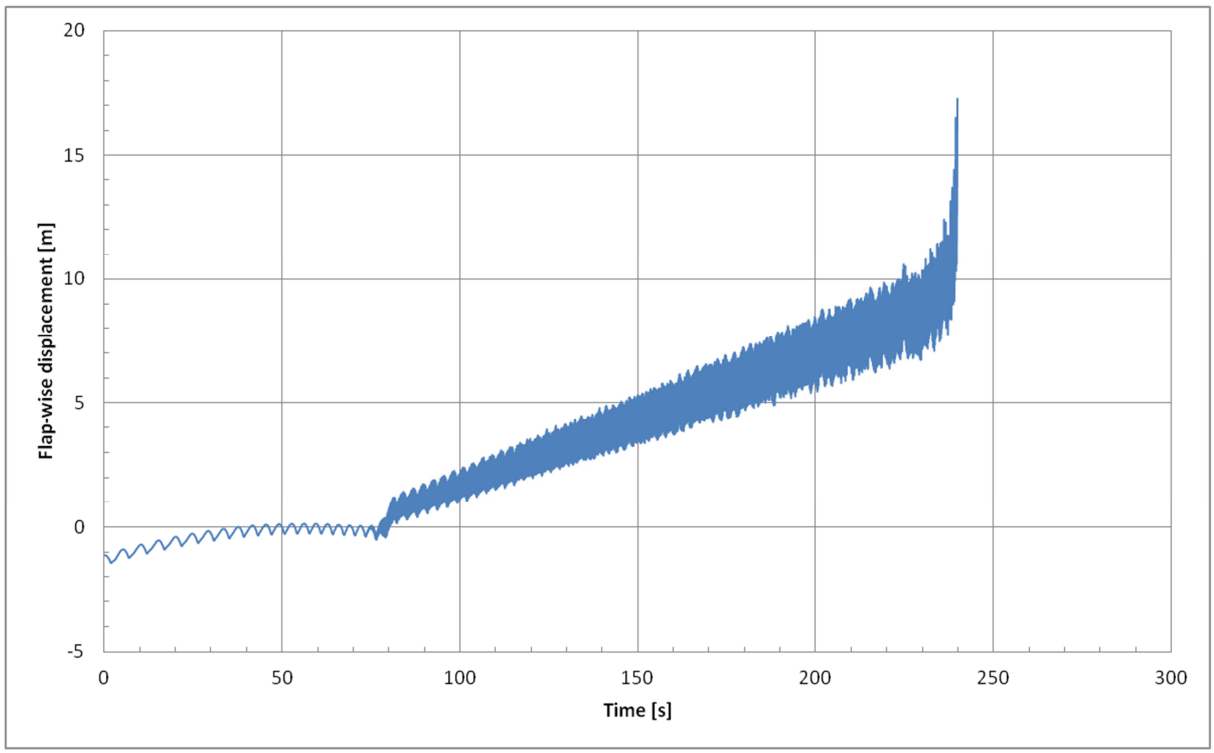

Figure 6.7: Flap-wise displacement blade 3 as a result of the increasing wind speed in the LCPREP overspeed loadcase.

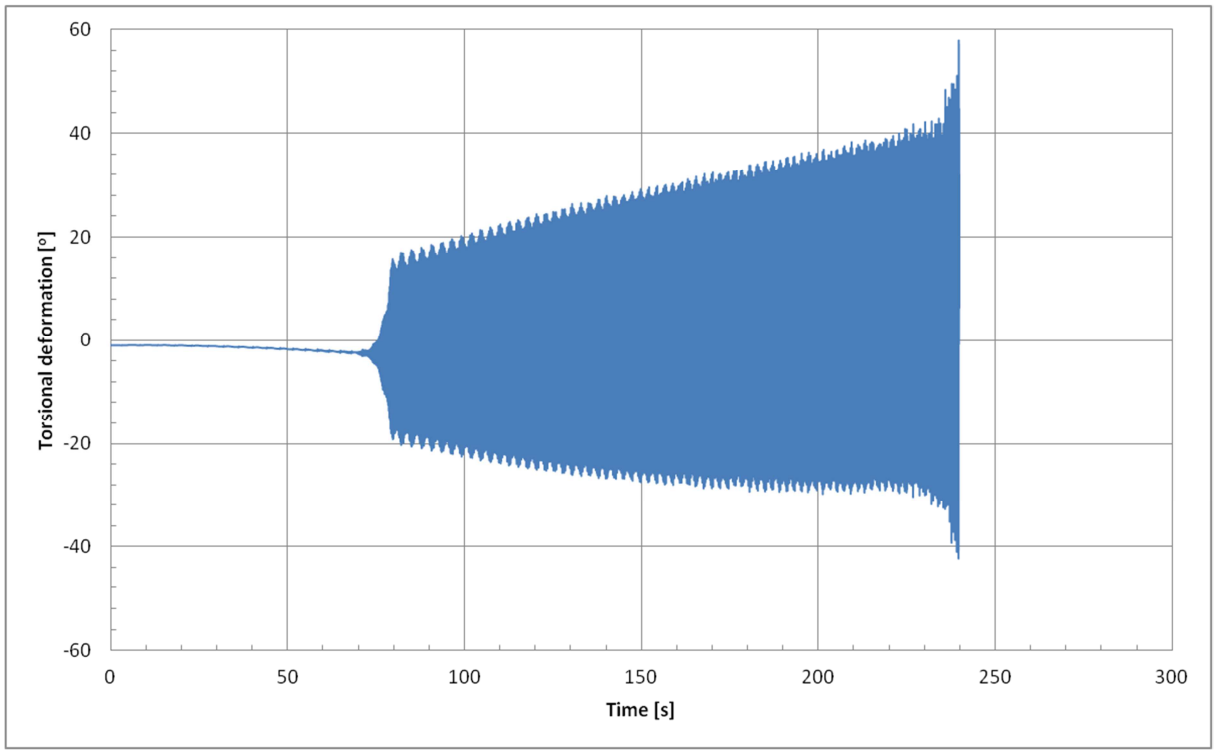

Figure 6.8: Torsional deformation blade 1 as a result of the increasing wind speed in the LCPREP overspeed loadcase.

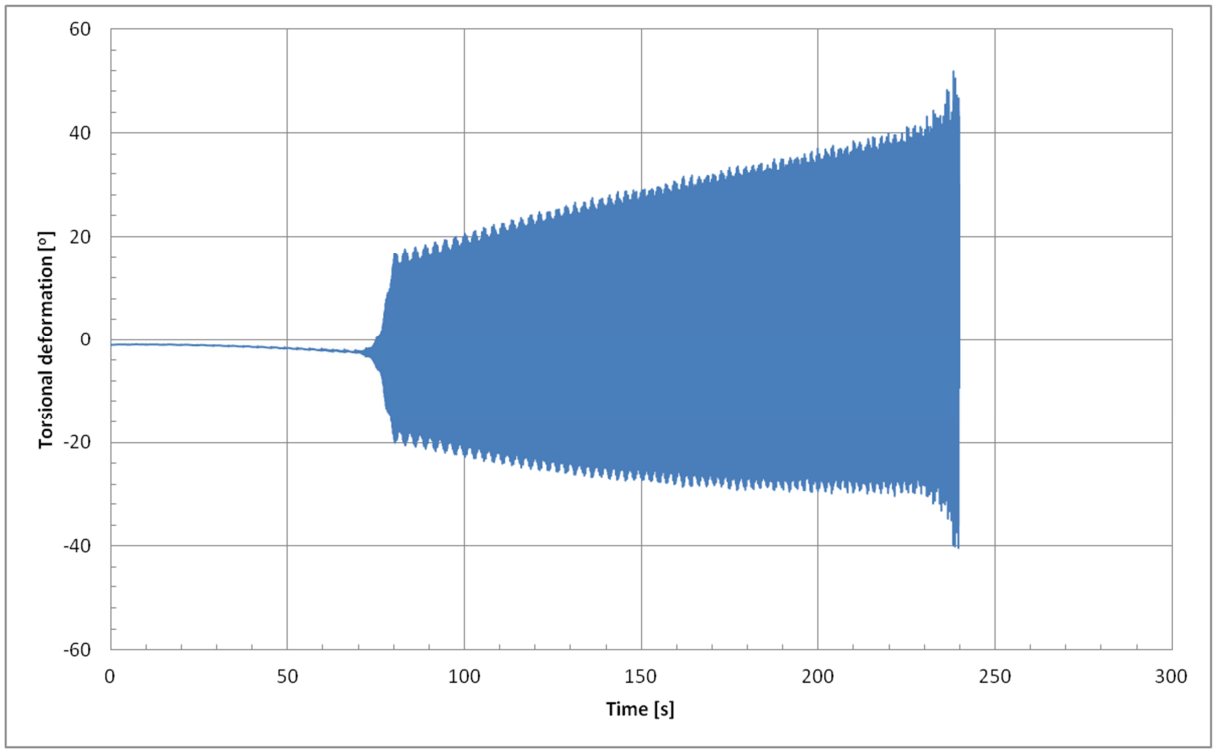

Figure 6.9 Torsional deformation blade 2 as a result of the increasing wind speed in the LCPREP overspeed loadcase.

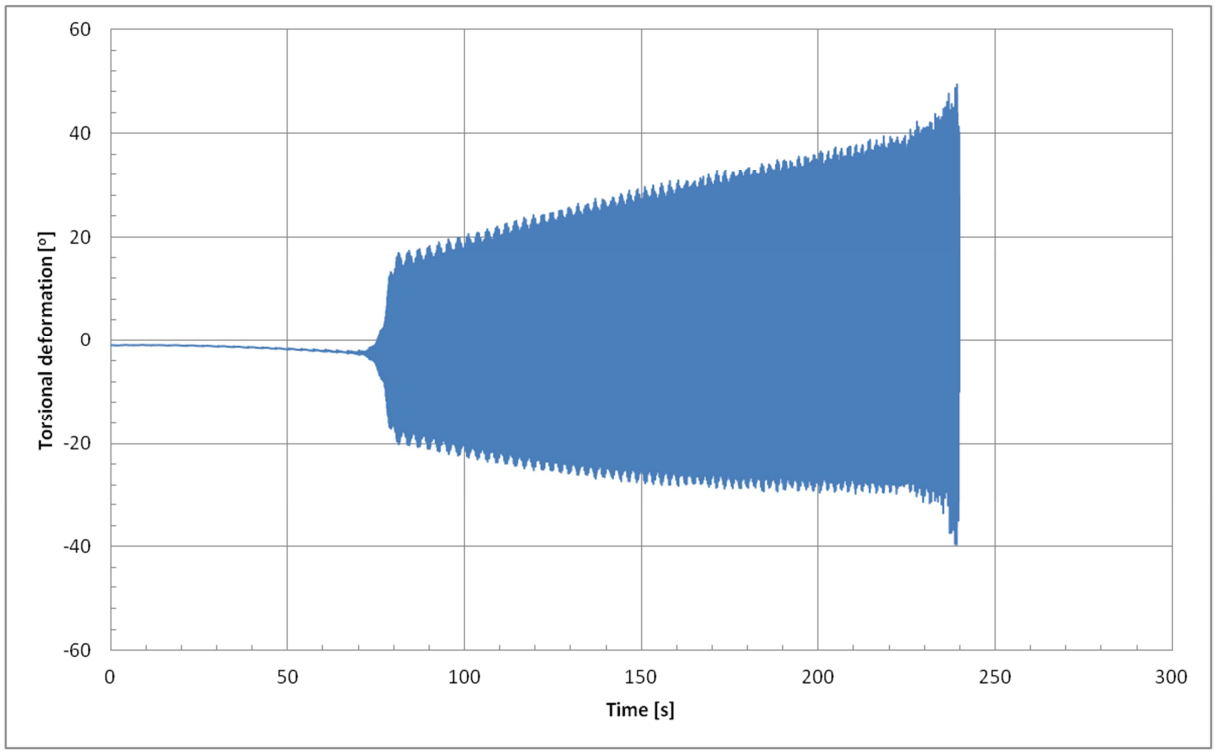

Figure 6.10: Torsional deformation blade 3 as a result of the increasing wind speed in the LCPREP overspeed loadcase.

From these figures it is clear that all three blades display similar behavior in the time domain for the overspeed loadcase. Therefore, in the following section the results for blade 1 will be considered to determine whether classical flutter is deemed to occur or not.

It should be noted that the heavy vibration seen in the figures does not increase exponentially as would be expected for classical flutter, due to the lift-curve having a limited range for attached flow [41]. As stated before the wind speed increases linearly for the overspeed loadcase analysis. Combined with a changing torsional deformation, this influences the angle of attack such that the position on the lift curve for this angle of attack is not always in the attached flow region. This was noted to be a main criterion for classical flutter in Chapter 2.

6.2 Method to Determine the Flutter Speed

In this section the method to determine the flutter speed is presented. The results for blade 1 from the previous section are used in the analysis. The method will consist of various steps. The first three steps serve to prove if classical flutter is present or not as different aspects relevant to classical flutter are considered. Step four of the method explains how the flutter limit can be deduced once it is established in the previous steps that classical flutter occurs. At the end of this section the steps are summarized. It should be noted that since the flap-wise displacement and torsional deformation are pivotal for classical flutter, the subsequent analysis will mainly focus on these two deformations.

6.2.1 Step 1

The first step is to consider if there are any indicators of unusual behavior in the curves which are the result of an instability. It can be seen from all figures, except Figure 6.1 which shows a linearly increasing wind speed, that at around 80 seconds an instability seems to occur. Consulting Figure 6.5 and Figure 6.8, it can be deduced that at around 80 seconds a considerable expansion of the curves takes place. This has the characteristics of classical flutter as the expansion occurs in a short time span. This time span is in the order of a few seconds. Consulting Figure 6.2, it can be seen that the rotor speed around the time of 80 seconds is equal to about 21

[RPM]. This would imply that one blade rotates with $\frac{21}{60} = 0{,}35$ rotations per second. So for the rotor to complete one full revolution, it takes $\frac{1}{0.35} = 2{,}86\ [s]$. Considering the rapid expansion of the torsional deformation, depicted in Figure 6.8, it is possible for this deformation to experience this expansion within one or a couple of rotor revolutions. This is characteristic for classical flutter.

Another indicator of an instability can be found when consulting Figure 6.2 and Figure 6.5. Here it can be seen that at 80 seconds a 'kink' is visible in the curves, after which the unusual behavior takes place. The term unusual is used here to indicate a clearly different behavior of the rotor speed and flap-wise deformation curves before and after 80 seconds.

By plotting the flap-wise and torsional deformation into the same figure, it can be seen which of the two shows the first signs of unusual behavior. This is illustrated in Figure 6.11. In this figure also the wind an rotor speed are included. The wind speed is included as it is relevant to when the instability occurs. The rotor speed is also depicted in the figure as it also contains a 'kink', as such it can be compared with the torsional deformation as well.

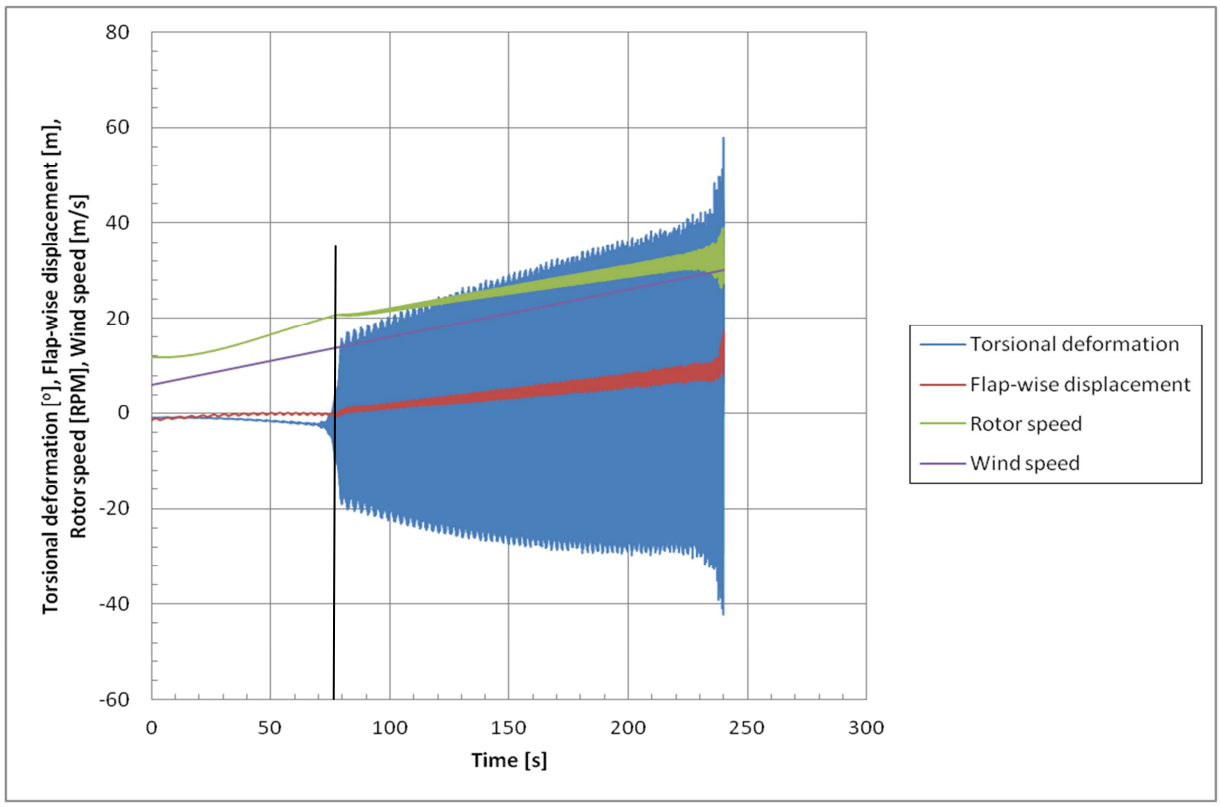

Figure 6.11: Torsional deformation (blue), flap-wise (red), rotor speed (green) and wind speed (purple) for blade 1 as a result of the increasing wind speed in the LCPREP overspeed loadcase. The vertical black line serves to clarify whether torsional expansion occurs prior to the 'kink' present in the flap-wise displacement and rotor speed.

From this figure it is clear that just before the 'kink' of the flap-wise deformation, the torsional deformation shows signs of the expansion which would be expected for classical flutter. Having determined which indicator of the instability occurs first, it will be possible to determine the flutter speed in a subsequent step.

6.2.2 STEP 2

The second step is to zoom in on the deformations in Figure 6.11, by considering the time before classical flutter is deemed to occur and while it develops. This is depicted in Figure 6.12 and Figure 6.13. The aim of the second step is to determine if a phase difference is present between the flap-wise and torsional deformation when classical flutter is deemed to occur, as was mentioned in Chapter 2.

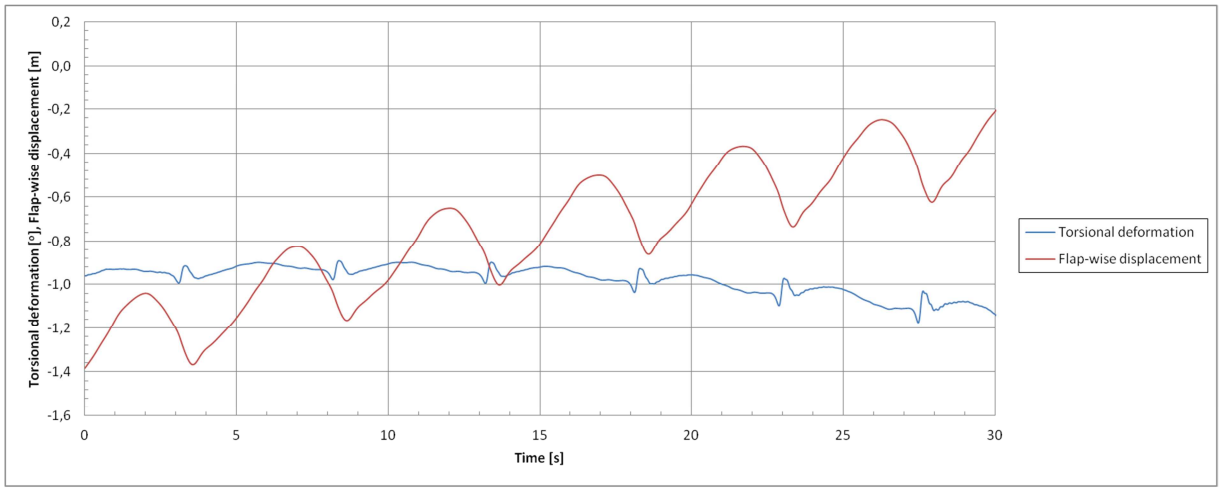

Figure 6.12: Zoom in on flap-wise displacement (red) and torsional deformation (blue) for blade 1, as a result of the increasing wind speed in the LCPREP overspeed loadcase, for the time period prior to classical flutter. Graph shows the results for the first 30 seconds of the simulation and checks whether a phase difference is present.

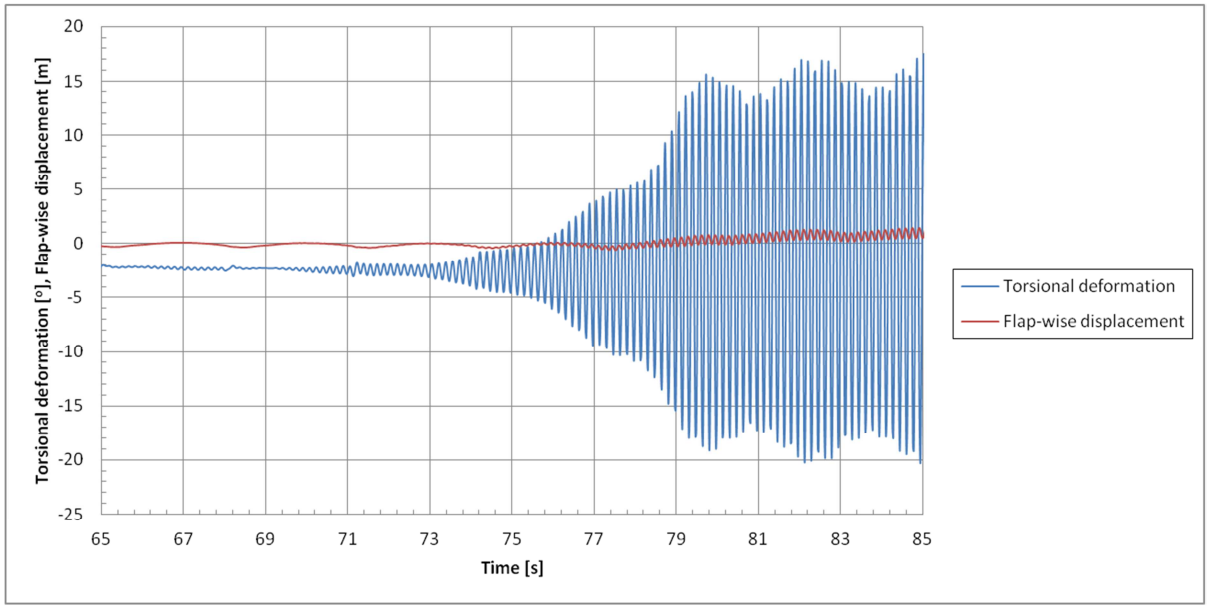

Figure 6.13: Zoom in on flap-wise displacement (red) and torsional deformation (blue) for blade 1, as a result of the increasing wind speed in the LCPREP overspeed loadcase, for the time period including the flutter limit. Graph shows results for the time period of the simulation where the instability occurs.

It should be noted that in Figure 6.12 a 'mini-kink' is present in the curve for the torsional deformation. This phenomena occurs when the flap-wise displacement reaches a minimum, which is about once every five seconds or equal to a frequency of 0,2 Hz. The reason for this behavior is due to the tower 1P frequency. Consulting Figure 6.2, it can be seen that for the first 30 seconds of the simulation the rotor speed is equal to approximately 12 RPM. This means that the 1P frequency equals $12/60 = 0{,}2$ Hz. This correlates with Figure 6.12 and the frequency found for the 'mini-kink'.

Considering both Figure 6.12 and Figure 6.13, it can be deduced that as the instability is approached, small vibrations become visible in the curves for both deformations. The deviations become evident from 70 seconds onwards for the torsional deformation. For the flap-wise deformation, the small deviations start to become evident from 74 seconds onwards. As the phase difference is desired to be found, it is necessary to zoom in further on the region where the deviations for both deformations are present. This is shown in Figure 6.14.

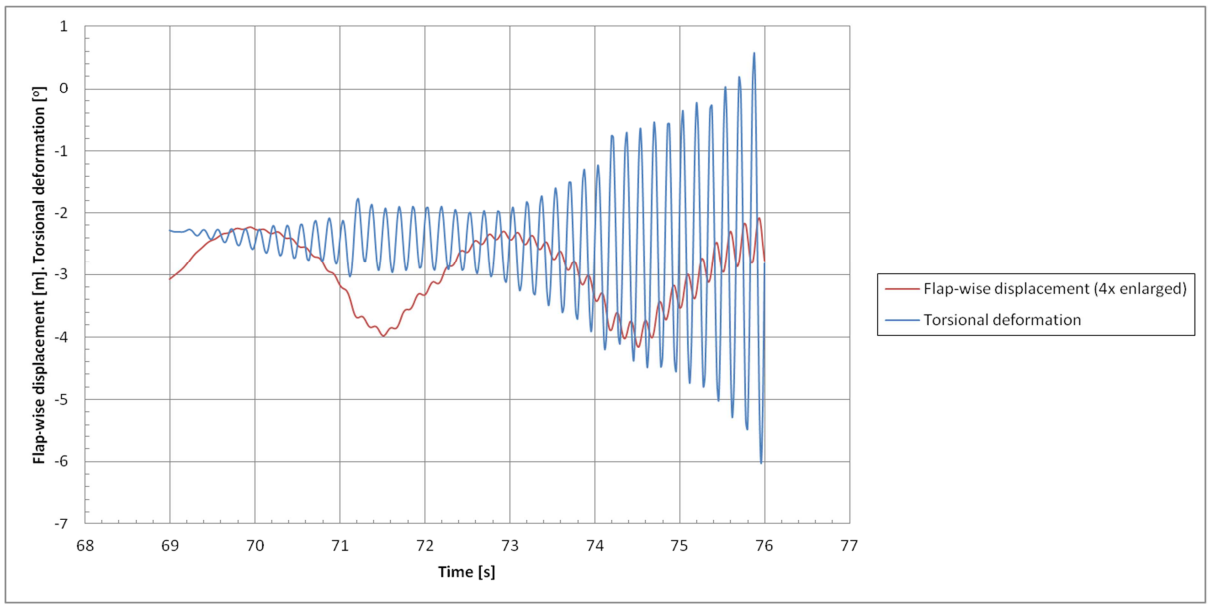

Figure 6.14: Zoom in further for flap-wise displacement (red) and torsional deformation (blue) for blade 1, as a result of the increasing wind speed in the LCPREP overspeed loadcase, to determine existence of a phase difference. The flap-wise displacement values have been multiplied by four to stretch the curve and shifted with a constant, in order to make the phase difference visible.

In this figure it can first of all be seen that the expansion of the torsional deformation occurs at around 69 seconds. This in contrast to the 70 seconds stated earlier. Zooming in has made this clear. Furthermore, it can be seen that there is indeed a phase difference present between the flap-wise and torsional deformations. This is depicted more clear in Figure 6.15 by drawing vertical green lines at certain time instances, which make it clear that when the flap-wise vibration is at a minimum the torsional vibration is not. Actually, based on the two green lines it can be deduced that the phase difference is around 120^0. Referring to Chapter 2, this is not equal to the case of 90^o, but it can still lead to classical flutter. This phase difference remains present, as is depicted in Figure 6.16. Here it can be seen that at times beyond the flutter limit, the phase difference is indeed still present.

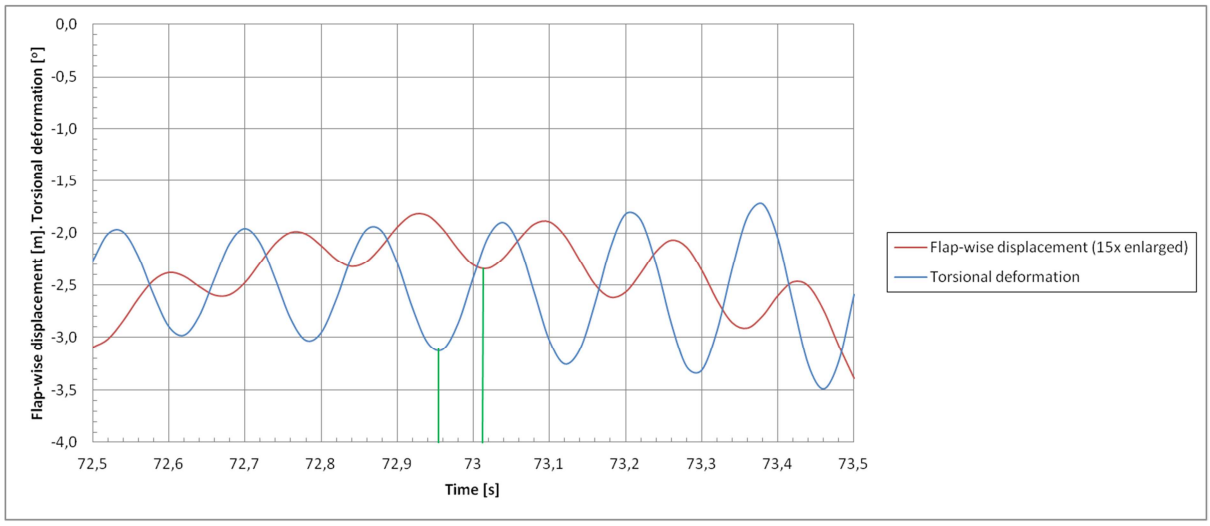

Figure 6.15: Zoom in further for flap-wise displacement (red) and torsional deformation (blue) for blade 1, as a result of the increasing wind speed in the LCPREP overspeed loadcase, to determine existence of a phase difference. The flap-wise displacement values have been multiplied by 15 to stretch the curve and shifted with a constant, in order to make the phase difference visible.

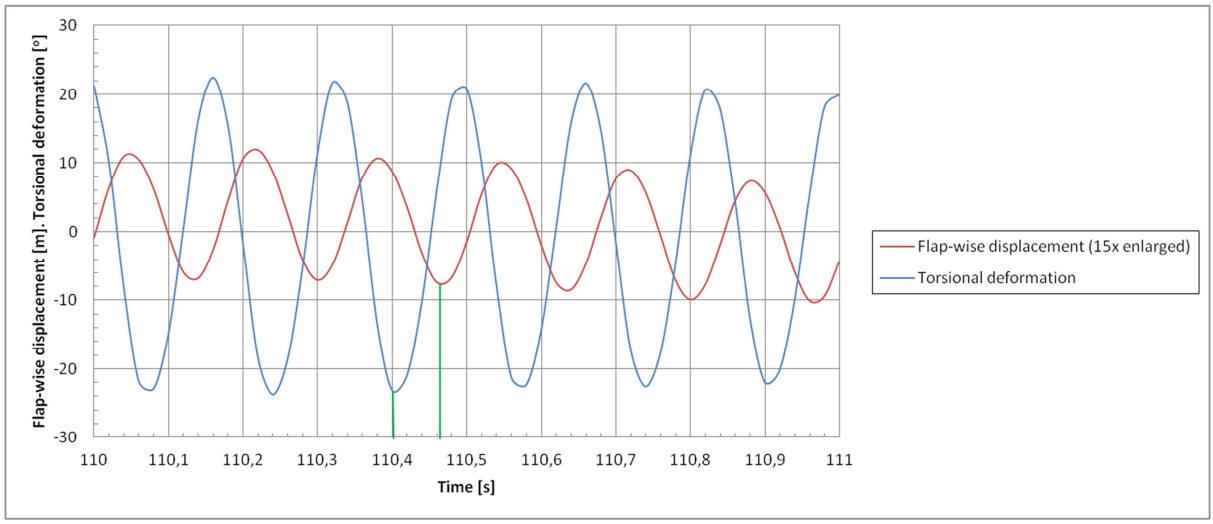

Figure 6.16: Zoom in on flap-wise (red) and torsional deformation (blue)peaks for blade 1, as a result of the increasing wind speed in the LCPREP overspeed loadcase, to show that the phase difference between the two remains present. The flap-wise displacement values have been multiplied by 15 to stretch the curve and shifted with a constant, in order to make the phase difference visible.

6.2.3 STEP 3

Now that the phase difference is established, the third step is to consider if the instability is a self-exciting instability. This is an essential aspect of the classical flutter phenomena, as stated in Chapter 2. To this extent, Figure 6.11 and Figure 6.13 are consulted. It was already established that there is a rapid expansion of in particular the torsional deformation. As this expansion occurs within one or a couple of rotor revolutions and no other reason was found present for this expansion, the only viable explanation is that of self-excitation. This is deemed a viable explanation because the conclusions of the two other steps are taken into account. Combining the phenomena discussed in the previous steps and their associated conclusions, self-excitation is viable as the criteria for classical flutter to occur are present. Indeed, based on Figure 6.14 it can be seen that beyond 69 seconds the self-enhancement mentioned in Chapter 2 is most clear. Furthermore, as the overspeed loadcase is performed with a linearly increasing wind speed, this cannot be the reason for the sudden expansion as there is no step-input in the wind. Next to this the rotor speed is determined based on the wind speed, meaning that the instability can only considerably increase within the short time span if it is a self-exciting instability.

As an extra check, another simulation is performed where all parameters except the blade *flap-wise stiffness* value are altered. These values have been given an exaggerated value of one million times the original input data. The reason for this is that it is desired to compare the time history behavior of the flap-wise displacement found with the original LCPREP simulation, with a simulation where the stiffness value has been changed. By comparing the two results it should be clear that the instability found for the simulation with the original data indeed hints at classical flutter. The results of this simulation is provided in Figure 6.17.

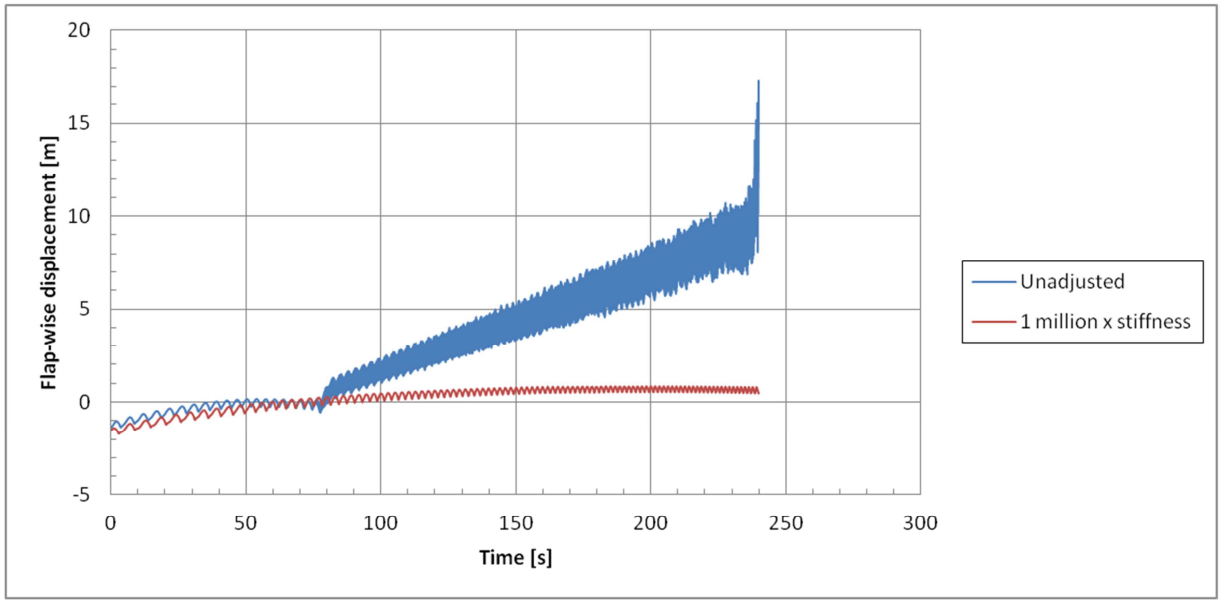

Figure 6.17: Flap-wise displacement as a result of the increasing wind speed in the LCPREP overspeed loadcase. The graph shows the result for the original data (blue) and for the case with one million times higher *torsional stiffness* values of the blade (red).

From this figure it is clear that increasing the *flap-wise stiffness* values results in the absence of the instability encountered in the simulation with the original data. This correlates with the theory in Chapter 2 that increasing the flap-wise stiffness will increase the flutter limit. In other words, the instability responds to the increase of the *flap-wise stiffness* values as one would expect classical flutter to do. Hence the result obtained substantiates the statement that the instability found indeed is classical flutter.

6.2.4 STEP 4

Considering the results and conclusions obtained so far, it can be stated that the instability present in the results of the simulation indeed is classical flutter. Based on this conclusion, step 4 can be performed. This step aims to find the flutter speed. This is achieved by first consulting the rotor speed plot, Figure 6.2, by zooming in on the time period including the determined time instance beyond which self-enhancement is determined to occur. This figure is presented in Figure 6.18. Based on this figure and the results obtained thus far, a first estimation of the flutter speed is made. The value for the *rotor speed* is determined at 73 seconds and it is found to be 20,12 RPM. This is indicated in Figure 6.18 with the red lines. The choice for this value is deemed appropriate as it is beyond the determined time instance where classical flutter is thought to occur.

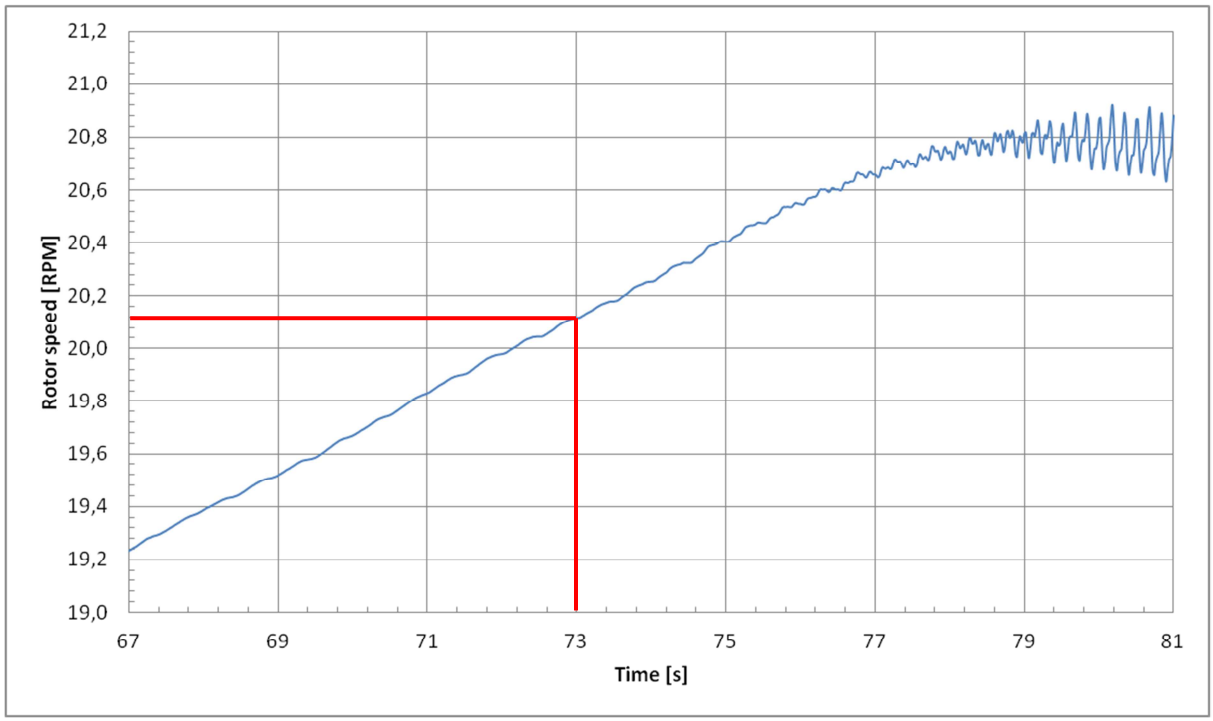

Figure 6.18: Zoom in on the rotor speed, as a result of the increasing wind speed in the LCPREP overspeed loadcase, to determine the flutter speed. The time period considered includes the flutter limit. The two red lines are present to make to easier to read the flutter speed at the time of 69 seconds.

What needs to be done next, is to perform several simulations with the LCPREP overspeed loadcase but now with a fixed *wind* and *rotor speed*. The first simulation is based on the *rotor* speed of 20,12 RPM. Based on the results obtained with this value it can be deduced whether classical flutter is present or not. If it is deemed to have occurred, the next simulation is performed with a *rotor* speed value 0,25 RPM less than the previous one. Vice versa in case classical flutter has not occurred. By doing this, the first *rotor speed* value at which the simulation shows the classical flutter instability is found. This is done because this yields a more accurate value of the flutter limit, compared to reading it from Figure 6.2 or Figure 6.18. To this extent the table containing the simulation data is presented in Table 6.1. The value of 0,25 RPM is deemed sufficient in this case, with respect to the accuracy of the flutter speed. Furthermore, the associated *wind speed* values can be found in Figure 6.1.

Table 6.1: Input data used in the LCPREP overspeed loadcase simulation to determine flutter limit.

Time [s]	***Wind speed [m/s]***	***Rotor speed [RPM]***
64,7	12,47	18,87
70,0	12,97	19,62
71,2	13,12	19,87
73,0	13,30	20,12
74,7	13,47	20,37
76,6	13,66	20,62
79,6	13,97	20,82

Based on these simulations the results for the time instances indicated in green in Table 6.1 are presented since they prove to show when the instability occurs. Before presenting the results it is important to note some key aspects which are considered when analyzing the results of the simulations. To determine if classical flutter is present at a specific *rotor speed* value, the focus is put on the following aspects

- Check whether the time history behavior of especially the torsional deformation shows signs of an instability akin to classical flutter, similar to the expansion seen in Figure 6.8.
- Check if the extreme values for the torsional deformation are comparable to those encountered in Figure 6.8 during the occurrence of the instability.
- Check if the time history behavior for the aerodynamic angle of attack and lift coefficient show signs of an instability and both obtain extreme values comparable to the stall values for the NACA63418 airfoil used at the blade tip.
- Check whether the flap-wise displacement and torsional deformation have the same frequency and a phase difference is present, as would be expected in case of classical flutter.

The results for the relevant simulations are presented in Figure 6.19-Figure 6.29. Only the first 50 seconds of each simulation is shown in the graphs, both for clarity reasons and because the maximum values are obtained within these 50 seconds.

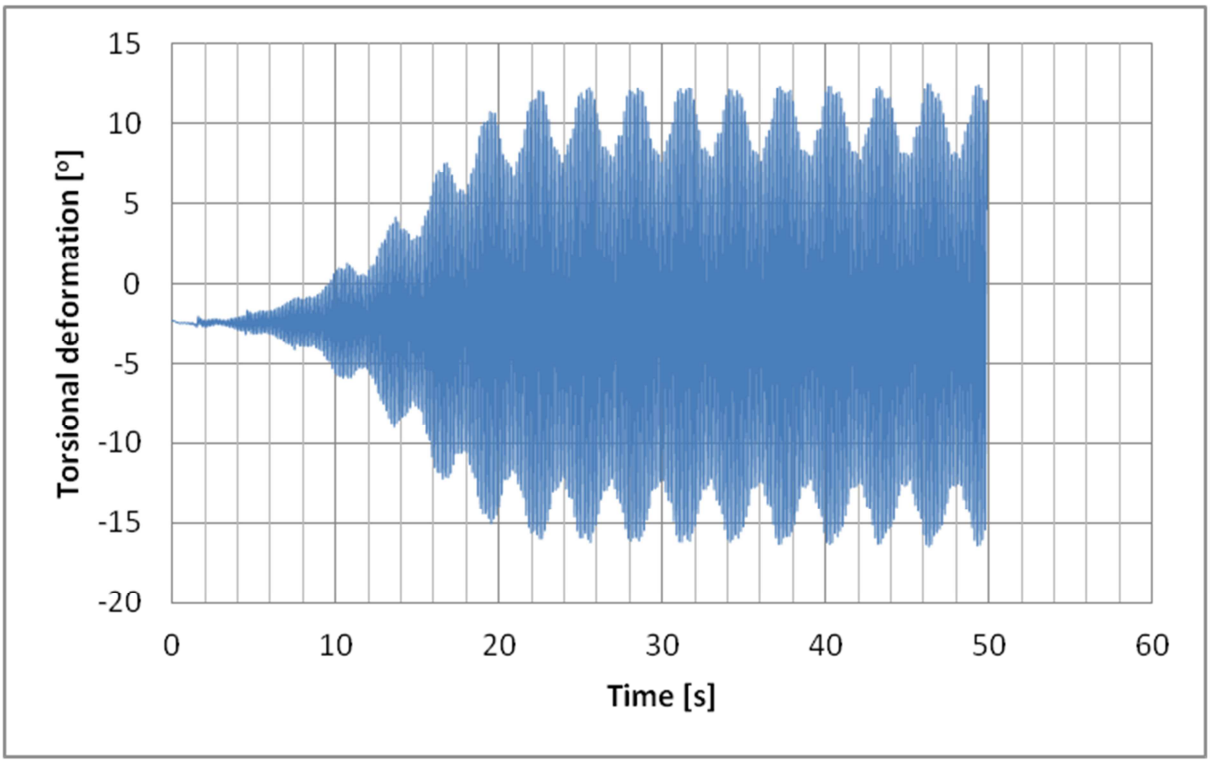

Figure 6.19: Torsional deformation blade 1 as a result of the LCPREP overspeed loadcase with a fixed *wind* and *rotor speed* value of 13,12 [m/s] and 19,87 [RPM], respectively.

From this figure it can be deduced that indeed both a sudden expansion and comparable extreme values are present as seen in Figure 6.8.

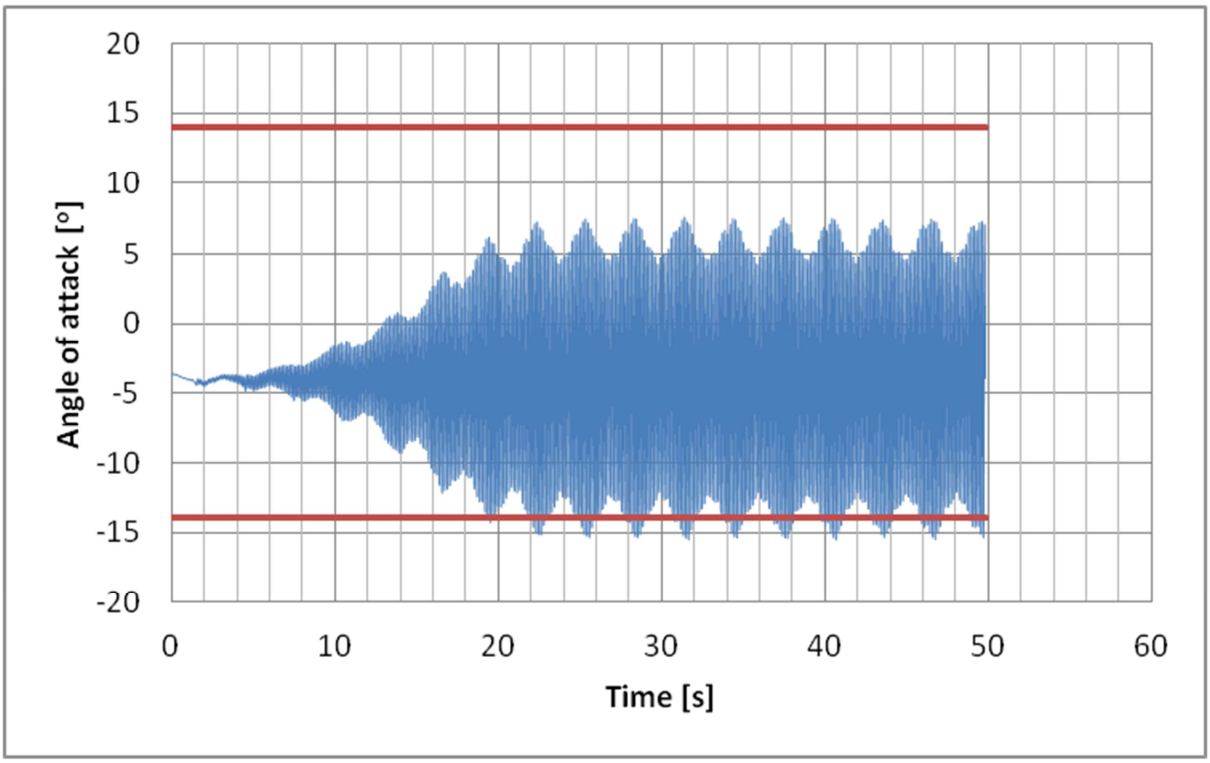

Figure 6.20: Aerodynamic angle of attack of blade 1 as a result of the LCPREP overspeed loadcase with a fixed *wind* and *rotor speed* value of 13,12 [m/s] and 19,87 [RPM], respectively. The red lines indicate the extreme values for the NACA63418 airfoil.

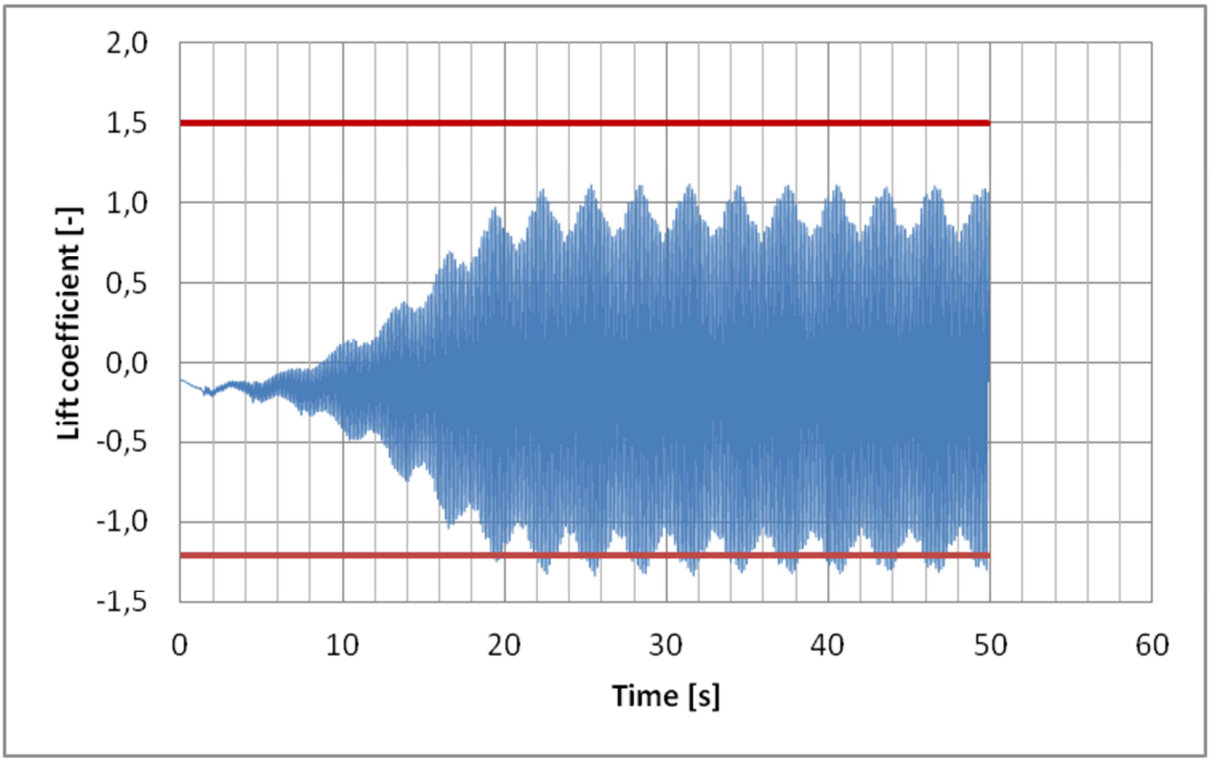

Figure 6.21: Lift coefficient at the tip of blade 1 as a result of the LCPREP overspeed loadcase with a fixed wind and rotor speed value of 13,12 [m/s] and 19,87 [RPM], respectively. The red lines indicate the extreme values for the NACA63418 airfoil.

Considering Figure 6.20 and Figure 6.21, it is evident that for this simulation there is an indication of an instability present. Both curves show signs of a sudden increase in values, similar to the torsional deformation, and obtain extreme values similar to those of the

NACA63418 airfoil. The latter is indicated by the red lines, where it is clear that not only is an extreme value approached, but also crossed. This crossing can be assigned to the dynamic stall effect, which would be expected in case of classical flutter.

The last key aspect is related to the frequency of and phase difference between the flap-wise displacement and torsional deformation.

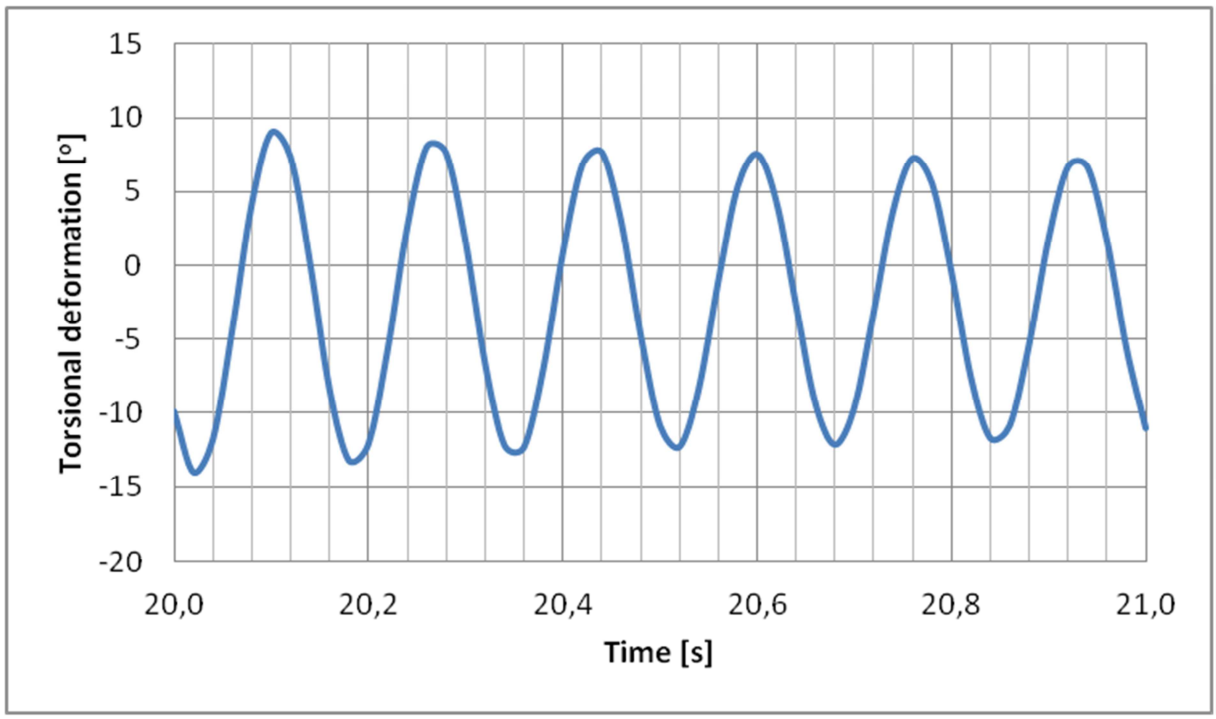

Figure 6.22: One second time period of the torsional deformation of blade 1 as a result of the LCPREP overspeed loadcase with a fixed *wind* and *rotor speed* value of 13,12 [m/s] and 19,87 [RPM], respectively.

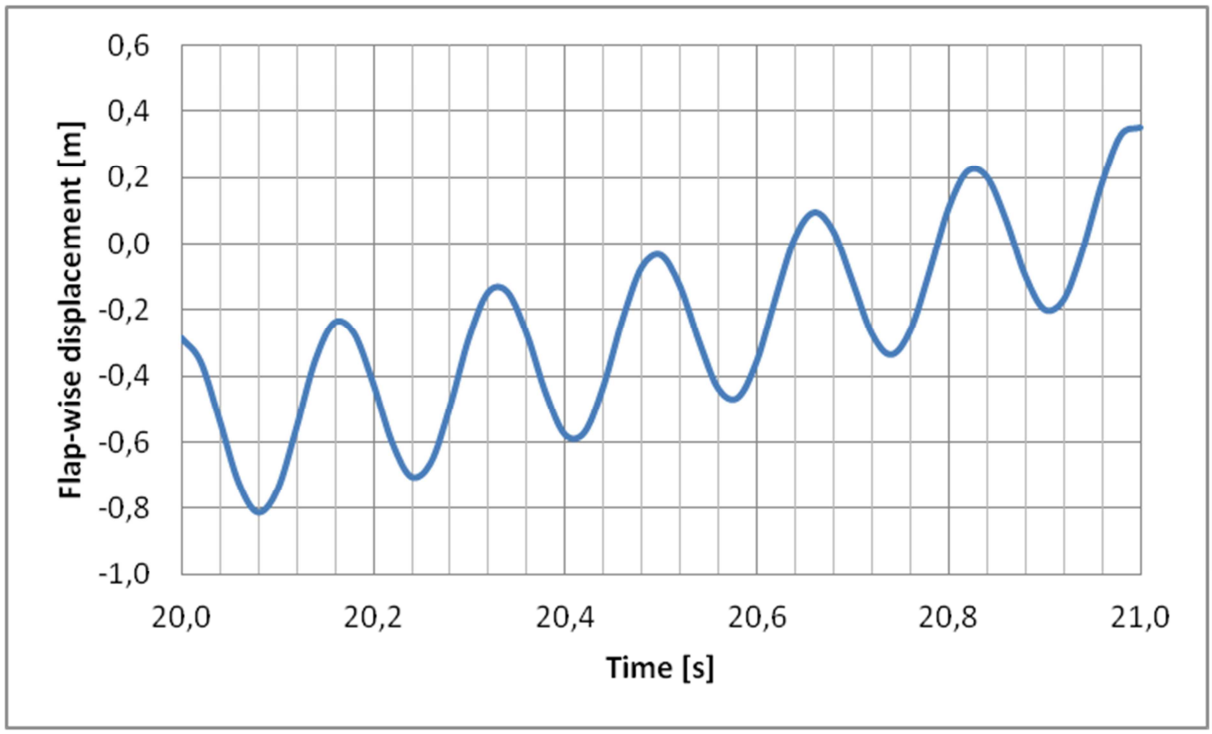

Figure 6.23: One second time period of the flap-wise displacement of blade 1 as a result of the LCPREP overspeed loadcase with a fixed wind and rotor speed value of 13,12 [m/s] and 19,87 [RPM], respectively.

Counting the number peaks in both Figure 6.22 and Figure 6.23, for the same time period, yields a frequency of 6 Hz for the flap-wise displacement and torsional deformation. Next to this it is evident that a clear phase difference is present between the two. This can easily be deduced by consulting both figures at the time instance of 20 seconds. This would all be expected in case of classical flutter.

Considering the results obtained for the simulation with a *rotor speed* of 19,87 RPM it can be stated that this value represents the flutter limit. This statement is substantiated because the four key aspects are met and lowering the *rotor speed* by 0,25 RPM yields results that do not meet all those key aspects. The results for the simulation with 19,62 RPM proves this.

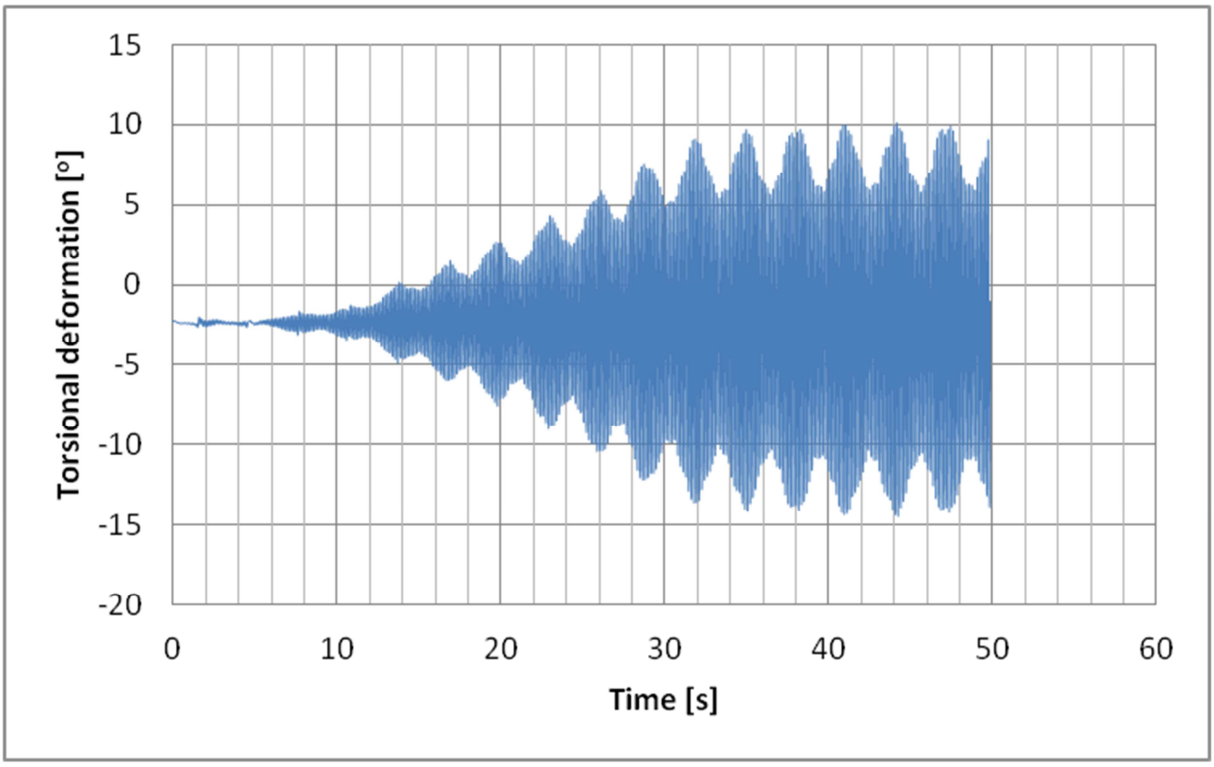

Figure 6.24: Torsional deformation blade 1 as a result of the LCPREP overspeed loadcase with a fixed wind and rotor speed value of 12,97 [m/s] and 19,62 [RPM], respectively.

Compared to the results presented in Figure 6.19, the expansion of the torsional deformation is clearly more gradual now. Also, the extreme values are lower and less comparable to those seen in Figure 6.8..

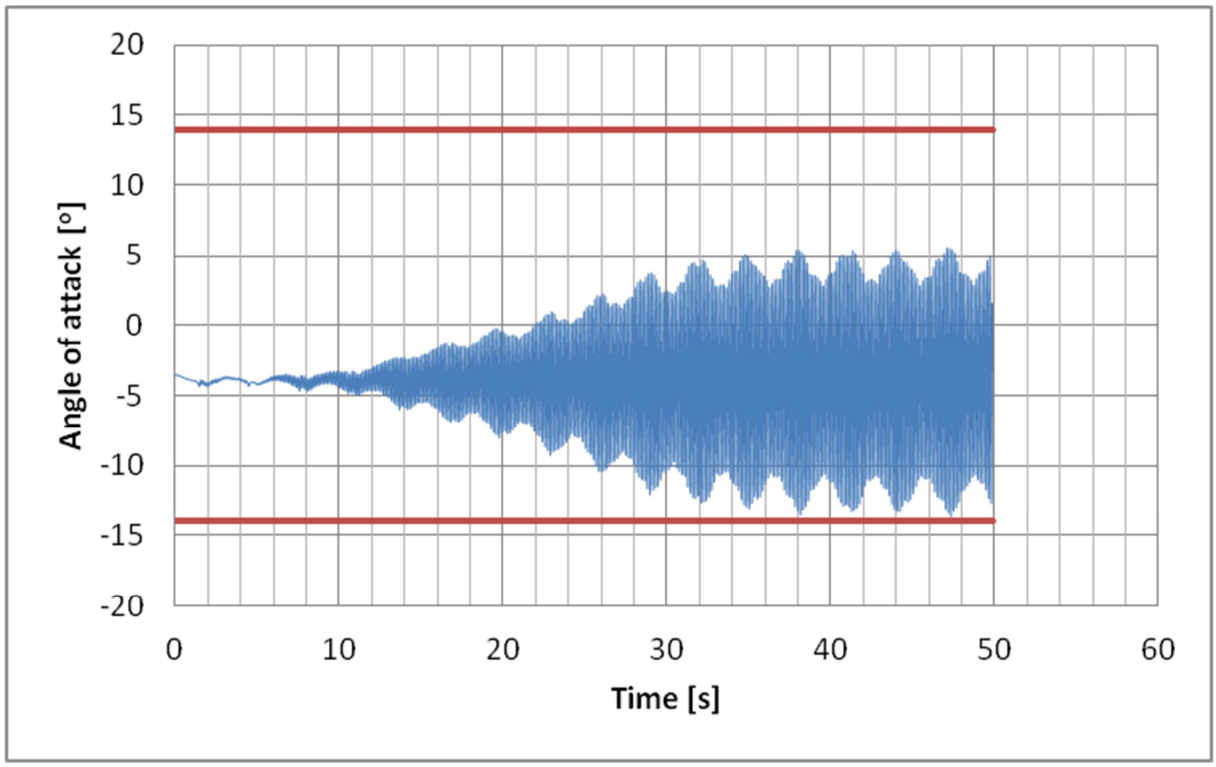

Figure 6.25: Aerodynamic angle of attack of blade 1 as a result of the LCPREP overspeed loadcase with a fixed *wind* and *rotor speed* value of 12,97 [m/s] and 19,62 [RPM], respectively. The red lines indicate the extreme values for the NACA63418 airfoil.

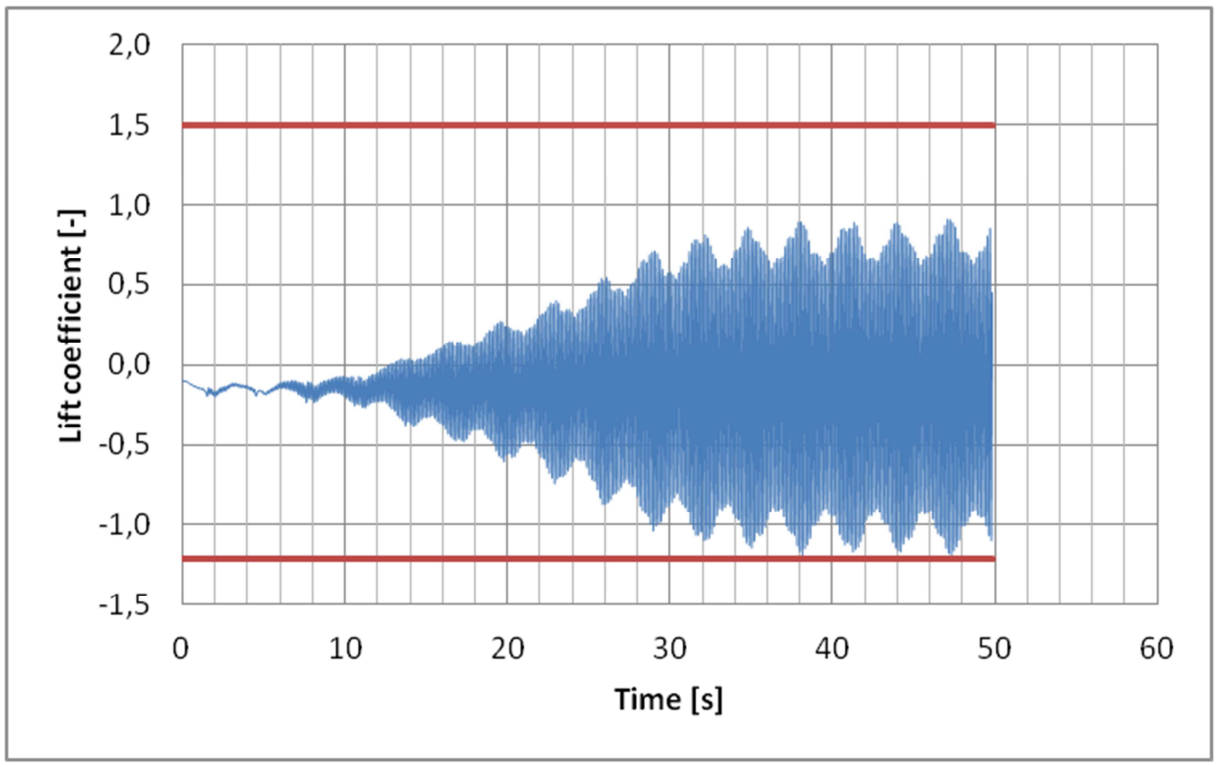

Figure 6.26: Lift coefficient at the tip of blade 1 as a result of the LCPREP overspeed loadcase with a fixed wind and rotor speed value of 12,97 [m/s] and 19,62 [RPM], respectively. The red lines indicate the extreme values for the NACA63418 airfoil.

Considering the above two figures, the same conclusion can be drawn as for the time history behavior of the torsional deformation. Furthermore, the red lines are no longer crossed, which would be expected if classical flutter occurred as the dynamic stall effect would be present.

Although the frequency of the flap-wise displacement and torsional deformation proves to be the same (6 Hz) and there is a phase difference present between the two, the *rotor speed* of 19,62 is not deemed the flutter speed. This is because the key aspects are not met with the same conviction as was the case for the *rotor speed* of 19,87 RPM.

Lowering the *rotor speed* further yields result which stray further and further away from the key aspects which are to be met. To prove this point with a clear result, the figures related to the simulation for the *rotor speed* of 18,87 RPM are presented. These figures show that one is moving away from the flutter speed because it is no longer possible to recognize an instability similar to classical flutter. The results are presented in Figure 6.27-Figure 6.29.

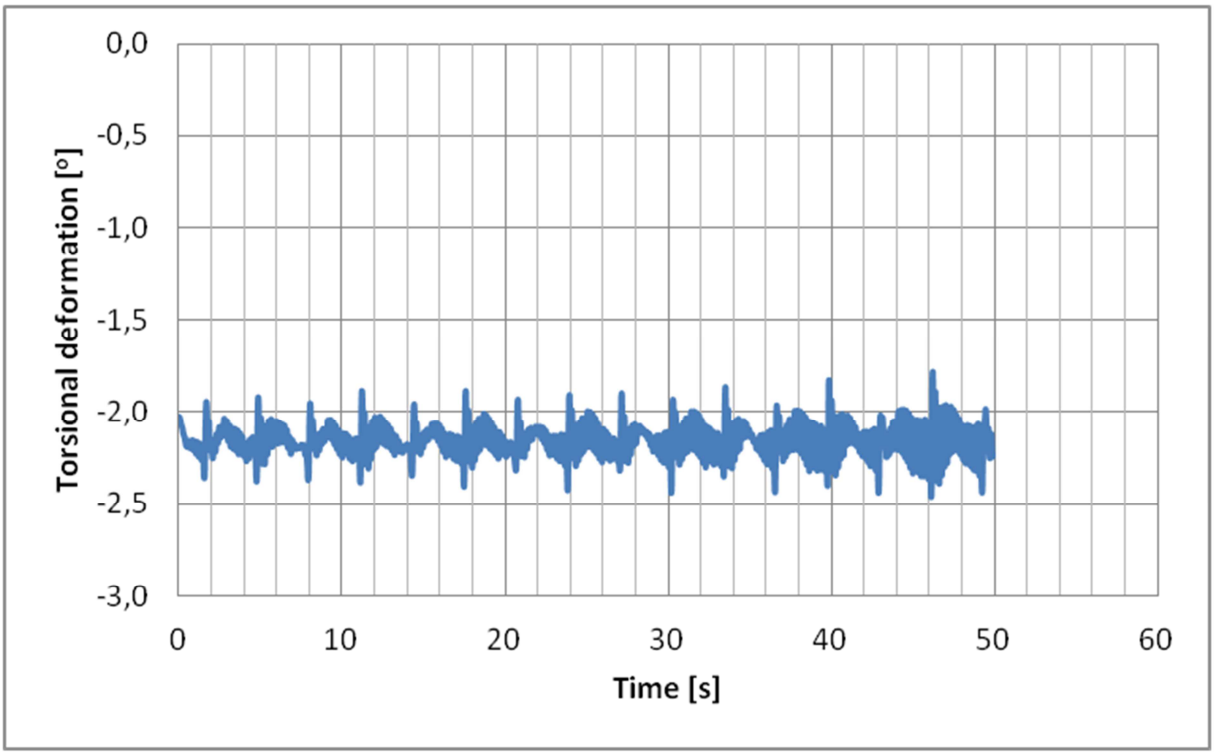

Figure 6.27: Torsional deformation blade 1 as a result of the LCPREP overspeed loadcase with a fixed wind and rotor speed value of 12,47 [m/s] and 18,87 [RPM], respectively.

In this figure there is no longer an instability such as classical flutter recognizable. Therefore the values for the torsional deformation in this figure are nothing like the result shown in Figure 6.8.

Furthermore, Figure 6.28 and Figure 6.29 show that the key aspect of the angle of attack and lift coefficient are nowhere close to being met.

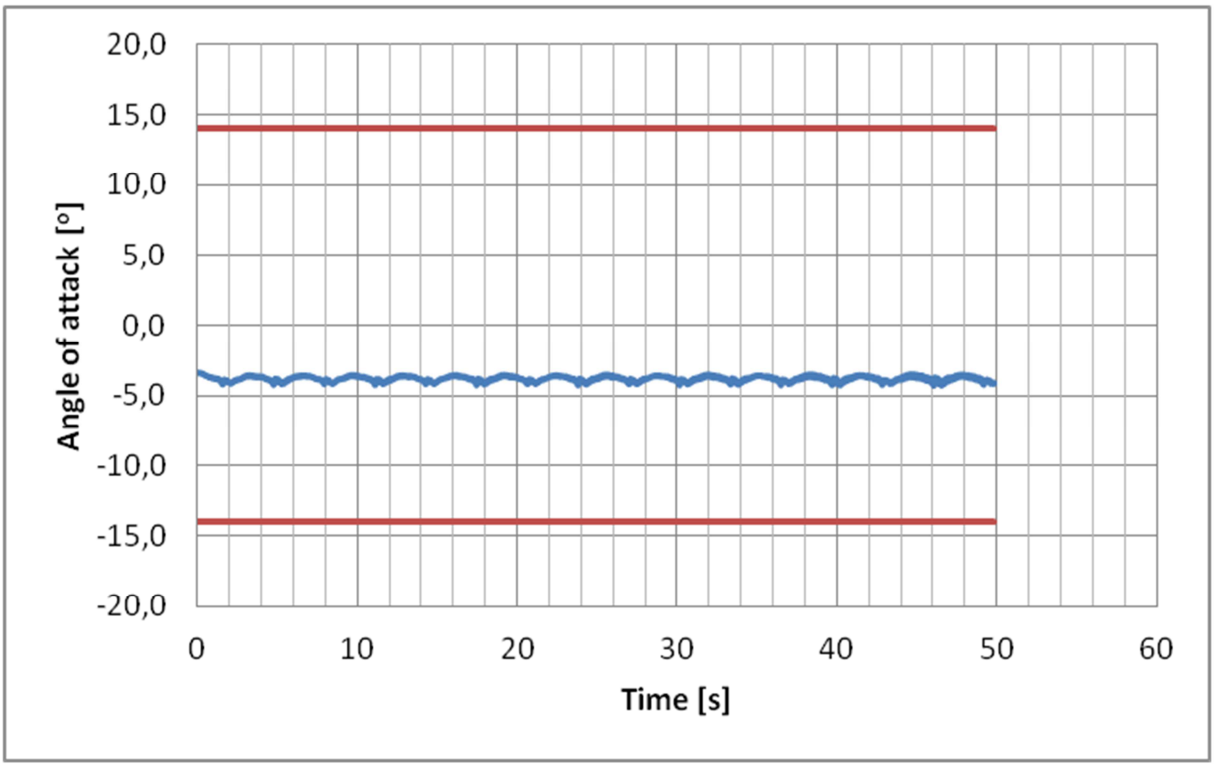

Figure 6.28: Aerodynamic angle of attack of blade 1 as a result of the LCPREP overspeed loadcase with a fixed *wind* and *rotor speed* value of 12,47 [m/s] and 18,87 [RPM], respectively. The red lines indicate the extreme values for the NACA63418 airfoil.

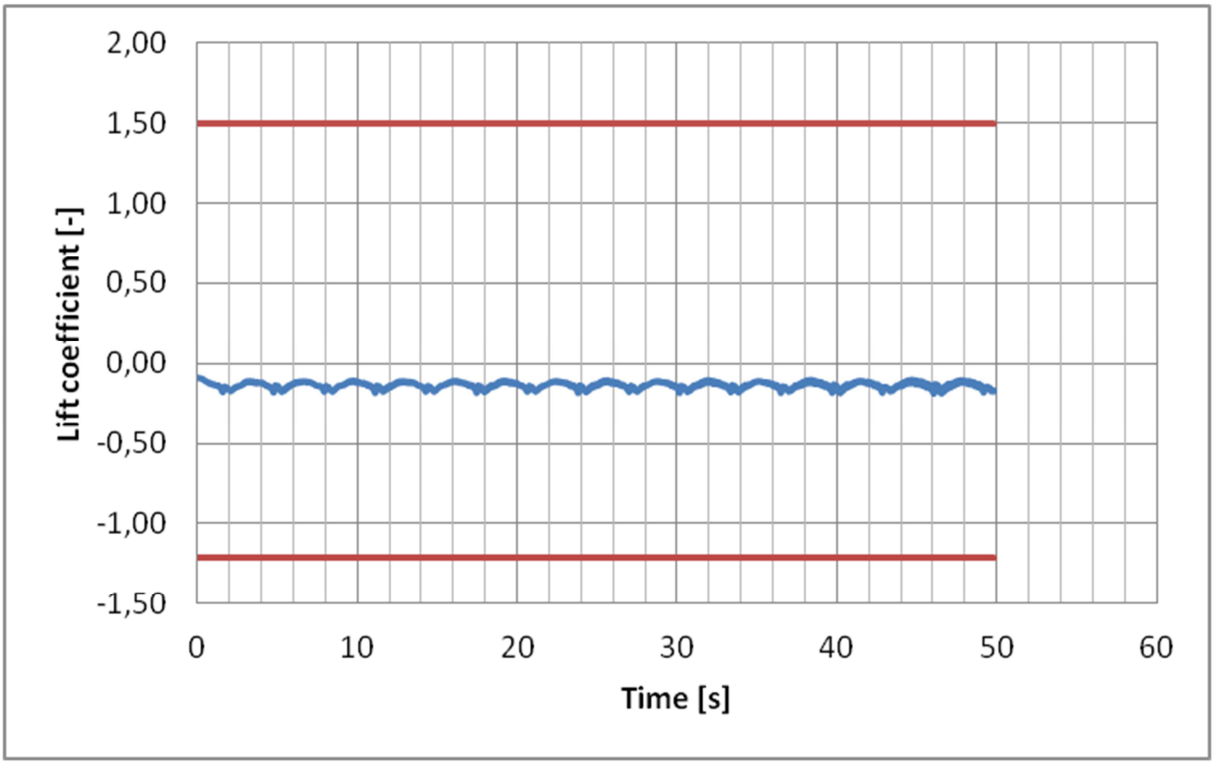

Figure 6.29: Lift coefficient at the tip of blade 1 as a result of the LCPREP overspeed loadcase with a fixed wind and rotor speed value of 12,47 [m/s] and 18,87 [RPM], respectively. The red lines indicate the extreme values for the NACA63418 airfoil.

6.2.5 *SUMMARIZING THE STEPS*

To summarize, the method to determine if classical flutter occurs and how the flutter speed can be found using PHATAS, consists of four steps. The first step considers if there are any indicators of unusual behavior in the curves, such as the 'kink' in Figure 6.2 and Figure 6.5, which hint at occurrence of classical flutter. By plotting the flap-wise and torsional deformation into the same figure, it can be seen which of the two shows the first signs of unusual behavior. If there is a hint of classical flutter, one moves on to the second step. Step 2 aims to determine if a phase difference is present between the flap-wise and torsional deformation. This can be checked by appropriately zooming in on the curves of the flap-wise and torsional deformation. Once this phase difference is established, the third step is considered. Here it is checked if the instability is a self-excitation of the flap-wise and torsional vibration and occurs within the time span associated with classical flutter. At the end of step three it can be concluded if the instability indeed is classical flutter. Step four starts with determining a first *rotor speed* value at which classical flutter is deemed to occur. Subsequently the overspeed loadcase is simulated with this fixed *rotor speed* and its associated *wind speed*. The results are analyzed using some key aspects. If the first *rotor speed* does not result in classical flutter, the *rotor speed* is increased by 0,25 RPM until the flutter speed is found. Vice versa if the first chosen *rotor speed* already yields classical flutter. As such it can be deduced with better accuracy what the flutter limit is. For the results of the simulation presented in section 6.1, a flutter limit of 19,87 [RPM] was established.

6.3 INFLUENCE OF CHANGING PITCH ANGLE AND TORSIONAL STIFFNESS ON THE FLUTTER LIMIT

This section presents the results for the separate effect of a changing *pitch angle* and *torsional stiffness* on the flutter limit. First the results for the changing *pitch angle* will be presented, accompanied by an elaboration. Consequently, the results for changing *torsional stiffness* will be provided and discussed. The results presented are for blade 1 and for the flap-wise displacement and torsional deformation. These deformations were pivotal in determining if classical flutter indeed occurs.

The *pitch angle* considered up to this point is equal to eight degrees. It is now altered to ten degrees, as such a comparison can be made between results of the two *pitch angles*. These results are presented in Figure 6.30 and Figure 6.31.

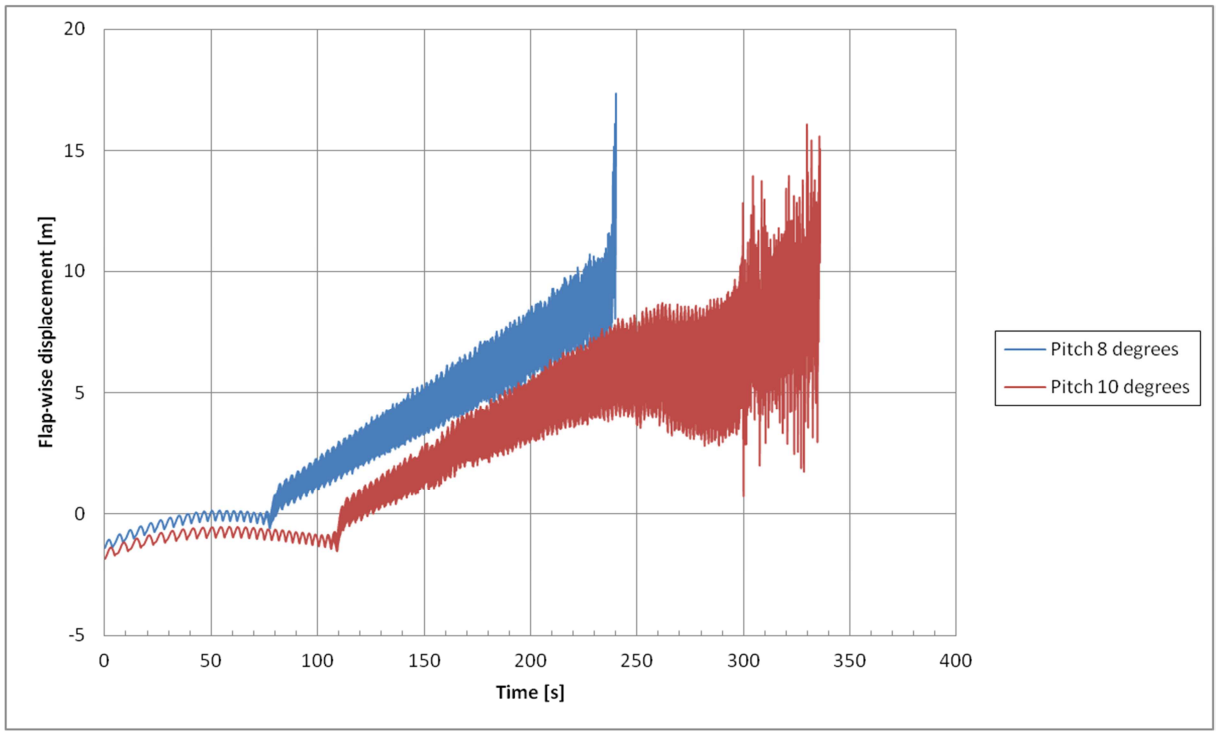

Figure 6.30: Flap-wise displacement for blade 1 as a result of the increasing wind speed in the LCPREP overspeed loadcase. The blue line is for a *pitch angle* equal to 8 degrees, while the red line is for a *pitch angle* equal to 10 degrees. This graph shows the effect of the increased pitch angle on the occurrence of the flutter limit associated with the 'kink'.

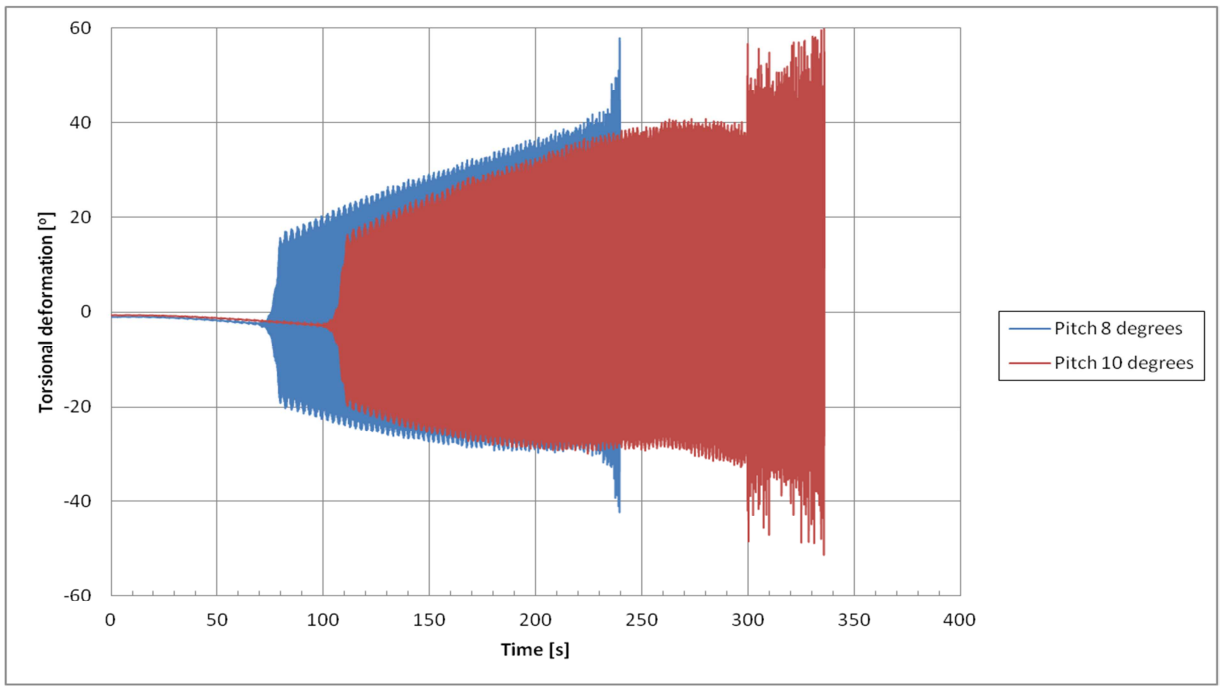

Figure 6.31: Torsional deformation for blade 1 as a result of the increasing wind speed in the LCPREP overspeed loadcase. The blue line is for a pitch angle equal to 8 degrees, while the red line is for a pitch angle equal to 10 degrees. This graph shows the effect of the increased pitch angle on the occurrence of the flutter limit associated with the rapid expansion.

From these two figures it is evident that increasing the pitch angle shifts both curves to the right and delays the occurrence of classical flutter. This could be deduced by executing the four steps mentioned in section 6.2, or by simply noting that both the 'kink' and expansion of the flap-wise and torsional deformation, respectively, occur at a time greater than was determined in section 6.2 for a *pitch angle* of eight degrees. To find the exact value of the flutter speed, the four steps of the method mention in the previous section should be followed.

Next the influence of the *torsional stiffness* is considered. The relevant plot is presented in Figure 6.32. In order to generate this plot, the second column in the torsion data table, see Table C.5, is multiplied with factors of 1,1 and 1,2 respectively. This creates two simulations with greater *torsional stiffness* values than the original simulation.

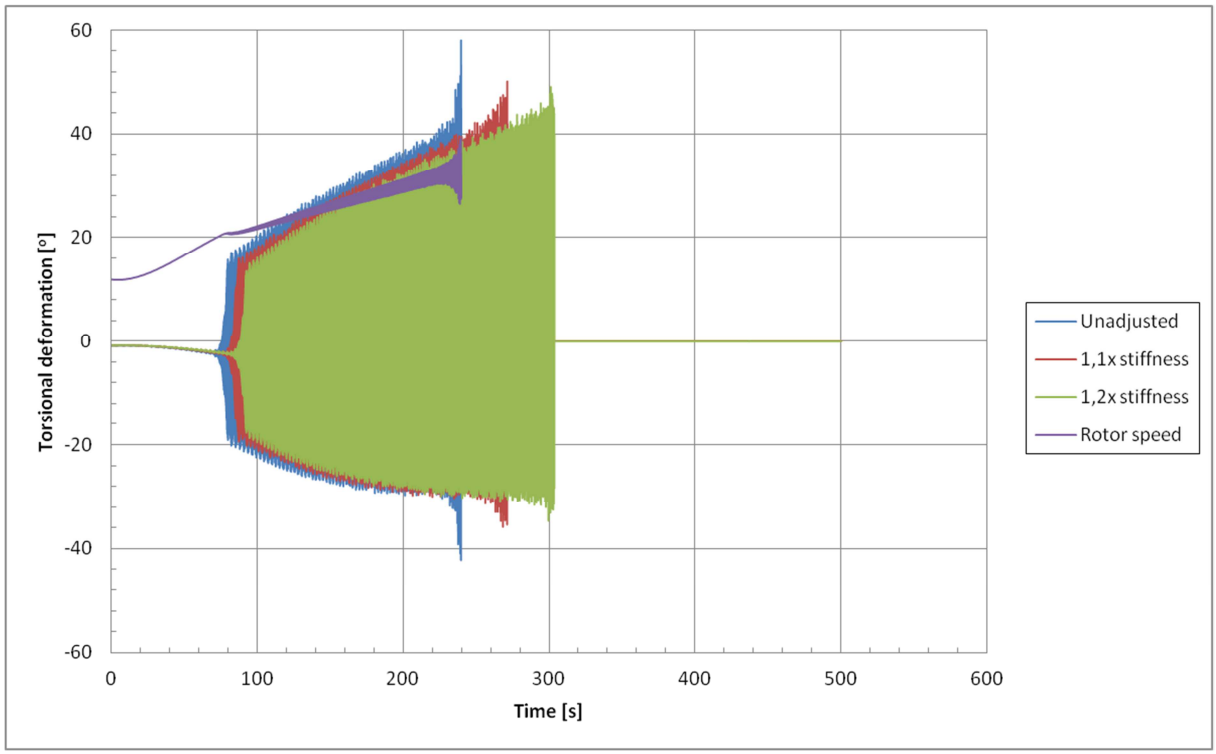

Figure 6.32: Torsional deformation, as a result of the increasing wind speed in the LCPREP overspeed loadcase, for changing torsional stiffness. Blue line is for unadjusted values, red is for multiplication of original torsional stiffness data with a factor of 1,1 and the green line is for multiplication with 1,2. The purple line indicates the rotor speed.

From this plot it is evident that increasing the *torsional stiffness* values over the entire blade span, results in a delay of the occurrence of classical flutter. This is evident because the rapid expansion of the amplitude of the torsional deformation occurs at a greater time in the simulation. Furthermore, this correlates with the results of the numerical example provided in Appendix A. Increasing the *torsional stiffness*, apparently increases the natural frequencies of the torsional mode shapes, resulting in classical flutter occurring at a later stage. This also correlates with the third flutter criterion mentioned in section 2.5. It should be noted that the rotor speed is plotted as well, because it contains the 'kink' and shows that when all simulations have the same *rotor speed* values, increasing the torsional blade stiffness postpones the occurrence of classical flutter.

Having performed both simulations, it is evident from Figure 6.30-Figure 6.32 that the best way to increase the flutter limit would be to increase the *pitch angle*. First of all, this is because the delay in the occurrence of classical flutter is larger for the changing *pitch angle* parameter. But another important aspect is, that it is also deemed the easiest option as changing the torsion data of the blade would mean redesigning the blade. However, it must be noted that the loss of generated power due to the increased pitch angle is not considered here.

6.4 DETERMINING THE NATURAL FREQUENCIES FOR CLASSICAL FLUTTER

In this section the results are presented for the natural frequencies associated with the flap-wise and torsional deformation respectively. The simulation considered is the second simulation from Table 6.1 indicated in green, as this simulation provided the flutter limit. The *pitch angle* used is eight degrees, when generating these results and the original torsion data table from Appendix C is used. It will be explained how the natural frequencies can be deduced, by using the built-in post-processor from FOCUS 6. This post-processor transforms the output signal from the time domain to the frequency domain via the Fast Fourier Transform (FFT). Using this post-processor a power spectral density (PSD) plot can be made of the signal of the output parameter. This PSD describes how the power of a signal or time series is distributed over the different frequencies. A natural frequency can be recognized in the PSD as it is represented by a 'spike' or narrow peak. Here a small amount of an input force can cause a very large response. This will be considered in the results. To this extent, Figure 6.33 and Figure 6.34 are presented.

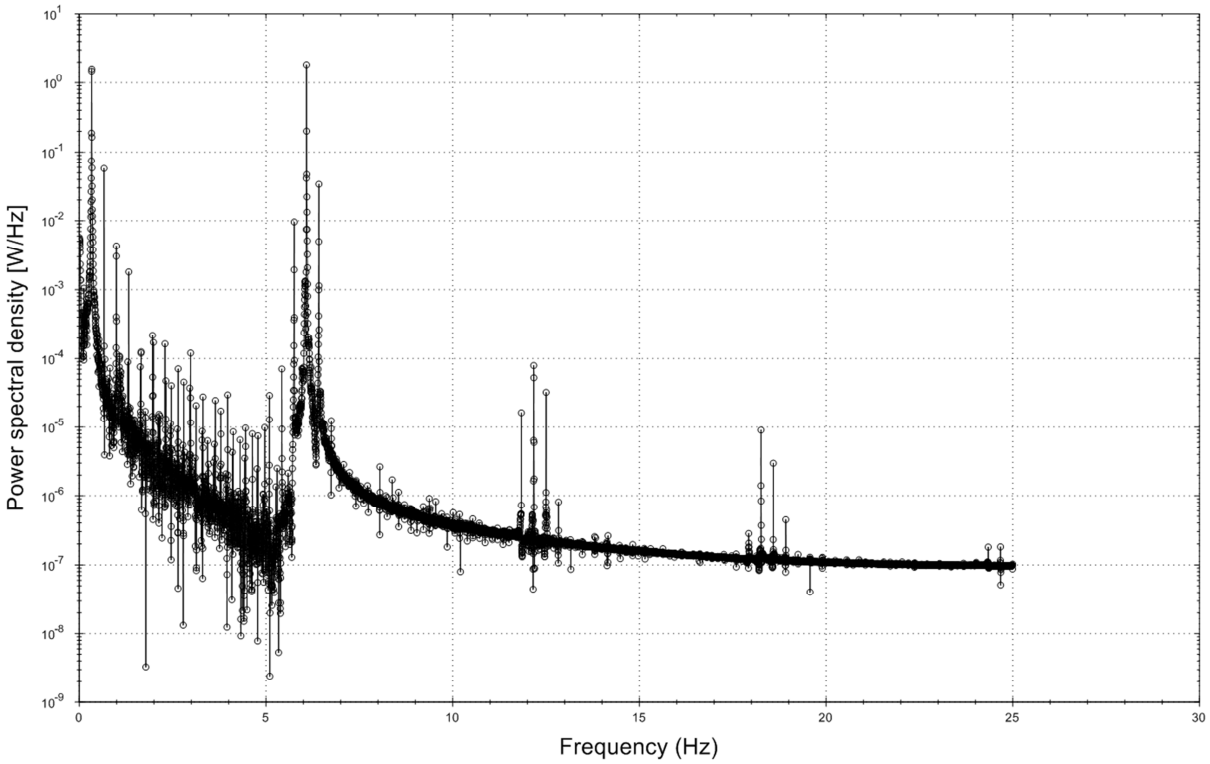

Figure 6.33: PSD for the flap-wise displacement of blade 1 for the simulation with *wind* and *rotor speed* of 13,12 [m/s] and 19,87 [RPM] respectively. A logarithmic scale is used as it yields a better perspective of the frequencies.

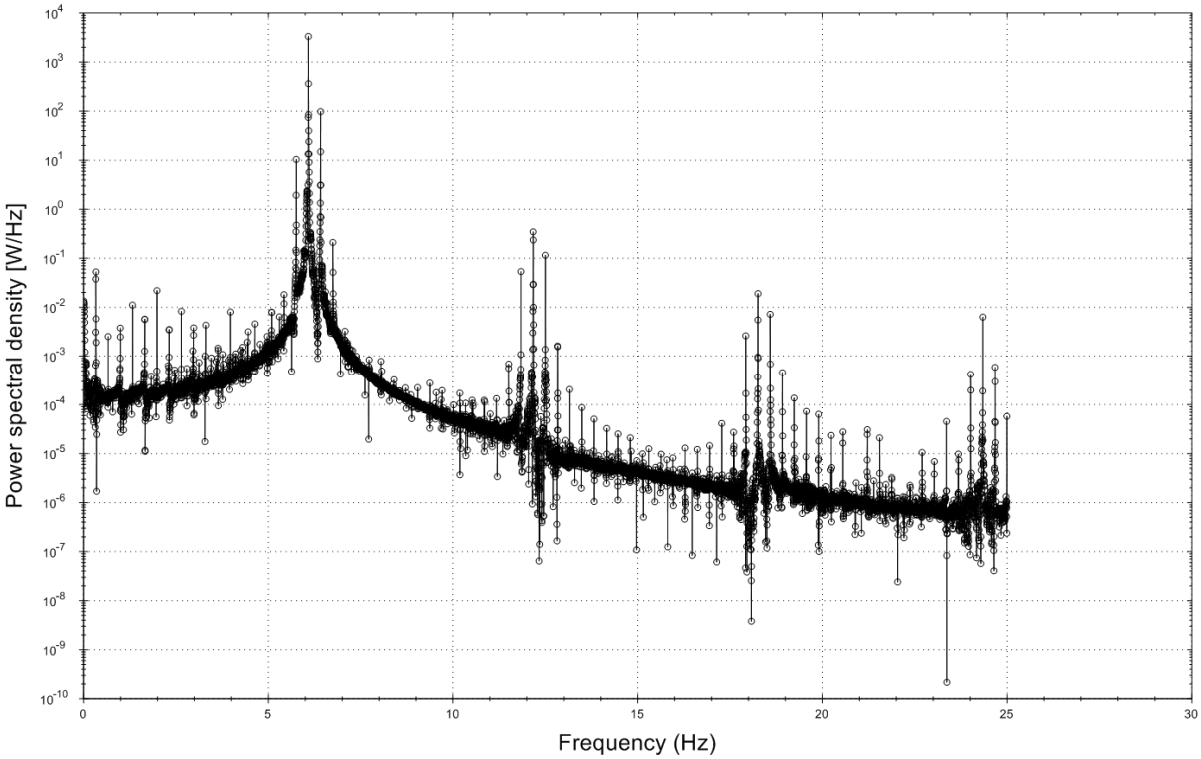

Figure 6.34: PSD for the torsional deformation of blade 1 for the simulation with *wind* and *rotor speed* of 13,12 [m/s] and 19,87 [RPM] respectively. A logarithmic scale is used as it yields a better perspective of the frequencies.

Considering Figure 6.33, a clear peak is present at around 6 Hz. As far as Figure 6.34 is concerned, there is also a clear peak present at the same frequency of 6 Hz. Since these two peaks occur at the same frequency and have a relative large response, it can be concluded that this is the frequency at which classical flutter occurs. This conclusion is substantiated when counting the number of peaks, and thus determining the frequency, in Figure 6.16 or Figure 6.22 and Figure 6.23 of either the flap-wise displacement or torsional deformation. This frequency is also approximately 6 Hz. For a classical flutter analysis, it thus are these frequencies of 6 Hz which are relevant in the PSD. This is in compliance with the theory from Chapter 2, where it was shown that when classical flutter occurs, the flap-wise and torsional natural frequencies approach each other. Hence the conclusion drawn from Figure 6.33 and Figure 6.34 is deemed viable. Such a PSD can be generated if one where interested in the frequency at which classical flutter occurs. Furthermore, it can be performed as an optional step after the fourth step of the method from section 6.2 is performed.

6.5 General Conclusions

The main conclusion that can be drawn is that it is possible to use PHATAS in the shell-program FOCUS 6 to analyze the occurrence of classical flutter, as well as determining a method for finding the flutter speed or limit.

The results for the analysis with the *pitch angle* of eight degrees hints at the occurrence of classical flutter. It is shown that this occurrence can be determined using a method comprising four steps. The first step of the method is to consider if there are any indicators of unusual behavior in the curves, such as the 'kink' in Figure 6.2 and Figure 6.5, which indicates the possible occurrence of classical flutter. Step 2 aims to determine if a phase difference is present between the flap-wise and torsional deformation. This is done by appropriately zooming in on the curves of the flap-wise and torsional deformation. The third step checks if the instability is a self-excitation of the flap-wise and torsional vibration and if it occurs within the time span associated with classical flutter. Consequently, step four consists of finding the flutter speed starting with a first estimation of the flutter limit based on the results obtained from the previous three steps. Performing the overspeed loadcase simulation with this fixed *rotor speed* value and its associated *wind speed*, shows whether the first estimation was correct or not. If the estimation proves to be too low the *rotor speed* is increased by 0,25 RPM. Vice versa if the first estimation is too high. This procedure is repeated until the flutter limit is found, which is established based on some key aspects. As such it can be deduced with better accuracy what the flutter limit is.

Next to this, the analysis with changing *pitch angles* and *torsional stiffness* values shows that increasing either of the parameters delays the occurrence of classical flutter. It is determined, between the two parameters, that changing the *pitch angle* value is the best way to delay classical flutter.

Finally, using the built-in post-processor in FOCUS 6 a FFT can be made of the signals of the output parameters, for the simulation at the time instance of the flutter limit, to produce the PSD. The PSD for the flap-wise displacement and torsional deformation shows a peak at the same frequency, which is determined to be the frequency at which classical flutter occurs.

6.6 Limitations of the Program

One of the limitations of the PHATAS program is that there is no direct output of a Campbell plot. As such, the behavior of the natural frequencies of the mode shapes, relevant to classical flutter, with increasing rotor speed cannot be viewed and analyzed directly.

Another limitation is that the program has no 3D plots of the mode shapes, which can be used to recognize the dominant mode shapes. This in contrast to BLADEMODE V.2.0.

Chapter 7 CONCLUSIONS AND RECOMMENDATIONS

This chapter concludes this report. First the conclusions are given followed by the recommendations.

7.1 CONCLUSIONS

The aim of this thesis is stated as:

"Provide a clear and efficient procedure
to analyze the flutter speed in case of classical flutter,
using BLADEMODE V.2.0 or PHATAS"

To meet this goal, three simulations are performed using BLADEMODE V.2.0. These simulations represent the possible variations for the type of classical flutter analysis with this program. The first simulation is executed such that it includes the generator damping effect on the modal frequencies in the classical flutter analysis, while for the second simulation this effect is omitted. Simulation three is executed such that the rotor speed is no longer solved from the aerodynamic torque, the generator torque-speed relation and the corresponding pitch angle but needs to be indicated manually. As each of these simulations has its own results, the classical flutter limit needs to be considered for each separate simulation. The focus is put on the approaching of the flap-wise and torsional natural frequencies as these are essential for classical flutter. This is because BLADEMODE V.2.0 inherently omits the relative phase between the deformation components and as such coupling between the flap-wise and torsional modes is not possible. Therefore attention is paid to the behavior of the relevant natural frequencies with increasing rotor speed. For each simulation a Campbell diagram is constructed which displays the natural frequencies of a vibration mode as a function of the rotor speed. All three simulations yield similar results. However, none of the Campbell diagrams, regardless of the simulation, shows behavior of the flap-wise and torsional natural frequencies which would be expected in case of classical flutter. Not only is there no coupling between the flap-wise and torsional modes, related to the an inherent property of BLADEMODE V.2.0, also there is no approaching visible between the natural frequencies of these two modes. This is not only in contrast to what is expected based on the theory of BLADEMODE V.2.0 and taking the centrifugal stiffening into account, but also with regard to the general classical flutter theory of how these natural frequencies should behave as a function of the rotor speed. Therefore it is concluded that in general BLADEMODE V.2.0 has an inherent inability to detect classical flutter and thus cannot be used to predict the flutter limit, or derive an efficient procedure to analyze this limit. This is substantiated by the mentioned fact that by performing the three simulations the possible variations for the type of classical flutter analysis are covered. Furthermore it is noted that although it is possible to differentiate between the absolute values of the relevant natural frequencies when comparing simulations, the impact of these differences on the flutter limit using BLADEMODE V.2.0 is inconclusive as it is not possible to determine this limit with the program.

The second program used to meet the aim of this thesis is PHATAS. This program uses the same reference wind turbine as provided for the BLADEMODE V.2.0 simulations. It are the results obtained with PHATAS which further substantiate the inability of BLADEMODE V.2.0 to detect classical flutter. Using PHATAS, the simulations performed in the time domain with the overspeed loadcase lead to the conclusion that it is possible to use PHATAS in the shell-program FOCUS 6 to analyze the occurrence of classical flutter, as well as determining a method for finding the flutter speed or limit. Based on the figures depicting the time history behavior of the flap-wise displacement and torsional deformation, it can be concluded that classical flutter occurs. This conclusion is substantiated by appropriately zooming in on the flap-wise displacement and torsional deformation plots and the rotor speed curve. Resulting from the

analysis of these curves, it is concluded that a four step method can be constructed to determine if classical flutter indeed occurs and how the associated flutter speed can be found. The first step of the method is to consider if there are any indicators of unusual behavior in the curves, which indicate the possible occurrence of classical flutter. Step two aims to determine if a phase difference is present between the flap-wise displacement and torsional deformation. This is done by appropriately zooming in on the curves of both deformations. The third step checks if the instability is a self-excitation of the flap-wise and torsional vibration and occurs within the time span associated with classical flutter. Consequently, step four consists of finding the flutter limit using a first estimation of this limit based on the results obtained in the previous steps. The overspeed loadcase is simulated with this fixed rotor speed and its associated wind speed. Using some key aspects it is established if classical flutter occurs. If the first estimation proves to be too low, the value of the rotor speed is increased by 0,25 RPM. Vice versa if the estimation is too high. Repeating this process until the flutter limit is found, increases the accuracy of the value of this limit.

The analysis with changing pitch angles and torsional stiffness values shows that increasing either of the parameters delays the occurrence of classical flutter. However, changing the pitch angle is considered the best way to do this. Furthermore, using the built-in post-processor in FOCUS 6 to produce a Fast Fourier Transform (FFT) of the flap-wise displacement and torsional deformation, for the simulation at the time instance of the flutter limit, a power spectral density (PSD) can be constructed. It is concluded that these PSD, one for the flap-wise and one for the torsional deformation, can be used to determine the natural frequency at which classical flutter occurs. This is substantiated by the fact that both the flap-wise and torsional deformation have relatively large peaks in their respective PSD at the same frequency.

7.2 RECOMMENDATIONS

With BLADEMODE V.2.0 the effect on the classical flutter limit, by changing the *torsion stiffness* values, is not analyzed as the *torsion data* is provided and classical flutter is not detected. Further investigation is needed here as significantly lowering the torsion stiffness values might yield better results, considering that this is one of the main flutter criteria. As such, it may be determined if the conclusion in this thesis that classical flutter cannot be detected with BLADEMODE V.2.0 remains valid under those conditions.

Simulations should be performed with other wind turbine models in BLADEMODE V.2.0 to compare with the work done and conclusions drawn in this thesis.

Validation of the results obtained with BLADEMODE V.2.0 should also be performed by executing the simulations in this thesis using the vortex wake model for the rotor aerodynamics.

Further investigation is required, using PHATAS, into what would be the best way to delay classical flutter. The conclusion that changing the *pitch angle* is better than changing the *torsion data* does not include the effect of the loss of power due to an increased *pitch angle*. It should be analyzed in detail, in order to better substantiate how to best delay classical flutter for the ART5 reference wind turbine used in this theses. To this extent, all flutter criteria should be considered.

Comparison of the results of other wind turbine models with the results obtained with PHATAS in this thesis is necessary. This can be done by performing the time domain simulations for different wind turbine models. It should be checked if applying the four step method to determine the presence of classical flutter and the associated flutter speed, is indeed correct.

REFERENCE LIST

1. Hulshoff, S.J., 2010. *AE4930 Aeroelasticity*. Aerodynamics Group Faculty of Aerospace Engineering, TU Delft.
2. Gandomi, A.H. et al., 2008. *Development in Mode Shape-Based Structural Fault Identification Technique*. *World Applied Sciences Journal*, 5(1), pp.29-38.
3. University of Connecticut. *3.6 Air Columns and Boundary Conditions*. [Online] Available at: http://www.phys.uconn.edu/~gibson/Notes/Section3_6/Sec3_6.htm [Accessed 20 November 2012].
4. Richardson, Mark H., 1997. *Is It a Mode Shape, or an Operating Deflection Shape?*. *Sound & Vibration Magazine*, 30th anniversary issue.
5. Dossing, O., Brüel & Kjaer, 1988. *Structural Testing, Part II: Modal Analysis and Simulation*.
6. Schwarz, B. & Richardson, M., 2006. *Using FEA Modes to Scale Experimental Mode Shapes*. International Modal Analysis Conf. (IMAC XXIV).
7. University of Texas. *2 Background Theory*. [Online] Available at: http://courses.ae.utexas.edu/ase463q/design_pages/spring03/wavelet/Webpage/Background.htm [Accessed 20 November 2012].
8. Lindenburg, C*. BLADEMODE V.2.0 Program for Rotor Blade Mode Analysis*. ECN-C--02-050 r7.
9. Van Rooij, R., 2001. *Terminology, Reference Systems and Conventions*. Duwind 2001.004.
10. Trudnowski, D. & Lemieux, D., 2002. *Independent Pitch Control using Rotor Position feedback for Wind Shear and Gravity Fatigue Reduction in a Wind Turbine*. American Control Conference. Anchorage, AK, 8-10 May 2002.
11. Politakis, G., Haans, W., Van Bussel, G.J.W., 2008. *Supression of Classical Flutter Using a 'Smart Blade'*. 46th AIAA Aerospace Sciences Meeting and Exhibit. Reno, Nevada. 7-10 January 2008.
12. Vatne, S.R., 2011. *Aeroelastic Instability and Flutter for a 10MW Wind Turbine*. Norwegian University of Science and Technology.
13. Hansen, M.H., 2007. *Aeroelastic Instability Problems for Wind Turbines*. *Wiley Interscience*, 10, pp.551-577.
14. Ferreira, C, 2011. *AE4W12 Rotor Aerodynamics, Lecture 8: Rotor Aerodynamics Vortex/Panel Methods*. Aerodynamics Group Faculty of Aerospace Engineering, TU Delft.
15. Mason, W.H., 1995. *AOE 4114 Applied Computational Aerodynamics Volume 1, Chapter 6: Aerodynamics of 3D Lifting Surfaces through Vortex Lattice Methods*. Virginia Polytechnic Institute and State University, Department of Aerospace and Ocean Engineering. [Online] Available at: http://www.dept.aoe.vt.edu/~mason/Mason_f/CAtxtChap6.pdf [Accessed 20 November 2012].
16. Katz, J. & Plotkin, A., 2001. *Low-speed Aerodynamics*. 2nd revised edition. Cambridge University Press.
17. Shyy, W. et al., 2010. *Recent progress in flapping wing aerodynamics and aeroelasticity. Progress in Aerospace Sciences 4G*, pp.284-327.
18. Bierbooms, W.A.A.M. & Rodenburg, R.V., 1992. *Flutter Analyse van Zijvanen voor Windmolens*. Mechanica & Constructies Group Faculty Civil Engineering, TU Delft.
19. National Aeronautics and Space Administration NASA*. Aerodynamic Center – ac*. [Online] Available at: http://www.grc.nasa.gov/WWW/K-12/airplane/ac.html [Accessed 20 November 2012].
20. Meng, F., 2011. *Aero-elastic Stability Analysis of Large-Scale Wind Turbines*. Dr. Delft University of Technology.
21. Zhicun Wang, 2004. *Time-Domain Simulations of Aerodynamic Forces on Three-Dimensional Configurations, Unstable Aeroelastic Responses, and Control by Neural Network Systems*. PhD. Virginia Polytechnic Institute.
22. Nayfeh, A.H. & Pai, F.P., 2004. *Linear and Nonlinear Structural Mechanics*. John Wiley & Sons, Inc.
23. Megson, T.H.G., 2013. *Aircraft Structures for Engineering Students*. 5th edition. Elsevier Ltd.
24. Weisshaar, T.A., 1995. *AAE 556 Aeroelasticity, Lecture 23: Representing motion with complex numbers and arithmetic*. Faculty Aeronautics & Astronautics, Purdue University.
25. Anderson, J. D. Jr., 2007. *Fundamentals of Aerodynamics*. 4th editon. Singapore: Mc Graw Hill.
26. G. Dimitriadis. *AERO0016 Introduction to Aeroelasticity, Lecture 01: Introduction – Equations of motion*. Université de Liege. [online] Available at: http://www.ltas-aea.ulg.ac.be/cms/uploads/Aeroelasticity01.pdf [Accessed 20 November 2012].
27. Duchesne, L.G., 1997. *Advanced Techniques for Flutter Clearance*. MSc. Massachusetts Institute of Technology.

28. University of Nebraska-Lincoln. *Mass moment of inertia*. [Online] Available at: http://emweb.unl.edu/negahban/em223/note19/note19.htm [Accessed 20 November 2012]
29. Academic Resource Center, 2012.*Workshop: Moment of Inertia*. Faculty Mechanical, Materials and Aerospace Engineering, Illinois Institute of Technology. [online] Available at: http://iit.edu/arc/workshops/pdfs/Moment_Inertia.pdf [Accessed 20 November 2012].
30. Hebert, C. et al., *Aerodynamic Flutter*. American Institute of Aeronautics and Astronautics. [online] Available at: http://www.cs.wright.edu/~jslater/SDTCOutreachWebsite/aerodynamic_flutter_banner.pdf [Accessed 20 November 2012].
31. Ziegler, H. *Principles of Structural Stability* (2nd edn). Birkhäuser Verlag: Basel, 1977.
32. Meirovitch, L. *Methods of Analytical Dynamics*. McGraw-Hill: New York, 1970.
33. Bisplinghoff, R.L., Ashley, H. & Halfman, R.L. *Aeroelasticity*. Dover Publications: New York, 1955.
34. Fung, Y.C. *An Introduction to the Theory of Aeroelasticity* (Dover edition, 1993). John Wiley & Sons, Inc.: New York, 1955.
35. Lanczos, C., 1970. *The Variational Principles of Mechanics*. 4th edition. University of Toronto Press.
36. Petersen, J.T., Thomsen, K. & Madsen, H.A. 1998. *Local Blade Whirl and Global Rotor Whirl Interaction*. Risø-R-1067(EN).
37. Holierhoek, J. G., Energy research Centre of the Netherlands ECN.
38. Bir, G.S., Wright, A.D. & Butterfield, C.P., 1996. *Stability Analysis of a Variable-Speed Wind Turbine*. NREL. [online] Available at: http://www.osti.gov/energycitations/servlets/purl/420360-9C2h1r/webviewable/420360.pdf Accessed 20 November 2012.
39. Skjoldan, P.F., 2011. *Aeroelastic modal dynamics of wind turbines including anisotropic effects*. PhD. Technical University of Denmark.
40. Hansen, M.H. Aeroelastic Stability Analysis of Wind Turbines Using an Eigenvalue Approach. *Wind Energy*, 2004, 7, pp.133–143.
41. Lindenburg, C., 2011. *Comparison of Phatas versions and the Wind Turbine module*. ECN. [online] Available at: http://www.ecn.nl/docs/library/report/2011/e11066.pdf Accessed 20 November 2012.
42. Lindenburg, K., Brood, R. & De Winkel, G., 2010. *FOCUS6 Workshop Aeroelastic Design I* (confidential). Wind Turbines and Constructions WMC.
43. Lindenburg, C., 2005. *PHATAS User's Manual*. ECN-I—05-005.
44. Lindenburg, C. & Snel, H., *Aero-elastic stability analysis tools for large wind turbine rotor blades*. Energy research Centre of the Netherlands ECN.
45. Snel, H., 1997. *Dynamic Stall Modelling: Some Results*. 11-th IEA Symposium on the Aerodynamics of Wind Turbines, ECN Petten.
46. Savenije, F.J. & Peeringa, J.M., 2004. *Aero-elastic simulation of offshore wind turbines in the frequency domain*. ECN-E–09-060.
47. Hulshoff, S.J., 2010. *AE4930 Aeroelasticity, Project 1*, 2010. Aerodynamics Group Faculty of Aerospace Engineering, TU Delft.
48. Robertson, D.G.E. et al., 2004. *Research Methods in Biomechanics*. Human Kinetics.
49. Germanischer Lloyd, 2010. *Rules and Guidelines IV Industrial Services, Part 1 Guideline for the Certification of Wind Turbines*. [online] Available at: http://cvi.se/uploads/pdf/Master%20Literature/Wind%20Turbine%20Technology/Guideline_for_the_Certification_of_Wind_Turbines_Edition_2010_R0_2_.pdf [Accessed 20 November 2012].

APPENDIX A NUMERICAL EXAMPLE TO FORM STABILITY PLOT

In order to create the stability plot, it is necessary to assume some values for the airfoil section and the surrounding airflow. The assumed values are presented in Table A.1. It should be noted that this section serves to provide a better understanding of the flutter limit and how it is influenced by the main flutter criteria. The values used to create this plot do not belong to an actual wind turbine blade.

Table A. 1: Wing and airflow properties used to construct stability plot.

Property	***Description***	***Value***	***Unit***
ρ	*Air density*	1,225	[kg/m^3]
m	*Mass per unit section*	100	[kg/m]
C_L'	*Lift curve gradient*	2π	[rad]
k_f	*Flap-wise stiffness*	1	[N/m/m]
$k_{t,1}$	*Torsional stiffness*	1000	[N · m/m]
a_{cg}	*Position of the CG relative to the EA*	-0,25-0,55	[-]
a_{AC}	*Position of the EA relative to the AC*	0,2	[-]
c	*Chord*	1	[m]
I_θ	*Mass moment of inertia about the EA*	100	[kg · m^2/m]

The values for ρ, m, k_f, $k_{t,1}$, a_{AC}, c and I_θ are based on Hulshoff [47]. The values are however adjusted such that the value for the reduced frequency remains lower than 0,1 and the example remains as simple as possible. By ensuring this, not only is the assumption of quasi-steady aerodynamics maintained, but also the omitting of the aerodynamic damping matrix $\boldsymbol{C}$ in the derivation of the flutter limit is validated.

The reason for the subscript used for the *torsional stiffness* will become clear in the subsequent analysis. Furthermore, the value of C_L' is based on a thin symmetric airfoil. In order to create the stability plot using the values from Table A.1, equation (2.45) needs to be rewritten, on the limit of this criterion, to formulate an expression for the critical relative speed $W_{0,n}$ or flutter speed.

$$W_{0,n} = \sqrt{\frac{2m\left(\omega_f^2 \frac{r_{CG}^2 + a_{CG}^2}{a_{AC}+a_{CG}} + \omega_{t,n}^2 \frac{r_{CG}^2}{a_{AC}+a_{CG}}\right)}{\rho C_L'}} \tag{A.1}$$

The reason for the subscript n is that, using the data in Table A.1, the natural torsional frequency $\omega_{t,1}$ is calculated. However, the stability plot will be made based on n frequencies, where n equals three, to be able to draw a conclusion regarding the effect of a changing natural torsional frequency and the flutter speed. As a result there will be three different W_0-lines in the plot.

The values for ω_f and $\omega_{t,1}$ are determined using equations (2.23) and (2.28) [1].

$$\omega_f = \sqrt{\frac{k_f}{m}} = \sqrt{\frac{1}{100}} = 0{,}1\ [Hz] \tag{A.2}$$

$$\omega_{t,1} = \sqrt{\frac{k_{t,1}}{I_\theta}} = \sqrt{\frac{1000}{100}} = 3{,}16\ [Hz] \tag{A.3}$$

Based on equation (A.3), the values for the other two natural torsional frequencies are chosen arbitrarily and $k_{t,2}$ and $k_{t,3}$ can then be calculated.

$$\omega_{t,2} = \omega_{t,1} + 0{,}5 = 3{,}66\ [Hz] \tag{A.4}$$

$$\omega_{t,3} = \omega_{t,2} + 0{,}5 = 4{,}16\ [Hz] \tag{A.5}$$

$$k_{t,2} = \omega_{t,2}^2 I_\theta = 3{,}66^2 \cdot 100 = 1{,}3 \cdot 10^4\ \ [N\,m/m] \tag{A.6}$$

$$k_{t,3} = \omega_{t,3}^2 I_\theta = 4{,}16^2 \cdot 100 = 1{,}7 \cdot 10^4 \ [N\,m/m] \tag{A.7}$$

It should be noted that in reality I_θ and thus r_{CG} and $\omega_{t,1}$ are functions of a_{CG}. For simplicity reasons they are assumed to be constant, although a_{CG} is changing [48]. This was already mentioned in section 2.4, when presenting equation (2.28). Therefore there is an inaccuracy of the critical relative speed, but the interaction between the main flutter criteria can still be illustrated. Keeping this in mind, equation (A.3) is similar to equation (2.28). Rewriting the latter expression in terms of r_{CG}, yields equation (A.8).

$$r_{CG} = \sqrt{\frac{k_{t,1}}{mc^2\omega_{t,1}^2}} = \sqrt{\frac{1000}{100 \cdot 1^2 \cdot 3{,}16^2}} = 1\ [-] \tag{A.8}$$

Note that in equation (A.8) r_{CG} has no units as it represents the normalized radius of gyration. Furthermore, although the values for k_t and ω_t change, the ratio $k_{t,n}/\omega_{t,n}^2$ in equation (A.8) remains the same for n=1, 2, 3.

Now that the normalized radius of gyration has been determined, one can check whether the value chosen for I_θ in Table A.1 indeed equals $mc^2 r_{CG}^2$, as indicated in equation (2.28).

$$I_\theta = mc^2 r_{CG}^2 = 100 \cdot 1^2 \cdot 1^2 = 100\ [\text{kg} \cdot \tfrac{\text{m2}}{\text{m}}] \tag{A.9}$$

Finally, in the stability plot the location of the CG will be expressed with respect to the leading edge. The values for a_{CG} indicated in Table A.1 are based on Figure 2.8. Since a_{CG} is determined with respect to the elastic axis, which is located at 45% chord, the maximum value for a_{CG} can only be 0,55. This is because that would place the CG at the trailing edge, or 100% chord location. If a_{CG} is in front of the EA, it obtains a negative value. Hence, based on the condition stated in equation (2.45), the minimum value for a_{CG} is at the AC which is -0,2.

Having determined all the relevant parameters, the stability plot in Figure A.1 can be created.

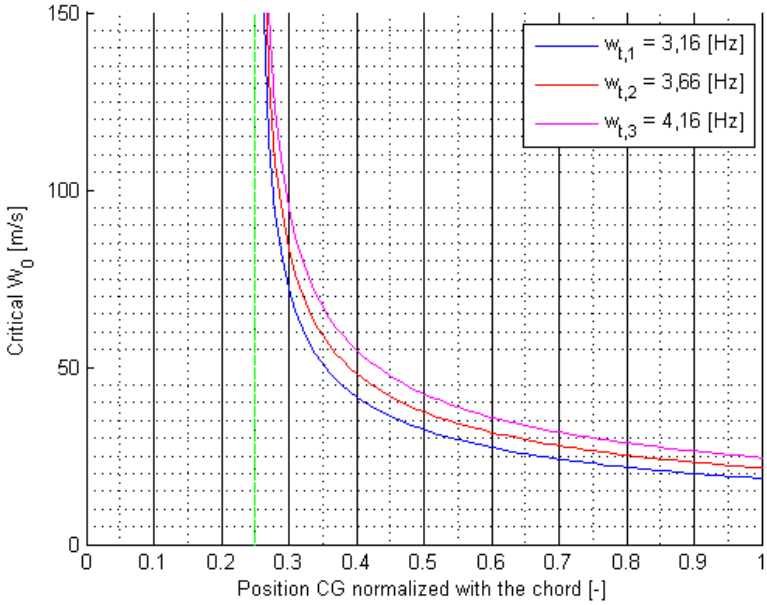

Figure A.1: Stability plot showing the critical relative speed as a function of the chord-wise position of the CG, for indicated natural torsional frequencies.

In the figure there is a vertical asymptote, indicated with the green line, at the 25% chord location, which is the AC location. As is clear from the figure, the values for the critical relative speed are indeed high, thereby complying with the second main flutter criterion. From Figure

A.1 it is also clear that for decreasing natural *torsional stiffness*, the flutter limit decreases. This complies with the third main flutter criterion stated at the beginning of this section. Next to this, as the location of the CG moves aft, the flutter speed decreases. This complies with the fourth main flutter criterion. The first main flutter criterion stated in Section 2.5, must always be met if classical flutter is to occur.

Figure A.1 can also be used to consider whether the coefficient of the polynomial, stated in equation (2.40) indeed becomes negative at the flutter speed indicated in the plot and thus yields an unstable solution. Using the values from the stability plot associated with $\omega_{t,2}$, the value for the position of the CG is chosen to be at 0,7. This correlates with an a_{CG} equal to 0,25. At the position of the CG of 0,7 a critical W_0 of approximately 28 m/s is read from the graph. Now considering the limit of the flutter criterion stated in equation (2.45), which is similar to the one in equation (2.40), the speed at which the coefficient of the polynomial becomes negative can be deduced.

$$0 < \omega_f^2 \frac{r_{CG}^2 + a_{CG}^2}{a_{AC} + a_{CG}} + \omega_{t,2}^2 \frac{r_{CG}^2}{a_{AC} + a_{CG}} - \frac{\rho}{2m} W_0^2 C_L' \tag{A.10}$$

Constructing a plot of the value of the coefficient on the RHS of equation (A.10) as function of the critical relative speed, it can be illustrated at which speed the coefficient switches sign and becomes negative. The values for ρ, m, C_L', and a_{AC} are indicated in Table A.1. The value for r_{CG} is presented in equation (A.8), while ω_f is given in equation (A.2).

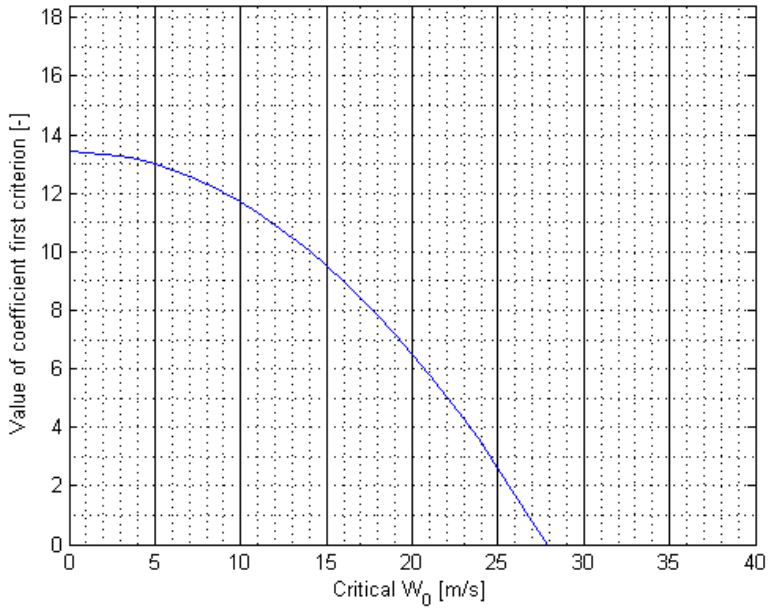

Figure A.2: Value of the coefficient of the flutter limit criterion.

It can be seen in Figure A.2 that the critical relative speed at which the coefficient becomes negative is approximately 28 m/s, which corresponds to the value deduced from Figure A.1 for the line of $\omega_{t,2}$ and a_{CG}=0,25.

As a final check, the value of the reduced frequency is plotted against the critical relative speed to see if it is indeed below 0,1 for all three natural torsional frequencies.

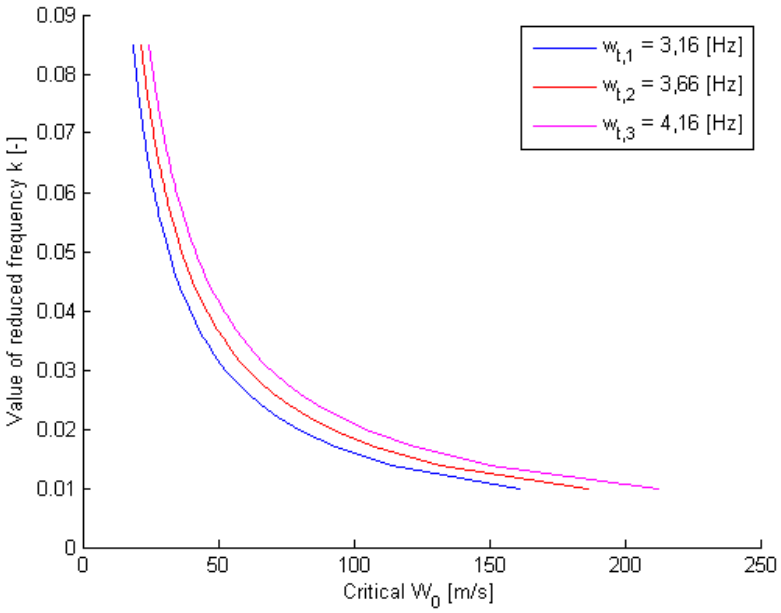

Figure A.3: Value of the reduced frequency *k* calculated for each torsional frequency.

The values are indeed well below 0,1. Therefore, based on Figure A.3, the assumptions and simplifications based on the condition that $k<0,1$ are justified.

APPENDIX B REFERENCE FRAMES

In this appendix the reference frames mentioned in Chapter 2 are illustrated again for clarity reasons in Figure B1. Although the labeling of the axes might have different symbols, the x-y-z axes are in the same direction as in Chapter 2. Furthermore it should be noted that the only inertial reference frame in Figure B1 is the ground-fixed reference frame.

Blade root reference system

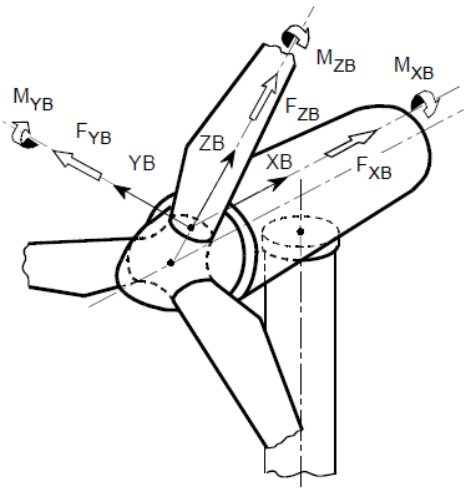

XB in direction of the rotor axis
ZB radially
YB so that XB, YB, ZB rotate clockwise

Local blade reference system

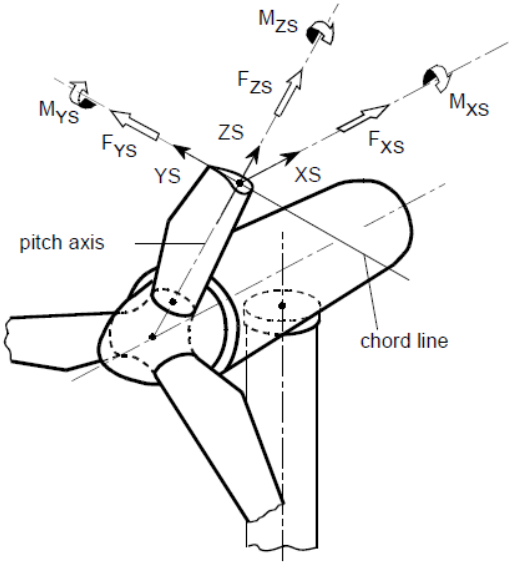

YS in direction of the chord, orientated to blade trailing edge
ZS in direction of the blade pitch axis
XS perpendicular to the chord, so that XS, YS, ZS rotate clockwise

Rotating rotor reference frame

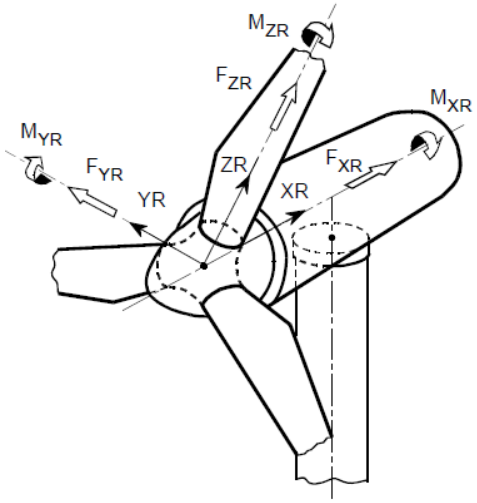

XR in direction of the rotor axis
ZR radially, orientated to rotor blade 1 and perpendicular to XR
YR perpendicular to XR, so that XR, YR, ZR rotate clockwise

Ground-fixed reference frame

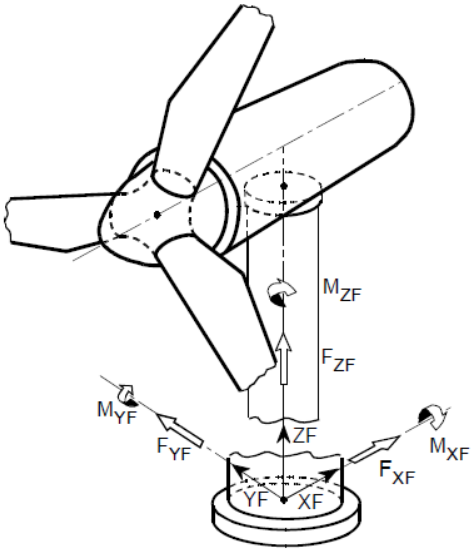

XF horizontal
ZF vertically upwards in direction of the tower axis
YF horizontally sideways, so that XF, YF, ZF rotate clockwise

Figure B.1: Reference frames used in the analysis [49]. The description of the axis is provided in the figures.

APPENDIX C ART5 INPUT FILE BLADEMODE V.2.0

```
nr_modes          0          # Number of modes that are required.
blade_torsion     OFF        # If 'ON' torsional deformation is included.
deformed_state    OFF        # Solve the deformed state with aerodynamics.
aerodynamics      OFF        # For aerodynamic stiffness and damping.
vortex_wake       OFF        # Solve quasi-steady state with vortex-wake model.
air_density                  1.225
#
dynamic_stall     1          # Refers to the first-order dynamic stall model.
amplitude         10.0       # Damping from the work for finite amplitude
amplitude         0.0        # Damping from linearized aerodynamic expressions.
ellipse_ratio     0.0        # Modifies motions from translations to loops.
#
wind_velocity     8.0
#
blade_span        62.7       # [m] Length of the blade.
root_radius       1.5        # [m] Radius of hub.
cone_angle        -2.5       # [deg]
tilt_angle        5.0        # [deg]
#
pitch_angle       0.0        # [deg]
rotational_speed  12.10      # [rpm] The nominal speed.
rotational_speed  11.0       # [rpm] Below nominal speed.
hinge_stiffness   2.E+30     # [Nm/rad] Large value indicates 'rigid'.
pitch_stiffness   2.E+30     # [Nm/rad] Large value indicates 'rigid'.
#
flap_pre_bend     -2.05      # [m] Undeformed bending deformation at tip.
lag_pre_bend      0.0
pre_bend_begin    17.9       # [m] With conservation of the tip radius.
pre_bend_end      53.7       # [m] With conservation of the tip radius.
#  Following are properties of the turbine, which are only
#  relevant for rotor shaft torsion and fore-aft tower bending.
nr_blades         3          # number of rotor blades.
#
#  For drive-train dynamics.
variable_speed    ON                 # If 'ON', then collective lead-lag modes.
hub_inertia       116000.0           # [kg*m^2]
drive_inertia     5000.0E+3          # [kg*m^2] All components behind the shaft.
shaft_stiffness   8.7E+8             # [Nm/rad] Stiffness of main shaft.
#shaft_stiffness  2.E+30             # [Nm/rad] Large value indicates 'rigid'
#
#  Conversion losses were added with 'CalcLoss';  C. Lindenburg, Nov. 2004.
```

Table C.1: Generator Curve Table

Speed [rpm]	*Torque [Nm]*	*Loss [Nm]*	*Pitch [deg]*
5.4	0.0	0.0	1.5,
5.87	0.77403E+6	21672.8	1.0,
7.2	1,16E+10	32538.7	1.0,
8.53	1,63E+11	45592.6	1.0,
10.52	2,44E+11	68182	1.0,
11.0	2,96E+12	82935	1.0,
11.9	3,95E+12	110596	4.0,
12.0	4,06E+11	113670	4.0,
12.1	4,06E+11	113670	4.0,
12.6	3,90E+12	109159	60.0,
13.1	3,75E+11	104993	70.0,
15.1	3,25E+12	91086.6	80.0

For fore-aft tower motion.
hub_mass 57000.0 # [kg]
tower_top_mass 240000.0 # [kg] Nacelle mass.
tower_top_stiffness 327607.0 # [N/m] Stiffness for the first fore-aft mode.
tower_stiffness 940468.35 # [N/m] Stiffness for the first fore-aft mode.
#tower_stiffness 2.E+30 # [N/m] Large value indicates 'rigid'.
#
3D_correction ON
#
#
twist_related ON # If ON the blade properties are w.r.t. twist.
In the following tables X is perpendicular to the chord
and Y is to the trailing edge.
#
#
Following table contains the blade mass properties.

Table C.2: Blade mass properties

Span [m]	*Mass [kg/m]*	X_{CG} *[m]*	Y_{CG} *[m]*	*rdelXX [m^2]*	*rdelYY [m^2]*	*rdelXY [m^2]*
0	698	0	0,0002	1,5	1,5	0
1,2	798	0	-0,0245	1	1,5	0
3,2	761	0	0,0442	0	1,48109	0
5,2	468	0	0,0672	0	1,42206	0
14,2	363	0	0,273	0	1,33703	0
24,2	322	0	0,1969	0	0,992414	0
34,2	246	0	0,1501	0	0,677988	0
40,2	183	0	0,1818	0	0,551009	0
48,2	133	0	0,2308	0	0,475962	0
60,7	39	0	0,0545	0	0,096721	0
62,6	2	0	0,0268	0	0,011772	0

#
Following table contains the geometric blade data.

Table C.3: Geometric data

Span [m]	*Chord [m]*	*Twist [deg]*	X_{AC} *[m]*	Y_{AC} *[m]*
0	3,5	13,4	0	-0,875
1	3,5	13,4	0	-0,875
10,7	4,6085	13,4	0	-0,6095
15	4,6694	8,346	0	-0,5791
18,69	4,4883	7,393	0	-0,5554
44	2,4635	-0,1	0	-0,3695
50	2,1	-1,2	0	-0,3242
55	1,86	-1,883	0	-0,287
58	1,75	-1,5	0	-0,253
59,6	1,7	-1	0	-0,202
61	1,5	-0,3	0	-0,137
62,7	0,35	0,5	0	-0,044

Following table contains the bending stiffness and related properties.

Table C.4: Bending data

Span [m]	EI_{flat} [N*m^2]	EI_{edge} [N*m^2]	EI_{cross} [N*m^2]	*Sh_XX* [1/N]	*Sh_YY* [1/N]	*Sh_XY* [1/N]	X_{EA} [m]	Y_{EA} [m]
0	1,76E+10	1,76E+10	-2,29E+03	0,00E+00	0,00E+00	0,00E+00	0	0
3,2	1,45E+10	1,96E+10	9,49E+07	0,00E+00	0,00E+00	0,00E+00	0	0
5,2	6,70E+09	1,00E+10	8,27E+07	0,00E+00	0,00E+00	0,00E+00	0	0
14,2	2,37E+09	4,80E+09	6,87E+07	0,00E+00	0,00E+00	0,00E+00	0	0
24,2	1,24E+09	3,58E+09	1,14E+08	0,00E+00	0,00E+00	0,00E+00	0	0
34,2	3,82E+08	2,24E+09	9,11E+06	0,00E+00	0,00E+00	0,00E+00	0	0
42,2	1,21E+08	1,12E+09	-1,32E+07	0,00E+00	0,00E+00	0,00E+00	0	0
57,7	2,33E+07	2,52E+08	-3,02E+06	0,00E+00	0,00E+00	0,00E+00	0	0
62,6	1,87E+06	5,06E+07	2,86E+03	0,00E+00	0,00E+00	0,00E+00	0	0

Following table contains the torsion related properties. The latter 3 columns contain the 'Karaolis' constants.

Table C.5: Torsion data

Span [m]	GJ_t [N*m^2]	X_{shc} [m]	Y_{shc} [m]	H_{41} [rad/N]	H_{42} [rad/Nm]	H_{43} [rad/Nm]
0.200	7,21E+9	0.0	-0.2587	0.0	0.0	0.0,
3.200	5,94E+9	0.0	-0.2082	0.0	0.0	0.0,
5.200	3,27E+9	0.0	-0.1819	0.0	0.0	0.0,
14.200	5,94E+8	0.0	-0.3685	0.0	0.0	0.0,
24.200	3,05E+8	0.0	-0.3459	0.0	0.0	0.0,
28.200	2,08E+8	0.0	-0.3289	0.0	0.0	0.0,
30.200	1,37E+8	0.0	-0.2931	0.0	0.0	0.0,
50.200	1,46E+7	0.0	-0.1154	0.0	0.0	0.0,
57.700	7,70E+6	0.0	-0.0640	0.0	0.0	0.0,
60.700	2,12E+6	0.0	-0.0335	0.0	0.0	0.0

APPENDIX D BLADEMODE V.2.0 INPUT FILE SIMULATION 1

gravity	9.81
nr_modes	9
variable_speed	ON
drive_inertia	5000.0E+03
root_loss	OFF

Table D.1: Generator curve table.

0	0	0	8	,
5.4	0	0	8	,
5.87	7.74E+05	21672.8	8	,
7.2	1.16E+06	32538.7	8	,
8.53	1.63E+06	45592.6	8	,
10.52	2.44E+06	68182	8	,
11	2.96E+06	82935	8	,
11.9	3.95E+06	110596	8	,
12	4.06E+06	113670	8	,
12.1	4.06E+06	113670	8	,
12.6	3.90E+06	109159	8	,
13.1	3.75E+06	104993	8	,
15.1	3.25E+06	91086.6	8	

deformed_state	ON
solve_speed	ON
aerodynamics	ON
blade_torsion	ON
generator_damp	ON
vortex_wake	OFF
air_density	1.225
dynamic_stall	1
amplitude	0
wind_velocity	8.0
blade_span	62.7
azimuth	90
ellipse_ratio	0
yaw_angle	0.0
3D_correction	ON
twist_related	ON

Table D.2: Bending data.

0	1,76E+10	1,76E+10	-2290	0.00E+00	0.00E+00	0.00E+00	0	0
3.2	1,45E+10	1,96E+10	94900000	0.00E+00	0.00E+00	0.00E+00	0	0
5.2	6,7E+09	1E+10	82700000	0.00E+00	0.00E+00	0.00E+00	0	0
14.2	2,37E+09	4,8E+09	68700000	0.00E+00	0.00E+00	0.00E+00	0	0
24.2	1,24E+09	3,58E+09	1,14E+08	0.00E+00	0.00E+00	0.00E+00	0	0
34.2	3,82E+08	2,24E+09	9110000	0.00E+00	0.00E+00	0.00E+00	0	0
42.2	1,21E+08	1,12E+09	-1,3E+07	0.00E+00	0.00E+00	0.00E+00	0	0
57.7	23300000	2,52E+08	-3020000	0.00E+00	0.00E+00	0.00E+00	0	0
62.6	1870000	50600000	2860	0.00E+00	0.00E+00	0.00E+00	0	0

Table D.3: Torsion data.

0.200	7,21E+12	0.0	-0.2587	0.0	0.0	0.0,
3.200	5,94E+12	0.0	-0.2082	0.0	0.0	0.0,
5.200	3,27E+12	0.0	-0.1819	0.0	0.0	0.0,
14.200	5,94E+11	0.0	-0.3685	0.0	0.0	0.0,
24.200	3,05E+11	0.0	-0.3459	0.0	0.0	0.0,
28.200	2,08E+11	0.0	-0.3289	0.0	0.0	0.0,
30.200	1,37E+11	0.0	-0.2931	0.0	0.0	0.0,
50.200	1,46E+10	0.0	-0.1154	0.0	0.0	0.0,
57.700	7,70E+10	0.0	-0.0640	0.0	0.0	0.0,
60.700	2,12E+10	0.0	-0.0335	0.0	0.0	0.0

Table D.4: Mass data.

0	698.00	0	0.0002	1.5	1.5	0
1.2	798.00	0	-0.0245	1	1.5	0
3.2	761.00	0	0.0442	0	148.109	0
5.2	468.00	0	0.0672	0	142.206	0
14.2	363.00	0	0.273	0	133.703	0
24.2	322.00	0	0.1969	0	0.992414	0
34.2	246.00	0	0.1501	0	0.677988	0
40.2	183.00	0	0.1818	0	0.551009	0
48.2	133.00	0	0.2308	0	0.475962	0
60.7	39.00	0	0.0545	0	0.096721	0
62.6	2.00	0	0.0268	0	0.0117722	0

Table D.5: Geometric data.

0	3.5	13.4	0	-0.875	,
1	3.5	13.4	0	-0.875	,
10.7	4,61E+04	13.4	0	-0.6095	,
15	4,67E+04	8.346	0	-0.5791	,
18.69	4,49E+04	7.393	0	-0.5554	,
44	2,46E+04	-0.1	0	-0.3695	,
50	2.1	-1.2	0	-0.3242	,
55	1.86	-1.883	0	-0.287	,
58	1.75	-1.5	0	-0.253	,
59.6	1.7	-1	0	-0.202	,
61	1.5	-0.3	0	-0.137	,
62.7	0.35	0.5	0	-0.044	

wind_series
1 ,
2 ,
....
....
60

root_radius	1.5
cone_angle	-2.5
tilt_angle	5
pitch_angle	8
pitch_error	0
pitch_inertia	0
pitch_stiffness	2.E+30
rotational_speed	12.1
tip_mass	0
tip_stat_moment	0
tip_bend_inertia	0
tip_tors_inertia	0
hinge_stiffness	2e+30
flap_pre_bend	-2.05
lag_pre_bend	0.0
pre_bend_begin	17.9
pre_bend_end	53.7
nr_blades	3
shaft_stiffness	8.7E+8
hub_mass	57000
hub_inertia	116000
tower_stiffness	940468.35
tower_top_mass	240000

Table D.6: Airfoil table.

0	cylinder.prf	,
8.35	DU40_A17	,
13.2	DU35_A17	,
18.7	DU30_A17	,
25	DU25_A17	,
32.42	NACA63421	,
40.67	NACA63418	

APPENDIX E ART5 INPUT FILE PHATAS

MENU	menu_param
Screen_option	OFF
<	
MENU	job_param
model_identif	ART5_compact
time_history_flag	OFF
message_file	ART5_c.log
model_file	ART5_c.mdl
output_file	ART5_c.pht
comment_mark	''
output_level	2
time_increment	0,020000
<	
SUBMENU	time_history
maximum_time	640,00
skip_time	40,00
table_increment	2
datafile_flag	OFF
datafile_name	Loadfiles\ART5_c.tbh
data_increment	2

Table E.1: Output table.

2	0,0
5	0,0
7	0,0
8	0,0
12	0,0
21	0,0
21	107,5
22	107,5
24	107,5
25	107,5
88	0,0
89	0,0
91	0,0
104	0,0
112	10,0
112	20,0
112	30,0
112	40,0
999	0,0

Table E.2: Pitch angle.

Blade number [-]	*Pitch angle [deg]*
1	1,00
2	0,70
3	1,30

rotor_speed	55,000
rotor_azimuth	0,0000
teeter_angle	0,0000
teeter_velocity	0,0000
yaw_angle	0,0000
<	
SUBMENU	turbine_coeff
delta_lambda	0,5000
lambda_min	70,000
nr_lambda	6

Table E.3: Pitch series [deg].

0,000
0,500
1,000
1,500
2,000
3,000
-180,000
-180,000
-180,000
-180,000

SUBMENU	control
brake_time	99000
generator_cut_off	99000
brake_overspeed	14,5
brake_torque	0
brake_delay_time	0,1
brake_ramp_time	0,05
brake_pitch_rate	3
control_increment	0,02
control_type	2
controller_target	12,1
fuzzy_pitch_rate	4
fuzzy_control_limit	1,40E+01
average_time	0,8
proportional_gain	3,00E-01
gain_scheduling	0,16
differential_gain	2,00E+00

pitch_time_lag	0,1
threshold_value	0,5
control_pitch_rate	5
max_pitch_acc	6
pitch_error	0,3
generator_emergency	16
peak_shave_pitch	4,5
peak_shave_begin	11
peak_shave_end	11,8
wait_time	30
failure_type	0
start_pitch_rate	-1
start_speed	6
max_pitch_error	1,5
pulses_per_rev	8192
pulse_ring_eccentr	0,0005
<	
MENU	geometry
tilt_angle	5
rotor_distance	5,02
hub_location	2,4
rotor_eccentricity	0
cone_angle	-2,5
blade_root_radius	1,5
nr_blades	3
blade_span	62,7
blade_elements	23
pitch_location	0
feather_axis	0
radial_motion	0
hub_mass	57000
hub_inertia	116000
hub_static_moment	0
nacelle_mass	240000
static_moment_x	460000
static_moment_z	420000
rolling_inertia	1,00E+06
tilting_inertia	2,90E+06
yawing_inertia	2,60E+06
cross_inertia	0,00E+00
nacelle_side_drag	108
nacelle_front_drag	36
<	
MENU	configuration
tower_input	tower108m.inp
free_yawing	OFF

gearbox_support	OFF
shaft_torsion	OFF
teeter_flag	OFF
hinge_flag	OFF
pitch_flag	OFF
lagging_flag	ON
flapping_flag	ON
blade_torsion	ON
<	
SUBMENU	yaw_data
yaw_start_time	99000
yaw_rate	0,3
yaw_ramp_time	10
yaw_repeat_time	100
yaw_friction	0,00E+00
yaw_damping	0
yawdrive_inertia	0,00E+00
yaw_time_lag	3
<	
SUBMENU	generator_data
generator_model	5
rated_rotorspeed	12,1
rated_power	5000000
generator_slope	0,02
maximum_torque	4,60E+04
tau_gen	0

Table E.4: Generator curve table.

Rotor speed divided by nominal speed [-]	*Torque at fast shaft [Nm]*	*Transmission loss w.r.t. fast shaft [Nm]*
0	0	0,0000
0,4463	0	0,0000
0,4851	7979,69	223,4313
0,595	11980,38	335,4505
0,705	16786,66	470,0265
0,8694	25103,82	702,9070
0,9917	41851,91	1171,8534
1	41851,91	1171,8534
1,0826	38657,11	1082,3989
1,1653	35915,46	1005,6330
1,3306	31453,92	880,7097
0	0	0

gear_ratio	97
constant_loss	0
proportional_loss	0,028
slow_shaft_inertia	0,00E+00

fast_shaft_inertia	5,34E+02
shaft_stiffness	8,68E+08
gearbox_inertia	0,00E+00
support_stiffness	9,00E+09
support_damping	0
<	
SUBMENU	teeter_data
delta_3_angle	0
teeter_offset	0

Table E.5: Teeter spring.

Teeter angles [deg]	*Restoring teeter spring moments [Nm]*
1,0000	0,0000
0,0000	0,0000

teeter_friction	0
teeter_viscosity	0
<	
SUBMENU	hinge_data
min_flap_angle	-90
max_flap_angle	90
hinge_stiffness	0
bumper_stiffness	0
hinge_damping	0
<	
SUBMENU	pitch_data
coupled_pitch	OFF
min_pitch_angle	1
max_pitch_angle	90
pitch_stiffness	9E+09
pre_stress_moment	0
pitch_damping	0
pitch_friction	0
<	
MENU	profiles
3D_correction	ON
dynamic_stall	1
hup1	0
hup2	0
hup3	0
<	
MENU	blade_data
flap_pre_bend	-2,05
lag_pre_bend	0
pre_bend_begin	17,9
pre_bend_end	53,7

Table E.6: Blade geometry.

Spanwise coordinate [m]	*Chord [m]*	*y-coordinate [m] (lag-wise) of the 25% chord location*
0,0000	3,5000	-0,8750
1,0000	3,5000	-0,8750
10,7000	4,6085	-0,6095
15,0000	4,6694	-0,5791
18,6900	4,4883	-0,5554
44,0000	2,4635	-0,3695
50,0000	2,1000	-0,3242
55,0000	1,8600	-0,2870
58,0000	1,7500	-0,2530
59,6000	1,7000	-0,2020
61,0000	1,5000	-0,1370
62,7000	0,3500	-0,0440

Table E.7: Blade twist.

Spanwise coordinate [m]	*Blade twist angle [deg]*
0,0000	13,4000
1,0000	13,4000
10,7000	13,4000
15,0000	8,3460
18,6900	7,3930
44,0000	-0,1000
50,0000	-1,2000
55,0000	-1,8830
58,0000	-1,5000
59,6000	-1,0000
61,0000	-0,5000
62,7000	0,0000

Table E.8: Blade mass distribution.

Spanwise coordinate y_{mass} [m]	*Blade 1 y_{mass} [kg/m]*	*Blade 2 y_{mass} [kg/m]*	*Blade 3 y_{mass} [kg/m]*	*Spanwise coordinate x_{cg} [m]*	*Blade 1 x-coordinate [m] (down-wind) of the mass centre line*	*Blade 2 x-coordinate [m] (down-wind) of the mass centre line*	*Blade 3 x-coordinate [m] (down-wind) of the mass centre line*
0,0000	698,0000	700,9316	698,0000	0,0000	0,0002	0,0002	0,0002
1,2000	798,0000	801,3516	798,0000	1,2000	-0,0245	-0,0245	-0,0245
3,2000	761,0000	764,1962	761,0000	3,2000	0,0442	0,0442	0,0442
5,2000	468,0000	469,9656	468,0000	5,2000	0,0672	0,0672	0,0672
14,2000	363,0000	364,5246	363,0000	14,2000	0,2730	0,2730	0,2730
24,2000	322,0000	323,3524	322,0000	24,2000	0,1969	0,1969	0,1969
34,2000	246,0000	247,0332	246,0000	34,2000	0,1501	0,1501	0,1501
40,2000	183,0000	183,7686	183,0000	40,2000	0,1818	0,1818	0,1818

48,2000	133,0000	133,5586	133,0000	48,2000	0,2308	0,2308	0,2308
60,7000	39,0000	39,1638	39,0000	60,7000	0,0545	0,0545	0,0545
62,6000	2,0000	2,0084	2,0000	62,6000	0,0268	0,0268	0,0268

Table E.9: Radius of Gyration.

Spanwise coordinate [m]	*Distribution of radius of gyration [m]*
0,0000	1,1971
1,2000	1,1726
3,2000	1,2170
5,2000	1,1925
14,2000	1,1563
24,2000	0,9962
34,2000	0,8234
40,2000	0,7423
48,2000	0,6899
60,7000	0,3110
62,6000	0,1085

Table E.10: Blade stiffnesses.

Coordinates for blade bending stiffnesses [m]	*Flatwise bending stiffness [Nm²]*	*Edgewise bending stiffness [Nm²]*	*Flat-edge cross stiffness [Nm²]*
0,0000	1,760000E+10	1,760000E+10	-2,290000E+03
3,2000	1,450000E+10	1,960000E+10	9,490000E+07
5,2000	6,700000E+09	1,000000E+10	8,270000E+07
14,2000	2,370000E+09	4,800000E+09	6,870000E+07
24,2000	1,240000E+09	3,580000E+09	1,140000E+08
34,2000	3,820000E+08	2,240000E+09	9,110000E+06
42,2000	1,210000E+08	1,120000E+09	-1,320000E+07
57,7000	2,330000E+07	2,520000E+08	-3,020000E+06
62,6000	1,870000E+06	5,060000E+07	2,860000E+03

Table E.11: Torsion data.

Spanwise coordinate [m]	*Torsional stiffness [Nm²/rad]*	*Chordwise location [m] of shear centre*
2,000000E-01	7,211200E+09	-2,587000E-01
3,200000E+00	5,938600E+09	-2,082000E-01
5,200000E+00	3,270800E+09	-1,819000E-01
1,420000E+01	5,938600E+08	-3,685000E-01
2,420000E+01	3,052100E+08	-3,459000E-01
2,820000E+01	2,081400E+08	-3,289000E-01
3,020000E+01	1,374000E+08	-2,931000E-01
5,020000E+01	1,457200E+07	-1,154000E-01
5,770000E+01	7,701700E+06	-6,400000E-02
6,070000E+01	2,116400E+06	-3,350000E-02

<

flat_damping 0,0048

edge_damping	0,0048
torsion_damping	0,0048
<	
MENU	wind
load_case	Vacuum
wind_option	0
air_density	1,225
duration	1000
amplitude	0
hor_shear	0
lower_shear	0
shear_type	2
shear_parameter	0,1429
start_time	0
time_period	1000
upper_shear	0
direction_change	0
vert_shear_change	0
hor_shear_change	0
wind_datafile	none
wind_velocity	8
wind_direction	0
wind_elevation	0
wind_twist	0
<	
MENU	waves
wave_option	0
water_density	1025
water_depth	20
wave_datafile	none
wave_direction	0

APPENDIX F MODE SHAPE PLOTS SIMULATIONS BLADEMODE V.2.0

Simulation 1:

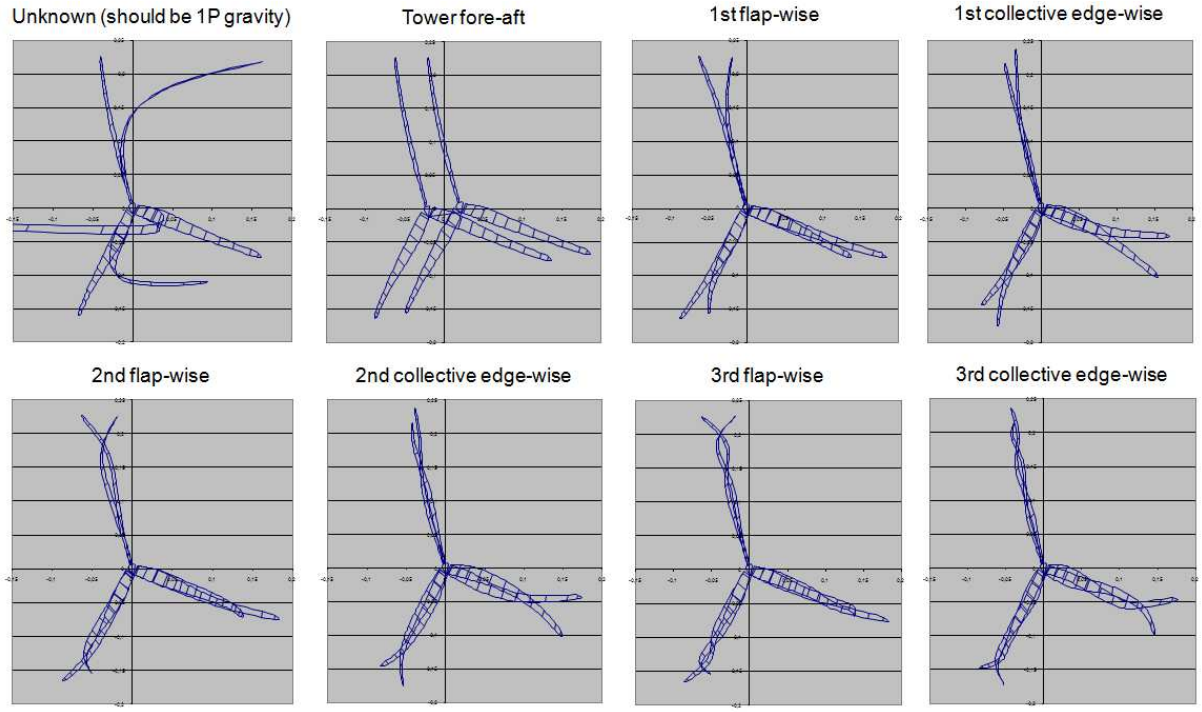

Figure F.1: Mode shape plots for modes 0-7 of simulation 1.

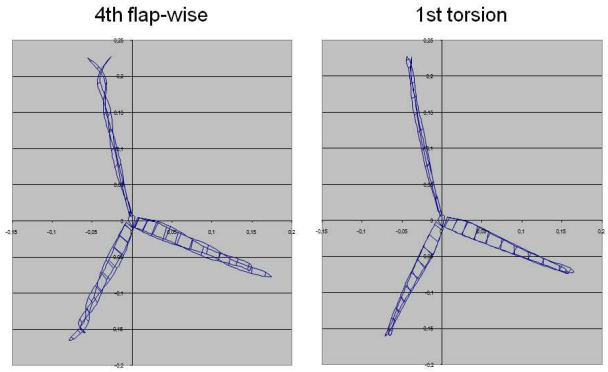

Figure F.2: Mode shape plots for mode 8 and 9 of simulation 1.

Simulation 2 Wind Speed 3 m/s:

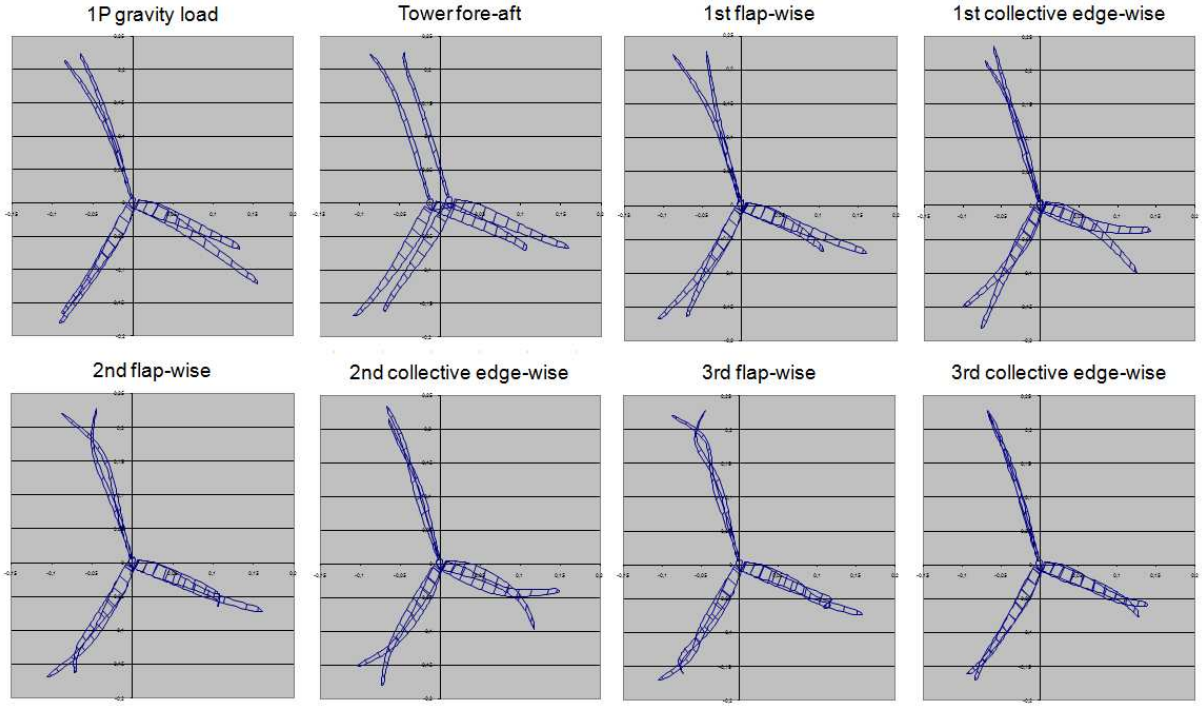

Figure F.3: Mode shape plots for modes 0-7 of simulation 3.

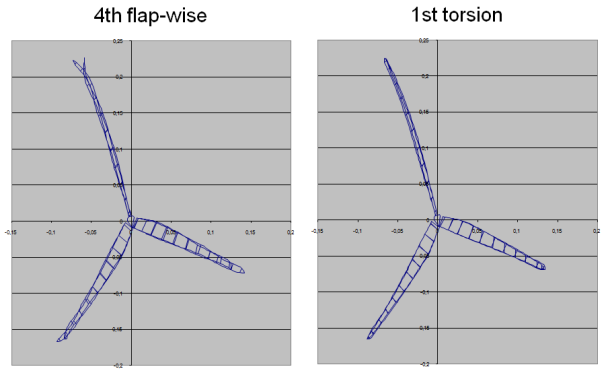

Figure F.4: Mode shape plots for mode 8 and 9 of simulation 3.